



저작자표시-비영리-동일조건변경허락 2.0 대한민국

이용자는 아래의 조건을 따르는 경우에 한하여 자유롭게

- 이 저작물을 복제, 배포, 전송, 전시, 공연 및 방송할 수 있습니다.
- 이차적 저작물을 작성할 수 있습니다.

다음과 같은 조건을 따라야 합니다:



저작자표시. 귀하는 원저작자를 표시하여야 합니다.



비영리. 귀하는 이 저작물을 영리 목적으로 이용할 수 없습니다.



동일조건변경허락. 귀하가 이 저작물을 개작, 변형 또는 가공했을 경우에는, 이 저작물과 동일한 이용허락조건하에서만 배포할 수 있습니다.

- 귀하는, 이 저작물의 재이용이나 배포의 경우, 이 저작물에 적용된 이용허락조건을 명확하게 나타내어야 합니다.
- 저작권자로부터 별도의 허가를 받으면 이러한 조건들은 적용되지 않습니다.

저작권법에 따른 이용자의 권리는 위의 내용에 의하여 영향을 받지 않습니다.

이것은 [이용허락규약\(Legal Code\)](#)을 이해하기 쉽게 요약한 것입니다.

[Disclaimer](#)

공학박사 학위논문

리튬 및 전이금속 화합물을 이용한
리튬 이차 전지용 나노 복합 양극
소재에 관한 연구

**Nanocomposite cathode of lithium and transition
metal compounds for lithium secondary batteries**

2018 년 8 월

서울대학교 대학원

재료공학부

정 성 균

Abstract

Nanocomposite cathode of lithium and transition metal compounds for lithium secondary batteries

Sung-Kyun Jung

Department of Materials Science and Engineering

College of Engineering

The Graduate School

Seoul National University

Diversification and market segmentation of electronic devices application accelerates the explosive demand for efficient energy storage system, especially lithium-ion batteries. Not only the increased demand on supply of lithium ion batteries, but also the superior properties corresponding to large energy density, high power capability and long calendar life are highly required. Investigation and research on cathode materials which is major part determining the performance of lithium-ion batteries has been devoted. Numerous candidates are explored, however, compositional change in layered materials (e.g. LiCoO_2 , $\text{LiNi}_{1-x-y}\text{Co}_x\text{Mn}_y\text{O}_2$) have been believed to be almost the only way practically feasible to improve the energy density. In addition, high power capability and long cycle life which is capable to be applied in practical application is achieved by development of only few materials

such as spinel and olivine. In this context, battery technology is still faced with challenges to expand its coverage from small electronic devices to large scale application such as electric vehicle or energy storage system.

Especially, most of cathode materials which have been developed as intercalation type materials have intrinsic limitation to improve the gravimetric capacity. Conventional cathode materials usually contain the redox active element and lithium in the same open frame crystal structure to accommodate the lithium ion in certain interstitial site. Storing a large amount of lithium leads to a remarkable increase in capacity, however, the number of lithium interstitial sites is limited to the same number of transition metal sites in the structure. In general, even if the contents of lithium interstitial site increase by substitution of transition metal to lithium, deficient transition metal ions cannot afford to provide sufficient electrons corresponding to lithium contents. Therefore, intercalation type cathode materials have intrinsic limitation of crystal structure except lithium-excess material showing additional capacity with anion redox.

A new cathode material design strategy is highly required in order to overcome the intrinsic limitation of intercalation cathode for development of high energy density battery system. Here, I suggest a new kind of nanocomposite cathode material composed of lithium compounds and transition metal compounds. This type of materials is electrochemically activated through the first charge reaction that induces the oxidation of transition metal ion by incorporation of anion from lithium compounds into the transition metal compounds. Reaction mechanism is classified

into surface conversion reaction and host formation reaction as the behavior of anion incorporation. Especially, the redox reaction of transition metal mainly occurs on the surface in the case of the surface conversion reaction mechanism. In addition, the capacity can be controlled by adjusting the particle size of the transition metal compound, which can be an alternative to overcome the limitation of intercalation type cathode materials. The validity of the nanocomposite cathode materials is proven in other battery system such as Na, K beyond lithium rechargeable batteries. This design strategy that can lead to a development of high energy density batteries system can provide an opportunity to broaden the boundaries of cathode materials based on numerous combinations of lithium compounds and transition metal compounds.

Keywords: Nanocomposite, Batteries, Surface conversion, Host formation, Positive electrode, Cathodes, Mixture, Lithium rechargeable batteries.

Student Number: 2014-30216

Contents

List of Tables	viii
----------------------	------

List of Figures	ix
-----------------------	----

Chapter 1 Introduction	1
-------------------------------------	----------

1.1. Motivation and Objectives.....	1
-------------------------------------	---

1.2. Research history based on cathode material design.....	2
-------------------------------------------------------------	---

1.3. Concept of nanocomposite cathode	5
---------------------------------------------	---

1.4. Scope of Thesis.....	9
---------------------------	---

Chapter 2 Lithium-free transition metal monoxides for positive electrodes in lithium-ion batteries.....	11
----------------------------------------------------------------------------------------------------------------	-----------

2.1. Research Background	11
--------------------------------	----

2.2. Experimental Methods.....	13
--------------------------------	----

2.2.1. Synthesis of materials	13
-------------------------------------	----

2.2.2. Electrochemical measurements.....	17
------------------------------------------	----

2.2.3. Charaterization	19
------------------------------	----

2.3. Results and Discussions	23
2.3.1. LiF-MO nanocomposite as positive electrode	23
2.3.2. Electrochemical response of LiF-MnO nanocomposite	32
2.3.3. Mn redox reaction aided by the fluorine ion	37
2.3.4. Surface concentrated chemical and structural changes	47
2.3.5. Particle size effect on electrochemistry	62
2.3.6. Reaction mechanism	72
2.3.7. Supplementary text and discussions	81
2.4. Concluding Remarks	86
2.5. References	87

Chapter 3 Host formation reaction mechanism: New iron-based intercalation host for lithium-ion batteries	92
3.1. Research Background	92
3.2. Experimental Methods	95
3.2.1. Synthesis of LiF-FeO nanocomposite	95
3.2.2. Electrochemical measurements	95
3.2.3. Characterizations	96
3.2.4. Computational details	98
3.3. Results and Discussions	99
3.3.1. Fabrication and electrochemical properties of LiF-FeO	99
3.3.2. New cubic-FeOF phase evolution	104
3.3.3. Charge storage behavior in a cubic-FeOF intercalation host	117
3.3.4. Reaction mechanism	122

3.3.5. Discussion	125
3.4. Concluding Remarks	128
3.5. References	129

Chapter 4 Chemical origins of the activity in nano-mixture

cathode materials.....	134
4.1. Research Background	134
4.2. Experimental Methods.....	137
4.2.1. Synthesis of MFx-MnO nanocomposite.....	137
4.2.2. Electrochemical measurement.....	137
4.2.3. Charaterizations.....	139
4.3. Results and Discussions	141
4.3.1. Electrochemical activities of MFx-MnO as metal fluorides	141
4.3.2. Overpotential of the first charge determining the activity.....	147
4.3.3. Effects of binding energy of F 1s on overpotential and activity..	151
4.3.4. Effect of stability of cation in electrolyte on activity	157
4.3.5. Origins of the overpotential in the first charge activation.....	161
4.4. Concluding Remarks	164
4.5. References	165

Chapter 5 Conclusion	168
-----------------------------------	------------

Chapter 6 Abstract in Korean.....	172
------------------------------------------	------------

List of Tables

Table 2.1. Formation energy of lithium compounds at 298.15 K 75

Table 2.2. Formation free energies of the low-index surfaces in MnO 85

Table 4.1. Correlation between the experimentally obtained F 1s binding energy and
lattice energy of metal fluorides from Born-Haber cycle 155

List of Figures

Figure 1.1.	Specific capacity and output voltage of various positive electrode materials including negative electrodes of metal monoxides	4
Figure 1.2.	Reaction schem of intercalation vs. conversion reaction of electrode materials.	7
Figure 1.3.	Available candidates of metal compounds in nanocomposite electrode materials.....	8

Figure 2.1.	Transition of metal monoxide from negative electrode to positive electrode material (A) Schematic figure of positive electrode material design strategy using metal monoxide (MO). Metal monoxides which only had electrochemical activity as negative electrode were designed as positive electrode material by forming mixtures with LiF in nanoscale under high energy ball milling. After mechanochemical mixing, LiF and MO exist without chemical reaction in several nanometer scale. The crystal structure of all compounds is described by a polyhedral image. (Red: O, Gray: F, Green: Li, Purple: Mn, Brown: Fe, Blue: Co). (B) Powder X-ray diffraction patterns of the MnO/C composite and LiF–MO (M=Mn, Fe, Co) nanocomposite.....	25
--------------------	----------------------------------------------------------------------------------------------------------------------------------------------------------------------------------------------------------------------------------------------------------------------------------------------------------------------------------------------------------------------------------------------------------------------------------------------------------------------------------------------------------------------------------------------------------------------------------------------------------------------------------------------------------------------------------------------------------------------------------------------------------------	----

- Figure 2.2.** (A) FT-IR and (B) Raman spectroscopy of the LiF–MnO nanocomposite and MnO. FT-IR and Raman spectroscopy of the LiF–MnO nanocomposite electrode showing each characteristic MnO peak, including carbon as a conducting agent without any other phase.26
- Figure 2.3.** (A) FT-IR and (B) Raman spectroscopy of the LiF–FeO nanocomposite and FeO. FT-IR and Raman spectroscopy of the LiF–FeO nanocomposite electrode, showing each characteristic MnO peak including carbon as a conducting agent without any other phase. (Asterisks in Raman spectroscopy indicate artifacts.).....27
- Figure 2.4.** Electron diffraction pattern and HR-TEM image of LiF–MnO nanocomposite and particle size distribution in as-prepared state. The white circle in the HR-TEM image identifies a single MnO nanoparticle.....28
- Figure 2.5.** **Electrochemical profiles of LiF–MO nanocomposites as a positive electrode (A–C)** First discharge and second charge profiles of LiF–MO (M=Mn, Fe, Co) nanocomposites after the initial activating charge protocol as a positive electrode (1.5–4.8 V) in 1 M LiPF₆ in ethyl carbonate/dimethyl carbonate (EC/DMC; v/v = 1:1) electrolyte at a 20 mA/g (0.03 mA/cm²) constant current rate..29
- Figure 2.6.** (A, B) Electrochemical profile of the MnO/C composite as a positive electrode and negative electrode at 1.5–4.8 V and 0.02–3.0 V voltage ranges, respectively.....30
- Figure 2.7.** (A) Charge-discharge profiles of LiF–MnO nanocomposite in a full cell with Li₄Ti₅O₁₂ at 20 mA/g (3 cycles).....31

- Figure 2.8. Electrochemical response of the LiF–MnO nanocomposite (A)** Cyclic voltammetry at various scan rates from 0.075 to 1.00 mV s⁻¹ after the first charge to 4.8 V at a constant current density (20 mA/g). **(B, C)** Log-scale plot of peak current (2.5 V, 3.75 V redox reaction) dependence on the scan rate (i_p vs. v). Dotted lines indicate the linear fit of cathodic and anodic current as scan rate. b value indicates the slope of linear fit curve. R square and standard error of each slope are shown in method section. **(D)** Current response with voltage at 1 mV/s scan rate. The overall current signal (solid line) was obtained from the cyclic voltammetry experiment. Capacitive current (shaded region with dotted line) was calculated using $i(V)=k_1v$34
- Figure 2.9.** Correlation between the scan rates and corresponding currents at **(A)** anodic and **(B)** cathodic scan according to equation (2).....35
- Figure 2.10.** **(A)** Electrochemical profile of the LiF–MnO nanocomposite at a high current density from 1000 mA/g to 5000 mA/g and **(B)** galvanostatic cycle properties and coulombic efficiency.....36
- Figure 2.11. Mn redox reaction and fluorine ion contribution (A–D) *In situ*** XANES spectra of Mn–K edge for the first two cycles in the 1.5–4.8 V range. **(E) *Ex situ*** XPS spectra of Li 1s, including the range of Mn 3p binding energy. The peaks were normalized to the Mn 3p peak to compare Li contents in the electrode. **(F)** Fluorine 1s photoelectrons were gathered from the same position as Li 1s. To remove uncertainty from the analysis, the fluorine sources except LiF were eliminated using polyacrylonitrile (PAN) as a binder and ethyl carbonate/dimethyl carbonate (EC/DMC; v/v = 1:1) in a 1 M LiClO₄ electrolyte (LiClO₄ should be used carefully due to the explosive

character). (G) Mn L-edge XAS spectra of LiF–MnO nanocomposite from total electron yield mode (TEY) with different electrochemical states. The vertical dashed lines indicate the edge position of the manganese ion with different oxidation states40

Figure 2.12. *Ex situ* Raman spectra of the LiF–MnO nanocomposite electrode in the charge (4.8 V) and discharge (2.4 V, 1.5 V) state.....41

Figure 2.13. *Ex situ* XANES spectra of LiF–FeO nanocomposite in Fe–K edge during the first charge42

Figure 2.14. *In situ* XANES spectra of the LiF–FeO nanocomposite in the Fe–K edge until the third charge43

Figure 2.15. Comparison of voltage profile of LiF–MnO in (left) 1 M LiPF₆ in EC/DMC and (right) 1 M LiClO₄ in EC/DMC44

Figure 2.16. Mn-L edge spectra of LiF–MnO nanocomposite from soft X-ray absorption spectroscopy. (A) 1st full discharge, (B) 2nd half charge, (C) 2nd full charge, (D) 2nd half discharge, and (E) 2nd full discharge. (F) Portion of Mn⁴⁺ peak (643.2 eV, red) and Mn²⁺ peak (639.6 eV, blue) area as state of charge (G) Mn-L edge reference spectra of MnF₂, Mn₂O₃, and MnO₂. (H) Linear combination of pristine and 1st charged samples using reference spectra.....45

Figure 2.17. F K-edge XAS spectra of LiF–MnO nanocomposite with different electrochemical states46

Figure 2.18. **Surface concentrated F⁻ ion interaction including structural evolution** (A, C) STEM–EELS images of LiF–MnO nanocomposite in charged and discharged state for the elemental distribution of F (green) and Mn (red). (B, D) EELS spectra of Mn L_{2,3} edges recorded from the shell and core regions of charged and discharged states. (E)

In situ EXAFS spectra during two cycles in the 1.5–4.8 V range. The first charge is operated in the 3.0–4.8 V range. EXAFS data and best-fit model for discharged electrode. (F) High-resolution HAADF image of charged state (4.8 V) and (G) discharged state (1.5 V) from yellow box in (A) and (C). The FFT pattern was obtained from the red box. The blue circles indicate an additional FFT pattern compared with the core region. (H) Diffraction pattern of an electrode discharged to 1.5 V51

Figure 2.19. Stability of LiF–MnO nanocomposite under electron beam exposure. (A, C) ADF image of LiF–MnO nanocomposite at charged/discharged state before EELS spectrum collection. (B, D) ADF image after EELS spectrum collection (after 2 h)52

Figure 2.20. ABF and STEM-EELS image of LiF–MnO nanocomposite. (A-D) Charged (4.8 V) and (E, F) discharged (1.5 V) state of LiF–MnO nanocomposite. (F: green, Mn: red) Yellow box shows the location that STEM-EELS measurement was performed. Blue and purple line indicate individual particles53

Figure 2.21. Chemical and electronic structure of LiF–MnO nanocomposite at charged state. (A) ADF image of LiF–MnO nanocomposite. (B) EELS spectra of Mn $L_{2,3}$ edges recorded as position following the green arrow in (A). (C) Mn- L_3 peak energy as position.....54

Figure 2.22. *Ex situ* X-ray diffraction patterns of the LiF–MnO nanocomposite from the first charge to second charge.....55

Figure 2.23. Fourier transformed EXAFS at Mn K-edge of various manganese compounds56

Figure 2.24. Fourier transformed magnitude (black), imaginary part (pink), and

	best-fit (red) model for the discharged electrode. (A) 1 st discharged and (B) 2 nd discharged electrode	57
Figure 2.25.	Crystal structure of (A) Mn ₃ O ₄ and (B) MnO along the coherent crystallographic orientation.....	58
Figure 2.26.	BF and ADF of STEM image of LiF-MnO nanocomposite. (A, B) First charged to 4.8 V. (C, D) Discharged to 1.5 V after the first charge	59
Figure 2.27.	Brightness intensity map of the diffraction ring pattern in Figure 2.18H from the center of the transmission electron beam	60
Figure 2.28.	MnO nanoparticle (cube shape). Assuming that 2 nm surface region (blue) undergoes the significant structural reordering in <i>a</i> nm size of the cubic particle, the volumetric portion of the blue region is calculated by the equation $\{a^3-(a-2)^3\}/a^3$	61
Figure 2.29.	Wulff construction of MnO. Only the (111) surface appeared in the equilibrium shape. (See supplementary text.)	64
Figure 2.30.	Fluorine absorption on the MnO (111) surface. (A) 1 F atom absorption, (B, C) 2 F atom absorption, (D, E) 3 F atom absorption, (F) and 4 F atom absorption in the (111) surface unit cell of MnO. (Red: O, Gray: F, Purple: Mn) (See supplementary text.).....	65
Figure 2.31.	(A) Crystal structure of MnO. (B) Bond length between the Mn and oxygen of each octahedron. (C) Integrated spin as a function of the radius around Mn in MnO. (D) Fluorinated MnO crystal structure after fluorination on the (111) plane of MnO. (E) Bond lengths between the Mn and anions (O and F) of each Mn octahedron. The top layer indicates the newly formed Mn octahedron after jumping up to bond with a fluorine ion. (F) Integrated spin as a function of	

the radius around Mn in fluorinated MnO. Mn was oxidized up to the third layer as a result of fluorination. (See supplementary text)...66

Figure 2.32. Simple model of numerical calculation for capacity of LiF–MnO nanocomposite as a function of the particle size of MnO. (A) The metal oxide (MO) is assumed to be composed by an $N \times N \times N$ octahedron cube (MO_6) by considering the similarity with the closed-packed structure. (B) Particle size as a function of the number of octahedron (N). (C) Electron transfer number as a function of the number of octahedron (N). (D) Electron transfer number as a function of particle size. (E) Correlation between the particle size and capacity of LiF–MnO nanocomposite based on the numerical calculation. The experimental capacity matches well with the prediction based on the numerical calculation67

Figure 2.33. Capacity-tunable LiF–C/Mn₃O₄ nanocomposite cathode materials (A) TEM image of Mn₃O₄ nanoparticles. (B) TEM and EFTEM images of LiF–C/Mn₃O₄ (15 nm) mixture electrode in as-prepared state. (C) Electrochemical profile of LiF–C/Mn₃O₄ nanocomposite with various particle sizes after the first charge...68

Figure 2.34. (A) High-resolution powder diffraction of Mn₃O₄ nanoparticles. (B) Average particle size and size distribution of Mn₃O₄ nanoparticles.....69

Figure 2.35. Transmission electron microscopy image of LiF-C/Mn₃O₄ mixture electrode. Particle size of Mn₃O₄ nanoparticle is 15 nm70

Figure 2.36. Electrochemical profile of LiF-C/Mn₃O₄ mixture electrode with the first charge. Particle size of Mn₃O₄ nanoparticle is 6 nm71

Figure 2.37. (A) Electrochemical profile of the LiF–FeO nanocomposite until the

second charge. Red dashed line indicates the reaction voltage of Li_xFeOF estimated by first-principles calculation⁴⁴. **(B)** *Ex situ* EXAFS spectra of the LiF–FeO nanocomposite during the first charge76

Figure 2.38. *In situ* EXAFS spectra of the LiF–FeO nanocomposite during charge and discharge in the 1.5–4.8 V voltage range. (See supplementary text.)77

Figure 2.39. Structure of **(A)** $\text{Li}_{0.25}\text{FeOF}$, **(B)** $\text{Li}_{0.5}\text{FeOF}$, and **(C)** $\text{Li}_{0.75}\text{FeOF}$ in the [001] *c*-axis projection. Bond cutoff length was set to 2.6 Å. **(D)** Average bond length between Fe and anions (O, F) (left axis) and bond length between Fe–F and Fe–O (right axis) as change in the lithium content in the Li_xFeOF structure. (See supplementary text.)78

Figure 2.40. *Ex situ* XANES spectra of the LiF–CoO nanocomposite at the Co–K edge during the first charge. The XANES shift was small during the charge in the CoO case compared with MnO and FeO. Although the chemical shift of the Co–K edge was small, 0.5 eV, it should be noted that this value is comparable to the chemical shift (0.9 eV) in Li_xCoO_2 ($0 < x < 0.83$), which may imply that the small shift is a chemical characteristic of Co ions in oxide environments¹⁰. Nevertheless, the clear chemical shift of the Co–K edge, similar to the case of Li_xCoO_2 ($0 < x < 0.83$), indicates that the Co ion redox reaction participates in the reversible electrochemical reaction in the LiF–CoO nanocomposite. Given the relatively small chemical shift value of the Co K-edge in the LiF–CoO nanocomposite compared with the reversible capacity, the capacity of the LiF–CoO

nanocomposite could originate from other charge compensation mechanisms, including anion-hybridization of Co ion and the anionic redox reaction.....79

Figure 2.41. Ex situ EXAFS spectra of the LiF–CoO nanocomposite at the Co–K edge during the first charge.....80

Figure 3.1. Synthesis and electrochemical properties of LiF–FeO nanocomposite. (a) XRD patterns of LiF–FeO nanocomposite. The inset presents a high-resolution TEM (HR-TEM) and scanning transmission electron microscope (STEM) image of the LiF–FeO nanocomposite. (b) Electrochemical profile of the nanocomposite electrode at 60 °C and 50 mA/g current density. (c) XANES analysis of as-prepared first charged and first discharged states. (d) Discharge capacities corresponding to different voltage regions as a function of cycle number. The red square indicates the overall capacity. The yellow triangle and blue circle indicate the capacities in the 2.2–4.8 V and 1.5–2.2 V voltage ranges, respectively. (e) Differential analysis of voltage profile at 2nd and 30th cycles..... 102

Figure 3.2. (a) XANES peak energy position at normalized intensity of 0.45. XANES analysis of (b) charged and (c) discharged state of LiF–FeO nanocomposite..... 103

Figure 3.3. Structural evolution of the LiF–FeO nanocomposite during electrochemical cycling. (a) XRD patterns of electrodes at charged/discharged states after different cycle numbers (1, 5, 10, 20

cycles). The green arrows identify the emergence of new peaks, and the red arrows identify the original peak positions of the FeO rock-salt phase. (b) Comparisons of XRD patterns of the electrode in the charged state after 20 cycles with possible reference candidates. The grey dotted lines refer to the peaks of the new phase. The asterisk indicates a peak belonging to the Al foil current collector... 109

Figure 3.4. High resolution X-ray diffraction of LiF-FeO nanocomposite electrodes during the first cycle. Arrow indicates new diffraction peaks from phase evolution on the first charge 110

Figure 3.5. Atomic structure and chemical distribution in LiF-FeO nanocomposite after cycling. (a) HAADF image of the electrode after the 20th charging process (inset: fast-Fourier transform images). The blue circle refers to the electron diffraction spot of a new phase. High-resolution images of (b) region 1 and (c) region 2 in (a). (d) Fe atomic arrangements in the new phase showing two different layers. HAADF-STEM images of the electrodes after the 20th (e) charging and (g) discharging process. (f) Corresponding STEM-EELS images of LiF-FeO nanocomposite for yellow box in (e) with the elemental distribution of F (green) and Fe (red). (h, i) STEM-EELS images of LiF-FeO nanocomposite corresponding to the yellow box in (g) with the elemental distribution of F (green), Fe (red), and O (blue)..... 111

Figure 3.6. (a) HR-TEM image of 20th charged LiF-FeO nanocomposite. (b-d) STEM-EELS images at Fe-L, F-K, and O-K edges. 112

Figure 3.7. EXAFS analysis of (a) charged and (b) discharged states of LiF-FeO nanocomposite. (c) EXAFS spectra of 30th charged/discharged

	electrodes. (d) EXAFS spectra of Fe ₂ O ₃ , Fe ₃ O ₄ , and Fe metal references.	113
Figure 3.8.	Soft XAS analysis of as-prepared and 20th charged state of LiF–FeO nanocomposite in F-K and Fe-L edge range	114
Figure 3.9.	(a) Relative formation energy of P4 ₁ 32-type FeOF as partial occupancy of iron in tetrahedral site compared with reported rutile-FeOF. (b) Most stable structure of P4 ₁ 32-type FeOF (+26.6 meV/f.u. vs. rutile-FeOF) along the c-axis (red: oxygen, white: fluorine, yellow: iron in octahedral site, blue: iron in tetrahedral site). (c) Structure of FeO along the c-axis.....	115
Figure 3.10.	XRD patterns of charged and discharged states of FeO–F phase with lattice parameters.....	116
Figure 3.11.	Transition from surface-controlled to bulk-diffusion-controlled reaction. (a) Cyclic voltammetry curves at various scan rates from 0.1 to 1.0 mV/s after the first charge and (b) thirtieth charge process. (c) Comparison of current response with voltage at 0.6 mV/s before cycling and after the 30 cycles. The shaded region was obtained from the diffusive current calculated using $i(V)=k_2(V)*v^{1/2}$. (d) Quantitative values of charge storage for LiF–FeO nanocomposite electrodes before cycling and after 30 cycles.....	120
Figure 3.12.	Rate performance of LiF–FeO nanocomposite. Charge and discharge profiles of LiF-FeO nanocomposites (a) during the first cycle before the formation of the new host structure and (b) after 20 cycling (after the formation of the new iron host structure). (c) Rate performance at 60 °C upon cycling before and after pre cycles	121

Figure 3.13. (a) Charge and discharge capacity of LiF–FeO nanocomposite as cycles at room temperature. Inset is the charge/discharge voltage profile at 2nd and 100th cycle. (b) Cycle performance at room temperature after the first charge at 60 °C 124

Figure 3.14. (a) GITT curve of LiF–FeO nanocomposite and (b) voltage hysteresis after GITT as a function of lithium content..... 127

Figure 4.1. Synthesis and electrochemical activities of MF_x–MnO nanocomposites. (a) X-ray diffraction patterns of MF_x–MnO (M=Li, Na, K, Rb, Cs, Mg, Ca, Al) nanocomposites. (b) Electrochemical profiles of MF_x–MnO (M=Li, Na, K, Rb, Cs) (c) (M=Mg, Ca, Al) nanocomposites after the first charge to 4.4 V vs. Li⁺/Li in 1 M LiPF₆ in EC/DMC (1:1, v/v) electrolyte. (d) Relation between the number of electrons transferred in the first charge and reversible discharge capacity of MF_x–MnO nanocomposites..... 144

Figure 4.2. (a) Williamson-Hall plot of MnO XRD peaks measured from MF_x–MnO nanocomposite (M=Li, Na, K, Rb, Cs, Mg, Ca, Al). (b) Calculated mean size of MnO in each nanocomposite. Nanocomposites are classified into two groups according to MnO size in order to ignore the MnO size effect on electrochemical activity of nanocomposite 145

Figure 4.3. The reversible capacity of eight MF_x–MnO nanocomposite electrode. The blue bar represent the capacity expressed above the 2.7 V and the green bar represent the capacity expressed below the 2.7

V..... 146

Figure 4.4. Origins of the first charge activation in MF_x -MnO nanocomposites. (a) Initial profile of the first charge of MF_x -MnO nanocomposites (M=Li, Na, K, Mg, Ca; Group A) (b) (M=Rb, Cs, Al; Group B). Inset figures are the correlation of reversible capacity and first charge potential at 0.1F-MnO. (c) Overpotential and relaxed voltage at 0.1F-MnO. Inset figure is GITT of KF-MnO. (d) Overpotential at 0.1F-MnO vs. electrochemical activities ... 149

Figure 4.5. Galvanostatic intermittent titration technique (GITT) curves of MF_x -MnO nanocomposites..... 150

Figure 4.6. Effect of F 1s binding energy on the first charge overpotential and electrochemical activity of MF_x -MnO nanocomposites. (a) Binding energy of metal fluorides(MF_x)-MnO nanocomposites (MF_x -MnO, M=Li, Na, K, Rb, Cs, Mg, Ca, Al) from X-ray photoemission spectroscopy. (b) Dependency of the first charge overpotential on binding energy of F 1s in MF_x -MnO nanocomposites. (c) XRD patterns of $LiCsF_2$ after mechanochemical synthesis. (d) Binding energy of LiF-MnO, CsF-MnO and $0.5LiCsF_2$ -MnO nanocomposite from X-ray photoemission spectroscopy. (e) Enhanced electrochemical activities of $0.5LiCsF_2$ -MnO nanocomposite. Each dotted line is 1st charge profile respectively..... 154

Figure 4.7. Relation between F 1s binding energy of MF_x (M=Li, Na, K, Rb, Cs, Mg, Ca and Al) and activity of MF_x -MnO nanocomposite electrode in (a) 1 M $LiPF_6$ in EC/DMC and (b) 1 M $LiClO_4$ in EC/DMC electrolyte. Each black and red line represents the linear relation

between binding energy and activity in group A (black) and group B (red) compounds..... 156

Figure 4.8. Effect of electrolyte salt on electrochemical activities of MF_x-MnO nanocomposites. (a) Reversible capacities of eight MF_x-MnO nanocomposites tested in 1 M LiPF₆ in EC/DMC (red) and 1 M LiClO₄ in EC/DMC (green). Each of data set was tested 5 times and the error bar is also shown in the graph. (b) The binding enthalpy of Ca²⁺, Li⁺ and Na⁺ with ClO₄⁻ (red) and PF₆⁻ (blue) calculated with DFT. (c) Initial profile of the first charge of 0.5CaF₂-MnO, (d) LiF-MnO, and (e) NaF-MnO nanocomposites as electrolyte salts..... 159

Figure 4.9. Initial charge profile of 1/3AlF₃-MnO nanocomposite electrode tested in 1 M LiPF₆ in EC/DMC 160

Figure 4.10. Origins of the first charge overpotential(η) affecting electrochemical activity in MF_x-MnO nano-mixture cathode materials. (a) Activation barrier for liberating fluorine ion is affected by the attraction force of cation (M^{x+}) which can be estimated by F 1s binding energy. Stability of cation in electrolyte determines the kinetics of cation dissolution into electrolyte during the first charge. Particle size of MnO is another origin of overpotential because the surface conversion mechanism is affected by the active surface area for fluorine incorporation. (b) Schematic of the Gibbs free energy versus reaction coordination of the first charge that shows overall overpotential required for the uphill reaction. Red and blue line indicate two cases when system energy can be changed by stability

of cation in electrolyte..... 163

Figure 5.1. Surface conversion reaction mechanism in LiF-MnO nanocomposite electrode 171

Figure 5.2. Host formation reaction mechanism in LiF-FeO nanocomposite electrode 172

Chapter 1. Introduction

1.1. Motivation and objectives

Global warming, environmental pollution has emerged as grand challenges since the twenty-first century. Concerns of these problems led to demanding the development of renewable energy sources and its applications. As a result, various electric vehicles (EV, HEV and PHEV) and energy storage system (ESS) were suggested as the key solution to solve the problems. Among the various energy storage and conversion technologies, lithium-ion batteries have been regarded as promising system to be applied to that equipment based on high energy and power densities.

Therefore, it is very critical issue to search and develop the new cathode electrode materials involving high energy and power density, long cycling life, and good thermal stability. However, the possible candidates of cathode material were confined to the crystals that contain both redox-active element and lithium ion in the open framework. This concept has been conventionally considered as a standard for searching the cathode materials. But, it could be constraints that limit the varieties of cathode materials and barrier of the development of new cathodes in lithium ion batteries technologies. For the breakthrough of cathode materials in lithium ion batteries technologies, new design concept is required to utilize numerous metal compounds as cathode materials beyond the limitation of conventional crystal system.

1.2. Research history based on cathode material design

Reversible storage of lithium ions in cathode materials is the fundamental principle that enables electrical energy storage in lithium ion batteries, and electrode materials are thus at the heart of advanced lithium rechargeable battery technology. A few key requirements for conventional cathode materials were suggested by Stanley Whittingham. The materials containing lithium and redox-active transition metal ion with open framework crystal structure are regarded as candidates of cathode material. In addition, the material exhibiting high redox potential including high capacity and fast reaction kinetics with lithium can be successfully used as a cathode.

Therefore, lithium ions are generally initially contained in a host crystal of positive electrode materials, and upon charge (or discharge), are extracted from (or reinserted into) the host crystal. Intrinsic lithium and a lithium conduction path are therefore regarded as essential characteristics of the positive electrode material. Representative conventional LiCoO_2 or LiFePO_4 intercalation-based cathode satisfying those requirements deliver 140–170 mAh/g and show 600 Wh/kg energy density. Various cathode materials that follow conventional requirements were developed and the energy density was improved as shown in Figure 1.1

Securing degree of freedom for cathode material design criteria could open a new material pool to discover superior cathode material. Historically, the cathode material or even new battery system has been developed by alleviating the conventionally accepted three main criteria (Intrinsic lithium, transition metal and open framework crystal structure for lithium conduction path) for cathode material.

In the early stage of developing cathode material, intercalation type material satisfying those standards were developed such as LiCoO_2 and LiFePO_4 . In the case of Li-S or Li- O_2 battery system, they are successfully designed by getting degree of freedom from intrinsic transition metal and open framework crystal structure for lithium conduction path. In the case of FeF_3 or V_2O_5 cathode materials, condition of intrinsic lithium is excluded. However, most efforts to design electrode material without open framework crystal structure condition are applied to conversion type anode materials. Therefore, cathode material design strategy by securing the degree of freedom from lithium conduction path can be an opportunity to expand the boundaries for cathode materials.

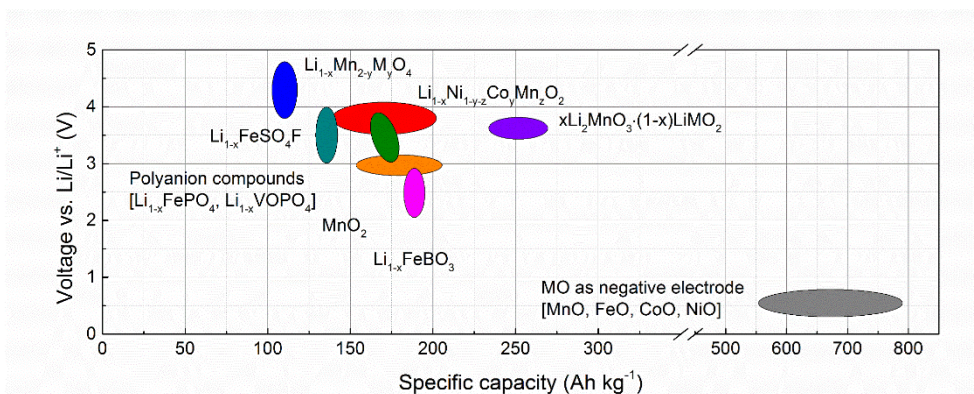


Figure 1.1. Specific capacity and output voltage of various positive electrode materials including negative electrodes of metal monoxides.

1.3. Concept of nanocomposite cathode

Generally, intercalation type conventional cathode material store the energy by accommodating both ions and electrons simultaneously as shown in Figure 1.2. Lithium ion extraction/insertion accompanies oxidation/reduction of nearby transition metal ion in angstrom scale. However, conversion reaction in anode material usually store the lithium ions and electrons separately to each lithium compound and transition metal. Decoupled lithium ion and electron storage occurring in nano-meter scale gave the intuition that it may offer the solution not only for cathode material design strategy without lithium conduction path but also for limited capacity of conventional cathode material due to the confined number of interstitial site for lithium storage (Figure 1.2).

Nanocomposite cathode material ($AX + MY$, AX:Alkali metal compounds / MY: Transition metal compounds / X, Y: anions) is composed of nano mixture of lithium compounds and transition metal compounds. Transition metal ions and lithium ions in the nanocomposite do not exist in the same crystal structure and spatially separated at the nanoscale. Nanocomposite cathode materials store the energy by reversible oxidation and reduction of transition metal ion after activation resulting from the simultaneous decomposition of spatially separated lithium ionic compound. Oxidized state of transition metal ion during charge is neutralized by incorporation of the anion from lithium compound into transition metal compound. In the case of discharge reaction, reduction of transition metal occurs including lithiation into the electrode.

Nanocomposite electrode design strategies have a great potential to enrich the available cathode materials by numerous combinations between lithium and transition metal compounds (Figure 1.3). Boundaries of available cathode materials can be expanded up to transition metal compounds which has been excluded as cathode material itself due to the low voltage or absence of intrinsic lithium. Nanocomposite cathodes are easy to synthesize by mechanochemical mixing without high temperature sintering process.

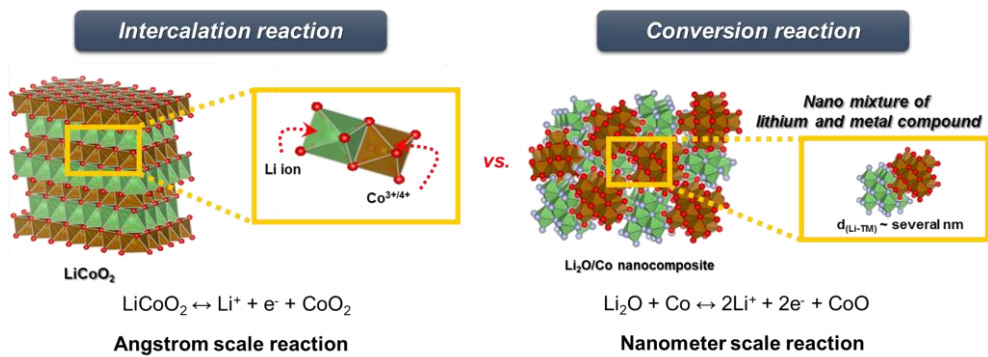


Figure 1.2. Reaction scheme of intercalation vs. conversion reaction of electrode materials.

MY compounds (M : metal, Y : anion)

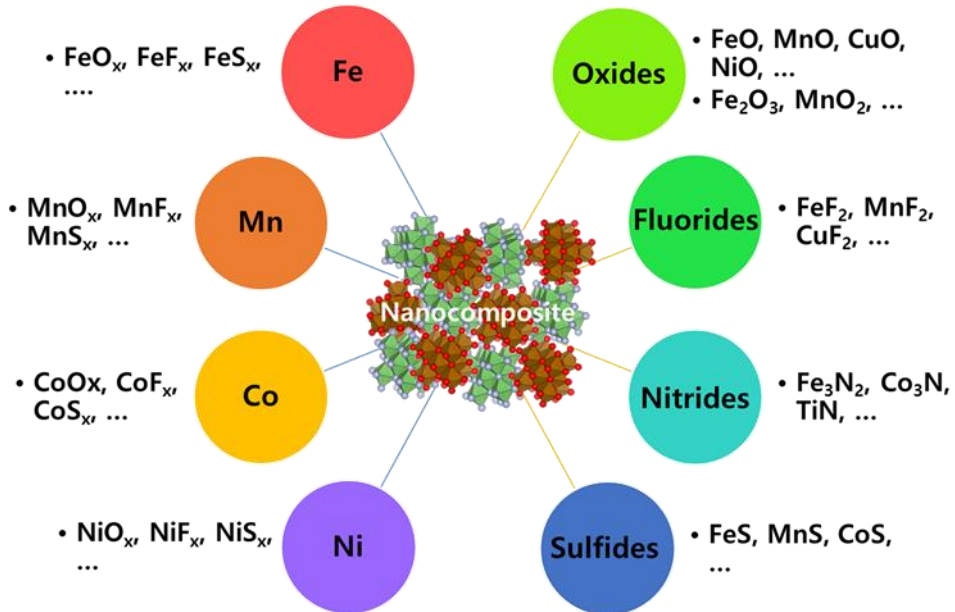


Figure 1.3. Available candidates of metal compounds in nanocomposite electrode materials.

1.4. Scope and aim of Thesis

In this study, I suggest new design strategy of cathode materials for lithium rechargeable batteries. Nanocomposite composed of a mixture with lithium compounds and transition metal compounds can be an alternative to develop high energy density cathode beyond conventional intercalation type cathode materials. Here, I develop various cathode materials based on new design strategy and reveal the energy storage mechanism. In addition, expanded applicability of nanocomposite cathode to other battery system beyond lithium rechargeable batteries is evaluated.

Chapter 2 excavates numerous nanocomposite cathode materials and investigates the feasibility of metal monoxides (MO, M=Mn, Fe, Co) as cathode materials in nanocomposite electrode. Metal monoxides are well known as negative electrode material itself due to the low voltage (< 1 V), however, addition of LiF forms LiF-MO nanocomposite cathode exhibiting ~ 3 V redox potential with high capacity. Superior properties of LiF-MnO nanocomposite is originated from the reversible redox reaction of Mn which is mainly occurred on the surface of MnO by reversible fluorine ion incorporation including structural changes (Surface conversion reaction).

Chapter 3 reveals new energy storage mechanism of host formation reaction. LiF-FeO nanocomposite shows gradual structure changes to cubic-FeOF which can store lithium inside the crystal structure. In contrast to surface conversion reaction, incorporation of fluorine ion into the FeO transforms crystal structure of FeO to cubic-FeOF (Host formation reaction). Electrochemically induced cubic-FeOF which belongs to cubic crystal system has different polymorph to rutile-FeOF which

is thermodynamically stable tetragonal iron oxyfluoride. Host formation reaction pathway in nanocomposite electrode is dependent on the initial crystal structure state.

Chapter 4 studies on the chemical origins of electrochemical activity in nanocomposite cathode materials. Nanocomposite cathode has common problem of large overpotential during the first charge regardless of reaction mechanism due to the inevitable decomposition of lithium compound, which critically affects to the discharge capacity. The correlation between the overpotential and capacity of nanocomposite cathode is investigated with systematic experimental design using the various metal fluorides (MF_x , $\text{M}=\text{Li, Na, K, Rb, Cs, Mg, Ca, Al}$) and MnO as a model system. All metal fluorides function as fluorine ion source for MnO and the overpotential is dependent on binding energy of F I s due to its strong correlation with lattice energy that is required to decompose the ionic compounds as ion state.

Chapter 2. Lithium-free transition metal monoxides for positive electrodes in lithium-ion batteries

(The essence of this chapter has been published in Nature Energy. Reprinted with permission from [S.-K. Jung *et al.*, *Nat. Energy* **2** (2017) 16208] Copyright (2017) Nature Publishing Group)

2.1. Research background

As lithium ion batteries approach the energy density ceiling permitted by conventional intercalation compounds, high demand has arisen for new electrode materials¹⁻³. The discovery of a positive electrode—a key performance component of lithium ion batteries—with high energy/power density, low cost, and long cycle life will expedite progress in emerging areas such as electric vehicles and large-scale energy storage systems (ESSs). Intercalation-based positive electrode materials contain transition metal ions (preferably early 3d metals) as redox active elements and lithium ions as charge carriers. Lithium ions diffuse in and out of the material during battery cycling, and thus the host should contain intrinsic lithium conduction paths. Generally, positive electrodes donate lithium ions in lithium ion batteries, since metallic lithium and lithium-containing negative electrode materials present safety concerns and are chemically unstable^{4, 5}. Accordingly, the most commonly explored positive electrode materials are lithium-containing transition metal compounds with a so-called one-, two-, or three-dimensional open structure, such as olivine (LiMPO_4 ; M=transition metal), layered (LiMO_2), or spinel (LiM_2O_4)

materials⁶⁻⁸. Unfortunately, these material groups constitute only a tiny fraction of the existing redox active transition metal compounds in nature. Numerous transition metal oxides, sulfides, phosphates, and nitrides exist, some of which may exhibit suitable electrochemical potentials *vs.* lithium as a positive electrode, which have been ignored since they are lithium-free or contain no lithium conduction path. Alleviating these restrictions would offer unexplored opportunities to identify new positive electrodes for lithium ion batteries.

Here, it is shown that transition metal monoxides (MO, M=Mn, Fe, Co) that do not contain either intrinsic lithium or a lithium conduction path in their structure can nonetheless function as high-capacity positive electrode materials. These transition metal monoxides are known to be electrochemically active only in negative electrodes (lower than ~ 1 V *vs.* Li^+/Li) by the conversion reaction⁹. We demonstrate herein that when they are blended with nano-sized lithium fluoride (LiF) in the electrode, they not only donate lithium ions to the negative electrode but also exhibit an average voltage of over 3 V (*vs.* Li^+/Li), functioning as a positive electrode. This study focuses on MnO, although characteristics of FeO and CoO are also introduced. This new energy storage mechanism, investigated through a combination of experiment and first-principles calculation, expands our current understanding and brings a variety of unexplored materials into consideration as positive electrode materials.

2.2 Experimental Methods

2.2.1. Synthesis of materials

2.2.1.1. MnO/C nanocomposite

MnO/C nanocomposites were synthesized by planetary ball milling (Pulverisette 5; Fritsch, Idar-Oberstein, Germany). As-received MnO (99%; Sigma-Aldrich, St. Louis, MO, USA) and fluorine-free graphite (Alfa Aesar, Ward Hill, MA, USA) were used without further purification. MnO and graphite were inserted into the same container (MnO/C = 1/0.2, w/w) with an argon atmosphere in the glove box. The powders were mixed in the container at 400 RPM for 48 h without rest time.

2.2.1.2. LiF-MO (M=Mn, Fe, Co) nanocomposite

To synthesize the LiF-MO (M=Mn, Fe, Co) nanocomposite, as-received LiF (99.5%; Sigma-Aldrich) and MO (M=Mn, Fe, Co) (99%; Sigma-Aldrich) were used without further purification. Composite material was prepared by planetary milling (Pulverisette 5; Fritsch). LiF, MO (M=Mn, Fe, Co), and graphite (20 wt% of the LiF-MO composite) were inserted into the same container (Li/M = 1.2/1, m/m), and the container was sealed in an argon-filled glove box to minimize air exposure. The inserted powders were homogeneously mixed in the container at 400 RPM for 48 h without rest time to obtain a finely dispersed composite. The synthesized LiF-MO nanocomposite was characterized by X-ray diffraction (XRD) using a D2 PHASER (Bruker, Bremen, Germany) equipped with Cu-K α radiation ($\lambda = 1.54178$ Å) at a scanning speed of $0.5^\circ \text{ min}^{-1}$ in a 2θ range of $30-70^\circ$. FT-IR and Raman

spectroscopy were performed to check the formation of impurities in the amorphous phase.

2.2.1.3. Mn₃O₄ nanocrystals

Mn₃O₄ nanocrystals (6 nm)

For the synthesis of Mn₃O₄ nanocrystals with edge length of 6 nm, 4.9 g manganese (II) acetate tetrahydrate (Aldrich), 53.4 g oleylamine (Acros), and 5.7 g oleic acid (Aldrich) were dissolved in 300 mL of 1-octanol (Aldrich). The mixture were stirred at room temperature over 3 h in a three-necked 1000-mL flask. The reaction mixture was slowly heated to 120 °C in air under magnetic stirring, and before it reached 120 °C, 3.8 mL of deionized water was rapidly injected into the reaction solution. The solution was aged at 120 °C in air for 2 h. The solution was then cooled to room temperature and washed with acetone and ethanol. The Mn₃O₄ nanocrystals were retrieved by centrifugation. The ligand exchange procedure using hexamethonium hydroxide solution (HMH; Aldrich) was as follows: First, 0.3 g as-prepared Mn₃O₄ nanocrystals were dissolved in 10 mL of tetrahydrofuran (THF) solution. Second, ~1 mL of HMH and ~0.5 mL of deionized water were added to the solution. Then, the nanocrystals were precipitated with ethanol by centrifugation.

Mn₃O₄ nanocrystals (9 nm)

For the synthesis of Mn₃O₄ nanocrystals with edge length of 9 nm, 4.9 g manganese (II) acetate tetrahydrate (Aldrich), 53.4 g oleylamine (Acros), and 2.8 g oleic acid (Aldrich) were dissolved in 300 mL of 1-octanol (Aldrich). The mixture was stirred at room temperature over 3 h in a three-necked 1000-mL flask. The

reaction mixture was slowly heated to 120 °C in air under magnetic stirring, and before it reached 120 °C, 3.8 mL of deionized water was rapidly injected into the reaction solution. The solution was aged at 120 °C in air for 2 h. The solution was then cooled to room temperature and washed with acetone and ethanol. The Mn₃O₄ nanocrystals were retrieved by centrifugation. The ligand exchange procedure using HMH was the same as that described above for the 6-nm-sized nanoparticles.

Mn₃O₄ nanocrystals (11 nm)

For the synthesis of Mn₃O₄ nanocrystals with edge length of 11 nm, 6.4 g manganese (II) acetate tetrahydrate (Aldrich), 17.4 g oleylamine (Acros), and 3.7 g oleic acid (Aldrich) were dissolved in 390 mL of xylene (Aldrich). The mixture was stirred at room temperature for 3 h in a three-necked 1000-mL flask. The reaction mixture was slowly heated to 100 °C in air under magnetic stirring, and after it reached 100 °C, 26 mL of deionized water was rapidly injected into the reaction solution. The solution was aged at 90 °C in air for 1.5 h. The solution was then cooled to room temperature and washed with ethanol. The Mn₃O₄ nanocrystals were retrieved by centrifugation. The ligand exchange procedure was performed using nitrosonium tetrafluoroborate (NOBF₄)³², 0.035 g NOBF₄ was dissolved in 1.5 mL of dimethylformamide (DMF) in an Ar atmosphere. This 1.5 mL of NOBF₄ solution was then added to the 10 mL of THF solution of as-prepared nanocrystals. After the ligand exchange process, the nanocrystals were precipitated with hexane by centrifugation.

Mn₃O₄ nanocrystals (15 nm)

For the synthesis of Mn₃O₄ nanocrystals with edge length of 15 nm, 4.9 g manganese (II) acetate tetrahydrate (Aldrich), 53.4 g oleylamine (Acros), and 2.8 g oleic acid (Aldrich) were dissolved in 300 mL of xylene (Aldrich). The mixture was stirred at room temperature over 3 h in a three-necked 1000-mL flask. The reaction mixture was slowly heated to 90 °C in air under magnetic stirring, and after it reached 90 °C, 7 mL of deionized water was rapidly injected into the reaction solution. The solution was aged at 90 °C in air for 1.5 h. The solution was then cooled to room temperature and washed with ethanol. The Mn₃O₄ nanocrystals were retrieved by centrifugation. The ligand exchange procedure using NOBF₄ was the same as that described for the 11-nm-sized nanoparticles.

Mn₃O₄ nanocrystals (18 nm)

For the synthesis of Mn₃O₄ nanocrystals with edge length of 18 nm, 4.9 g manganese (II) acetate tetrahydrate (Aldrich), 53.4 g oleylamine (Acros), and 2.8 g oleic acid (Aldrich) were dissolved in 300 mL of xylene (Aldrich). The mixture was stirred at room temperature over 3 h in a three-necked 1000-mL flask. The reaction mixture was slowly heated to 100 °C in air under magnetic stirring, and after it reached 100 °C, 8 mL of deionized water was rapidly injected into the reaction solution. Then, the solution was aged at 90 °C in air for 1.5 h. Thereafter, the solution was cooled to room temperature and washed with ethanol. The Mn₃O₄ nanocrystals were retrieved by centrifugation. The ligand exchange procedure using NOBF₄ was the same as that described for the 11-nm-sized nanoparticles.

2.2.1.4. LiF-C/Mn₃O₄ mixture electrode

LiF-C/Mn₃O₄ (6, 9, 11, 15, 18, 20 nm) mixture electrodes were fabricated using the following sequence. In total, 70 wt% of the electrode was composed by a mixture of the LiF-C nanocomposite and Mn₃O₄ nanocrystals (Li/Mn=1/1 m/m). The LiF-C nanocomposite was synthesized using planetary ball milling (Pulverisette 5; Fritsch, Idar-Oberstein, Germany). As-received LiF (Sigma-Aldrich, St. Louis, MO, USA) and F-free graphite (Alfa Aesar, Ward Hill, MA, USA) were used without further purification. MnO and graphite were inserted into the same container (LiF/C = 1/1, w/w) with an Ar atmosphere in a glove box. The powders were mixed in the container at 400 rpm for 48 h without rest time. In addition, 20 wt% carbon black (Super-P; Timcal, Bodio, Switzerland) and 10 wt% F-free binder (polyacrylonitrile, PAN) dissolved in *N*-methyl-1,2,-pyrrolidone (NMP, 99.5%; Sigma-Aldrich) were cast onto aluminum foil using a doctor blade. The NMP was evaporated overnight at 25 °C in a vacuum oven. The final portion of active material (LiF/Mn₃O₄ except carbon) was set as 55.8 wt%.

2.2.2. Electrochemical measurements

Test electrodes were fabricated with the following sequence. A slurry of 70 wt% LiF-MO nanocomposite, 20 wt% carbon black (Super-P; Timcal, Bodio, Switzerland), and 10 wt% polyvinylidene fluoride (PVDF) binder dissolved in *N*-methyl-1,2,-pyrrolidone (NMP, 99.5%; Sigma-Aldrich) was cast onto aluminum foils using a doctor blade. The NMP was evaporated overnight at 25°C in a vacuum

oven. Coin cells (CR2032; Hohsen, Osaka, Japan) were assembled with the LiF–MnO nanocomposite electrode, lithium counter electrode, a separator washed with acetone (GF/F Filter; Whatman, Maidstone, Kent, UK), and a 1 M solution of LiPF₆ in a mixture of ethyl carbonate/dimethyl carbonate (EC/DMC, 1:1, v/v) in an argon-filled glove box. For XPS measurement, a fluorine-free binder (polyacrylonitrile, PAN) and a 1 M solution of LiClO₄ in EC/DMC (1:1, v/v) were used. To evaluate the properties of the LiF–MO nanocomposite, galvanostatic charge/discharge profiles were measured over voltage ranges of 1.5–4.8 V with a potentiogalvanostat (WBCS 3000; WonA Tech, Seoul, Korea) at room temperature. LiF–C/Mn₃O₄ mixture electrode was tested over voltage ranges of 2.0–4.8 V. The first charge process was performed under the constant current and constant voltage (CC/CV) mode to 4.8 V under 20 mA/g at room temperature and maintained until the current density decreased below 10 mA/g. The capacity was calculated by dividing the absolute capacity by the weight of active material including LiF and MO (M=Mn, Fe, Co). CV measurements were obtained after the first charge using the same protocol as for the galvanostatic charge. The voltage was scanned from 4.8 to 1.5 V as the scan rate was changed from 0.075 to 1.00 mV s⁻¹. The peak currents at 3.75 V and 2.5 V redox reaction were plotted as scan rate and analyzed by linear fit in log scale. Adjusted R-square value of 3.75 V was same as 0.9995 at cathodic and anodic reaction. The values of 2.5 V were 0.9994 and 0.9952 at cathodic and anodic reaction respectively. The standard errors of 3.75 V were 0.00949 and 0.00973 at cathodic and anodic reaction. In the case of 2.5 V, the standard errors were 0.04039 and

0.01579 each. The full cell was assembled into a coin-type cell with a $\text{Li}_4\text{Ti}_5\text{O}_{12}$ electrode as the negative electrode and LiF-MnO nanocomposite as the positive electrode. The cell was tested in the voltage range 0.01–3.3 V at a current rate of 20 mA g^{-1} based on the weight of the positive electrode.

2.2.3. Characterization

2.2.3.1. In-situ X-ray absorption spectroscopy (XAS) and ex-situ X-ray diffraction (XRD) analysis

For *in situ* absorption spectroscopy (XAS) experiments, holed coin cells sealed using epoxy with Kapton film were used. The current rate fixed was at 20 mA/g , and the charge discharge protocol followed the same conditions as those used in the galvanostatic experiments. *In situ* XAS was performed at the 7D XAFS and 10C wide XAFS beamlines at the Pohang Light Source-II (PLS-II) using the Si(111) double-crystal monochromator. The beam intensity was reduced by 20%–30% to minimize high-order harmonics. The Mn and Fe K-edge spectra of LiF-MO ($\text{M}=\text{Mn}, \text{Fe}$) electrodes were recorded in transmission mode at room temperature. The storage ring was operated at 2.5 GeV with a ring current of 100–150 mA. Reference spectra of the Mn and Fe metals were collected simultaneously using Mn and Fe metal foils. The XAS data were analyzed using the Athena program, and the spectral energies were calibrated using the first inflection points in the Mn and Fe metal foil spectra. The extracted extended X-ray absorption fine structure (EXAFS) signal, $\chi(k)$, was

weighted by k^3 to emphasize the high-energy oscillations and then Fourier-transformed in a k range from 2.0 to 11.5 \AA^{-1} for the Mn and 2.0 to 11.8 \AA^{-1} for the Fe K-edge using a Hanning window to obtain the magnitude plots of the EXAFS spectra in R -space (\AA). Data pre-processing operations such as deglitching, energy calibration, normalization, and least-squares fitting with theory were performed as described by Kelly *et al.*³³ using IFEFFIT³⁴ which used the FEFF code³⁵. *Ex situ* XRD patterns for the LiF–MnO electrode were collected on the 5A XRD beamline at PLS-II. Samples were prepared by subdividing points in the charge/discharge cycles. Electrodes were collected by disassembling the coin cell after achieving the set capacity. Collected electrodes were washed using diethyl carbonate (DEC) and dried in the dry room. Samples were sealed using Kapton tape and packed in an aluminum pouch to prevent contamination. The wavelength of the X-ray beam was 0.7653 \AA , and XRD patterns were recorded as a set of circles on a Mar 345-image plate detector in the transmission mode for about 1 min of exposure time. The total recording time was about 2.6 min, including the scanning time of the image plate and transfer time of spectral information. The 2θ angles of all the XRD patterns presented in this article have been recalculated to corresponding angles for $\lambda = 1.54$ \AA , which is the wavelength of the conventional X-ray tube source with Cu–K α radiation for easy comparison with other published results. High-resolution powder X-ray diffraction (XRD) data of Mn₃O₄ nanoparticles were obtained from Beamline 9B at Pohang Accelerator Laboratory (PAL), Republic of Korea. The data were collected over a 2θ range of 10–130 $^\circ$ with a step size of 0.01 $^\circ$, step time of 6 s, and

wavelength of $\lambda=1.4865 \text{ \AA}$

2.2.3.2. Near edge X-ray absorption fine structure (NEXAFS) spectroscopy

NEXAFS spectra of Mn L₃, 2-edge and F K-edge were taken at 10D KIST bending magnet beamline at the Pohang Light Source-II (PLS-II). All the measurements were performed at room temperature and the spectra were collected in a total electron yield (TEY) mode under a base pressure of 3×10^{-10} Torr. The spectra were normalized to the incident photon flux, and the energy resolution was 0.1 eV.

2.2.3.3. Ex-situ X-ray photoelectron spectroscopy (XPS)

Half-cells of the LiF–MO (M=Mn, Fe) nanocomposites were assembled and electrochemically cycled. The charged electrode was collected by disassembling the coin cell charged to 4.8 V, and the discharged electrode was collected from the coin cell discharged to 1.5 V after being charged to 4.8 V. The collected electrodes were washed using DMC and dried. The chemical states and composition of the collected electrodes were identified by X-ray photoelectron spectroscopy (Thermo VG Scientific, Waltham, MA, USA).

2.2.3.4. TEM and STEM-EELS Measurements

For *ex situ* analysis, electrodes at different state of charges (SOCs) in half cells were disassembled in a glove box and washed using DMC before drying. The electrodes detached from the aluminum current collector were immersed in DMC

and dispersed using sonication. The TEM sample grid was covered by DMC to minimize any exposure to air during the sample transfer and kept in a vacuum before being transferred to the transmission electron microscope³⁶.

STEM–EELS measurements were performed using a cold field-emission type Cs-corrected JEM-ARM200F equipped with an EELS detector (965 GIF Quantum ER) installed at the National Center for Inter-university Research Facilities(NCIRF) at Seoul National University. High-resolution annular-dark-field images were collected with 0.1-nm spatial resolution. TEM was performed at 80 kV. For STEM–EELS elemental mapping, the energy dispersion was set as 0.25 eV/ch. The full width at half-maximum of the zero-loss peak in vacuum was 1.0 eV. The convergence and collection semiangles were 19 and 52.8 mrad, respectively. TEM and energy-filtered TEM (EFTEM) images of the as-synthesized Mn₃O₄ nanoparticles and LiF–C/Mn₃O₄ electrode were captured using a JEOL-2100F at 200 kV.

2.3 Results and Discussions

2.3.1. LiF-MO nanocomposite as positive electrode

Mixtures of LiF and MO (M=Mn, Fe, Co) were fabricated using a high-energy ball miller under an argon atmosphere (Figure 2.1 (A)). The presence of the mixture (LiF and MO) was confirmed using X-ray diffraction (Figure 2.1 (B)) without any impurity phase, which may be formed during the mechanochemical mixing (Figure 2.2 and 2.3) ¹⁰. The particle size of the composite was around 8 nm as shown by high-resolution transmission electron microscopy (HR-TEM) (Figure 2.4). The mechanochemically treated MnO/C composite was synthesized for comparison with the LiF-MnO nanocomposite to verify the effect of the lithium compound (LiF).

LiF-MO (M=Mn, Fe, Co) nanocomposites showed positive electrode properties with high voltage and capacity after the first charging step (Figure 2.5 (A)-(C)). Almost 0.9 of the lithium in the LiF-MnO nanocomposite participated in the reversible reaction (theoretical capacity corresponding to one lithium: 262.63 mAh/g) at a 3.1 V average voltage. Meanwhile, the MnO/C composite was nearly inactive in the voltage range >1.5 V and only had electrochemical activity as the negative electrode from the conversion reaction within a low voltage range (<1.0 V) (Figure 2.6)^{9, 11-13}. This implies that the addition of LiF critically affects MnO activation during the electrochemical reaction. The characteristic profile of LiF-MnO is displayed in a full cell with Li₄Ti₅O₁₂ negative electrode (Figure 2.7)¹⁴. LiF-FeO and LiF-CoO nanocomposites delivered discharge capacities of 310 and 206 mAh/g,

respectively, demonstrating the general applicability of metal oxides used as positive electrodes when mixed with LiF (Figure 2.5 (B) and (C)).

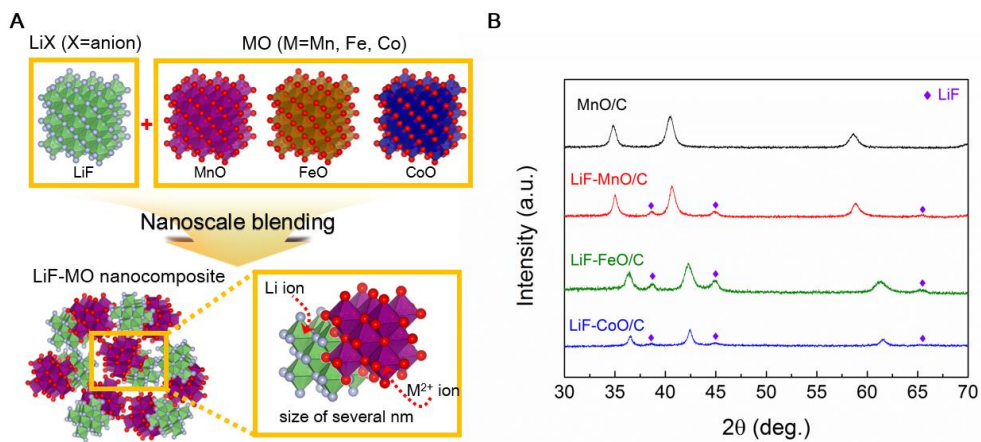


Figure 2.1. Transition of metal monoxide from negative electrode to positive electrode material (A) Schematic figure of positive electrode material design strategy using metal monoxide (MO). Metal monoxides which only had electrochemical activity as negative electrode were designed as positive electrode material by forming mixtures with LiF in nanoscale under high energy ball milling. After mechanochemical mixing, LiF and MO exist without chemical reaction in several nanometer scale. The crystal structure of all compounds is described by a polyhedral image. (Red: O, Gray: F, Green: Li, Purple: Mn, Brown: Fe, Blue: Co). **(B)** Powder X-ray diffraction patterns of the MnO/C composite and LiF–MO (M=Mn, Fe, Co) nanocomposite

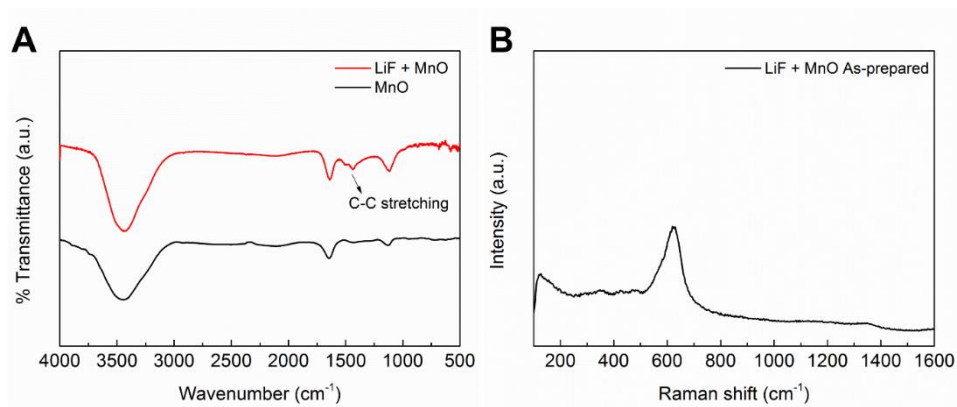


Figure 2.2. (A) FT-IR and (B) Raman spectroscopy of the LiF–MnO nanocomposite and MnO. FT-IR and Raman spectroscopy of the LiF–MnO nanocomposite electrode showing each characteristic MnO peak, including carbon as a conducting agent without any other phase.

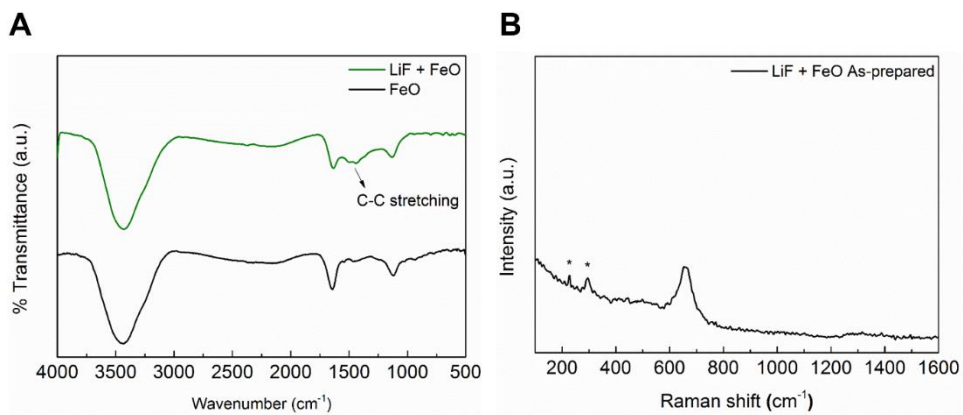


Figure 2.3. (A) FT-IR and (B) Raman spectroscopy of the LiF–FeO nanocomposite and FeO. FT-IR and Raman spectroscopy of the LiF–FeO nanocomposite electrode, showing each characteristic MnO peak including carbon as a conducting agent without any other phase. (Asterisks in Raman spectroscopy indicate artifacts.)

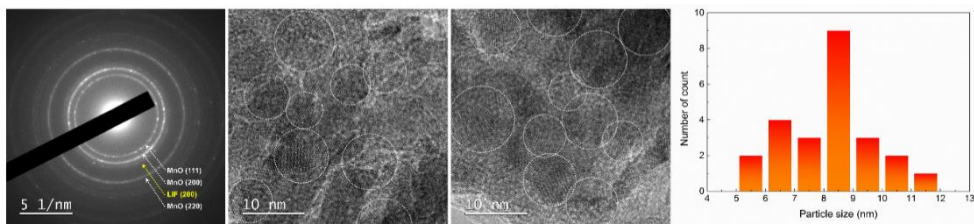


Figure 2.4. Electron diffraction pattern and HR-TEM image of LiF-MnO nanocomposite and particle size distribution in as-prepared state. The white circle in the HR-TEM image identifies a single MnO nanoparticle.

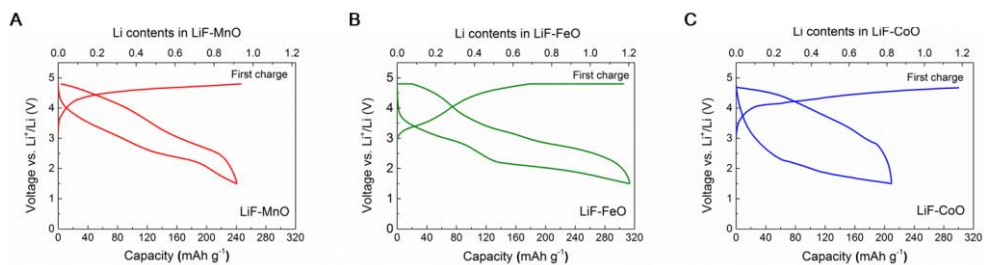


Figure 2.5. Electrochemical profiles of LiF–MO nanocomposites as a positive electrode (A–C) First discharge and second charge profiles of LiF–MO (M=Mn, Fe, Co) nanocomposites after the initial activating charge protocol as a positive electrode (1.5–4.8 V) in 1 M LiPF₆ in ethyl carbonate/dimethyl carbonate (EC/DMC; v/v = 1:1) electrolyte at a 20 mA/g (0.03 mA/cm²) constant current rate.

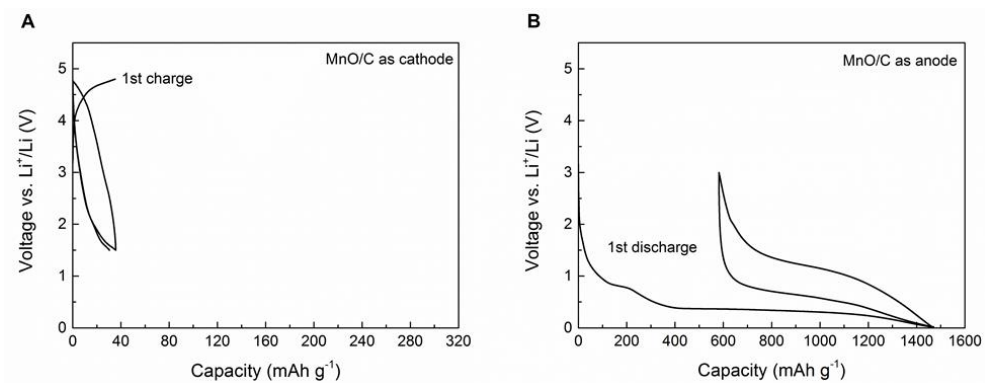


Figure 2.6. (A, B) Electrochemical profile of the MnO/C composite as a positive electrode and negative electrode at 1.5–4.8 V and 0.02–3.0 V voltage ranges, respectively.

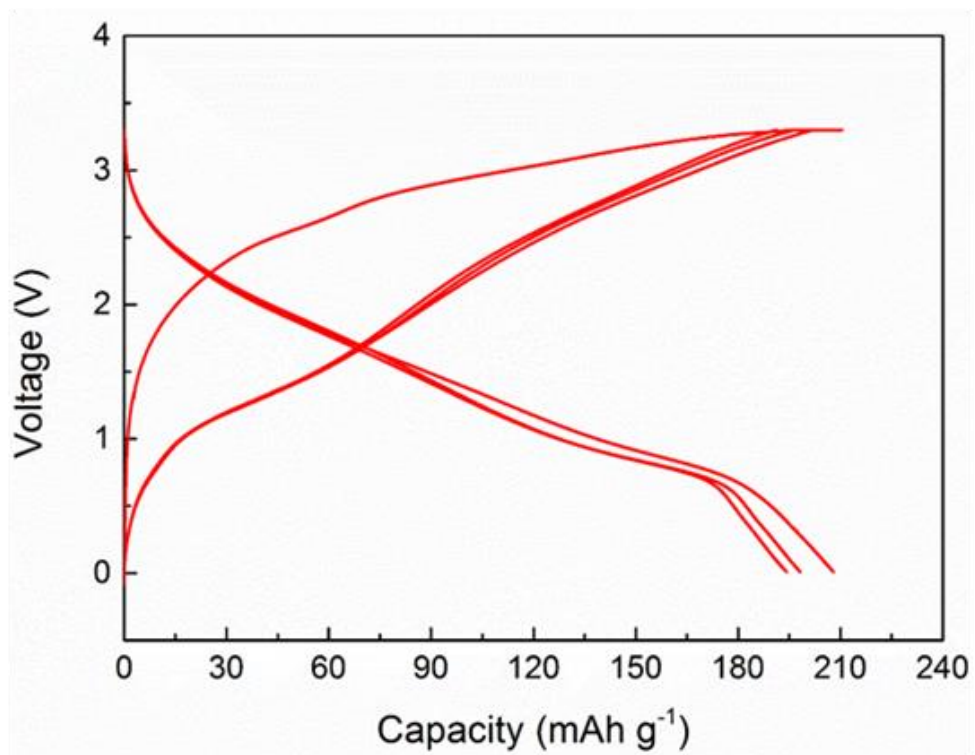


Figure 2.7. (A) Charge-discharge profiles of LiF-MnO nanocomposite in a full cell with $\text{Li}_4\text{Ti}_5\text{O}_{12}$ at 20 mA/g (3 cycles).

2.3.2. Electrochemical response of LiF-MnO nanocomposite

Pseudocapacitive electrochemical behavior was observed in LiF-MnO nanocomposite from the electrochemical response in the cyclic voltammetry (CV) experiment from 0.075 mV s⁻¹ to 1.00 mV s⁻¹. In the CV experiment, the redox reaction appeared mainly at 2.5 V and 3.75 V, which could be ascribed to manganese redox reaction (Figure 2.8 (A)). Cathodic and anodic peak currents at each reaction voltage (2.5 V, 3.75 V) tend to increase as scan rate increases from 0.075 mV s⁻¹ to 1.00 mV s⁻¹. The redox peak currents obey a power-law relationship with the scan rate, which exhibits a nearly linear proportionality of $i_p = av^b$ ($b = \sim 1$) (Figure 2.8 (B) and (C)), indicating that the electrochemical reaction is primarily surface controlled in contrast to the bulk-diffusion-controlled reaction ($b = 0.5$) generally observed in intercalation-based positive electrodes¹⁵. The current can be expressed more precisely as the sum of the surface-controlled and diffusion-controlled capacities at a fixed potential¹⁶⁻¹⁸:

$$i(V) = k_1v + k_2v^{1/2} \quad (1)$$

In equation 1, the k_1v and $k_2v^{1/2}$ terms indicate the surface- and diffusion-controlled contributions, respectively. The k_1 and k_2 values at fixed potentials were determined by the correlation between the scan rates and corresponding current signals according to equation 2 (Figure 2.9):

$$i(V)/v^{1/2} = k_1v^{1/2} + k_2 \quad (2)$$

Accordingly, the capacitive contribution as a function of the voltage could be obtained using $i(V) = k_1v$ at 1 mV/s scan rate, as demonstrated in Figure 2.8 (D).

The capacity from the surface-controlled reaction accounts for 94 % of the overall capacity by comparing the shaded region with the total area. The remarkable power capability of the LiF–MnO nanocomposite assures the surface-controlled reaction kinetics. The electrode exhibited 110 mAh/g discharge capacity even at a current rate of 5,000 mA/g, with a cycle life stable over 100 cycles (Figure 2.10).

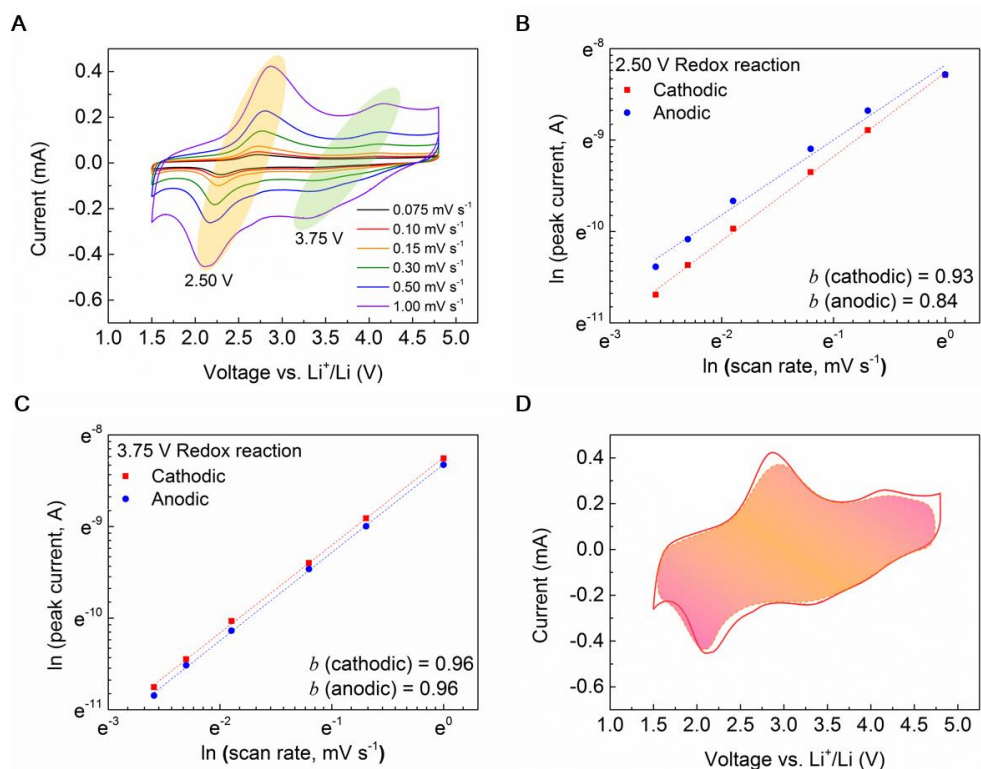


Figure 2.8. Electrochemical response of the LiF-MnO nanocomposite (A) Cyclic voltammetry at various scan rates from 0.075 to 1.00 mV s⁻¹ after the first charge to 4.8 V at a constant current density (20 mA/g). **(B, C)** Log-scale plot of peak current (2.5 V, 3.75 V redox reaction) dependence on the scan rate (i_p vs. v). Dotted lines indicate the linear fit of cathodic and anodic current as scan rate. b value indicates the slope of linear fit curve. R square and standard error of each slope are shown in method section. **(D)** Current response with voltage at 1 mV/s scan rate. The overall current signal (solid line) was obtained from the cyclic voltammetry experiment. Capacitive current (shaded region with dotted line) was calculated using $i(V)=k_1v$.

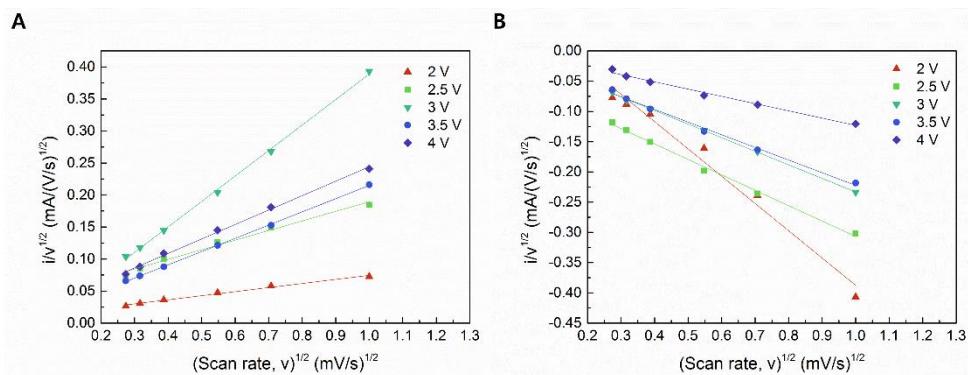


Figure 2.9. Correlation between the scan rates and corresponding currents at (A) anodic and (B) cathodic scan according to equation (2).

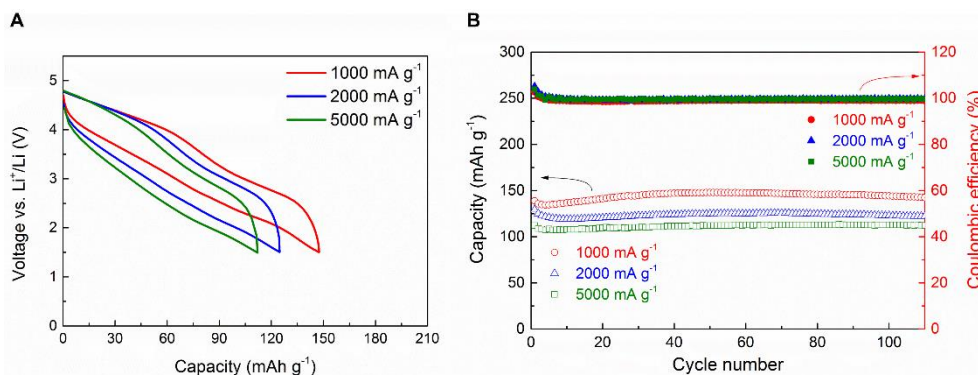


Figure 2.10. (A) Electrochemical profile of the LiF-MnO nanocomposite at a high current density from 1000 mA/g to 5000 mA/g and (B) galvanostatic cycle properties and coulombic efficiency.

2.3.3. Mn redox reaction aided by the fluorine ions

The reversible change in the Mn oxidation state was observed during the entire charge and discharge reaction using *in situ* X-ray absorption near-edge structure analysis (XANES), shown in Figure 2.11 (A) and (B). Mn oxidation and reduction were evident for both the first and subsequent cycles (Figure 2.11 (C) and (D)). Raman spectroscopy also showed the reversible Mn redox reaction. The stretching bond strength between Mn and O ($610\text{--}648\text{ cm}^{-1}$) changed due to variations in the electrostatic attraction force, according to the oxidation and reduction of Mn ions (Figure 2.12). Similarly, the LiF–FeO nanocomposite also showed that the Fe redox reaction participated in the electrochemical reaction as confirmed by *in situ* XANES (Figure 2.13 and 2.14).

As with the reversible oxidation and reduction of Mn, Li and F ion in LiF participates as a charge carrier and charge neutralizer. Additional experiments excluding any fluorine sources other than LiF, *i.e.* using fluorine-free binder and electrolyte were carried out in Figure 2.15, which showed no significant changes in the electrochemical profile, confirming the role of LiF as the source of F. X-ray photoemission spectroscopy (XPS) of Li 1s region showed that the lithium signal at 56.0 eV disappears at charge and is recovered at discharge (Figure 2.11 (E)). Especially notable is that the extraction of lithium ions during the first charge indicates the decomposition of LiF. In the F1s region shown in Fig. 4F, the binding energy of 685.3 eV from LiF increased to 686.0 eV after charge and returned to the initial state when discharged. A peak at 686.0 eV comes from the local environment

of the F^- ion bound to the Mn ion to satisfy charge neutrality as oxidation occurs.

The electrochemical reaction between the MnO and F ions was further investigated using soft X-ray absorption spectroscopy (Figure 2.11 (G)). Mn-L edge signals collected from the surface-sensitive total electron yield mode (TEY) revealed the characteristic peak of Mn^{2+} (639.6 eV), including a small portion of the Mn^{3+} signature in the as-prepared state, which has been observed in MnO in many previous works¹⁹. Upon charging, the Mn^{3+} and Mn^{4+} signals increased at the expense of the Mn^{2+} signal. We analyzed the X-ray absorption spectra by linear combination of various valence states Mn reference spectra. MnF_2 , Mn_2O_3 and MnO_2 are used as references of Mn^{2+} , Mn^{3+} and Mn^{4+} oxidation state. As a result, the portion of Mn^{4+} increased from 0 to 11.3 % after the first charge. The reversible change was observed during the subsequent electrochemical cycling, which indicates that not only Mn^{2+}/Mn^{3+} but also Mn^{3+}/Mn^{4+} redox reactions are involved in the electrochemical reaction. It was noted that the Mn^{3+}/Mn^{4+} reaction mainly participates in the high potential redox reaction (~ 3.75 V), while Mn^{2+}/Mn^{3+} redox reaction occurs in the entire voltage range as described in Figure 2.16.

The F-K edge spectra revealed slight changes in the 685–687.5 eV range (Figure 2.17). In the charged state, the peak at 685–687.5 eV, which is mainly observed in the manganese fluoride system (MnF_2 or MnF_3), slightly increased²⁰. In contrast to the charged state, the peak reversibly decreased in the discharged state. The XPS and XAS results imply that the Mn^{2+}/Mn^{3+} and Mn^{3+}/Mn^{4+} redox reactions mainly occur on the MnO surface accompanying F^- ion interaction. It is noted that

the redox peak at 3.75 V in the CV experiment (Figure 2.8 (A)) accompanies the $\text{Mn}^{3+}/\text{Mn}^{4+}$ related redox reaction as shown in Figure 2.16. Additionally, the pseudocapacitive behavior may be due to the surface redox reaction of MnO with F^- ion from LiF. However, the current response does not establish the reaction mechanism, therefore, we further investigated the reaction mechanism using transmission electron microscopy (TEM)²¹.

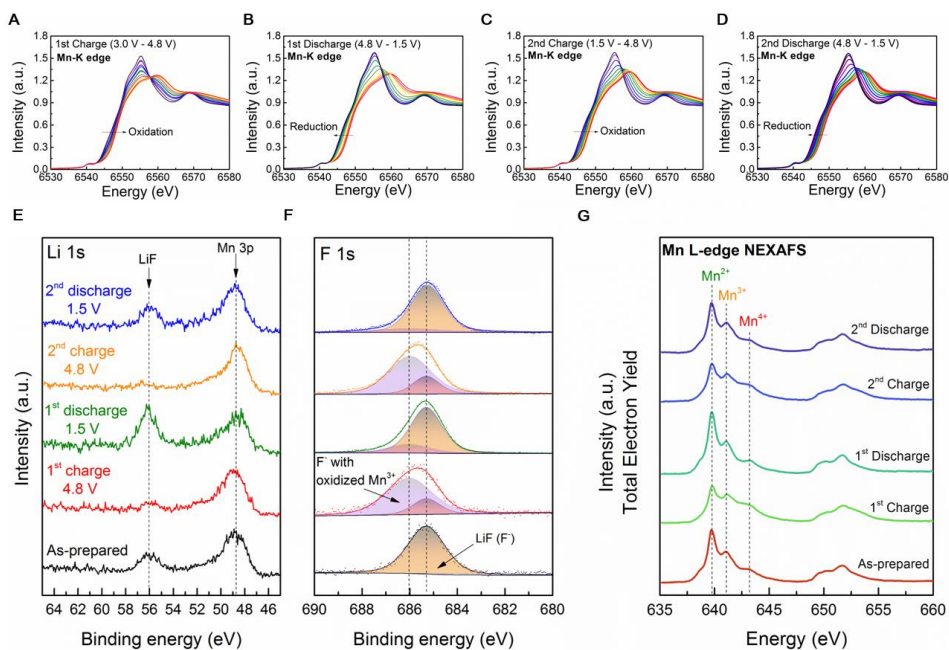


Figure 2.11. Mn redox reaction and fluorine ion contribution (A–D) *In situ* XANES spectra of Mn–K edge for the first two cycles in the 1.5–4.8 V range. (E) *Ex situ* XPS spectra of Li 1s, including the range of Mn 3p binding energy. The peaks were normalized to the Mn 3p peak to compare Li contents in the electrode. (F) Fluorine 1s photoelectrons were gathered from the same position as Li 1s. To remove uncertainty from the analysis, the fluorine sources except LiF were eliminated using polyacrylonitrile (PAN) as a binder and ethyl carbonate/dimethyl carbonate (EC/DMC; v/v = 1:1) in a 1 M LiClO₄ electrolyte (LiClO₄ should be used carefully due to the explosive character). (G) Mn L-edge XAS spectra of LiF–MnO nanocomposite from total electron yield mode (TEY) with different electrochemical states. The vertical dashed lines indicate the edge position of the manganese ion with different oxidation states.

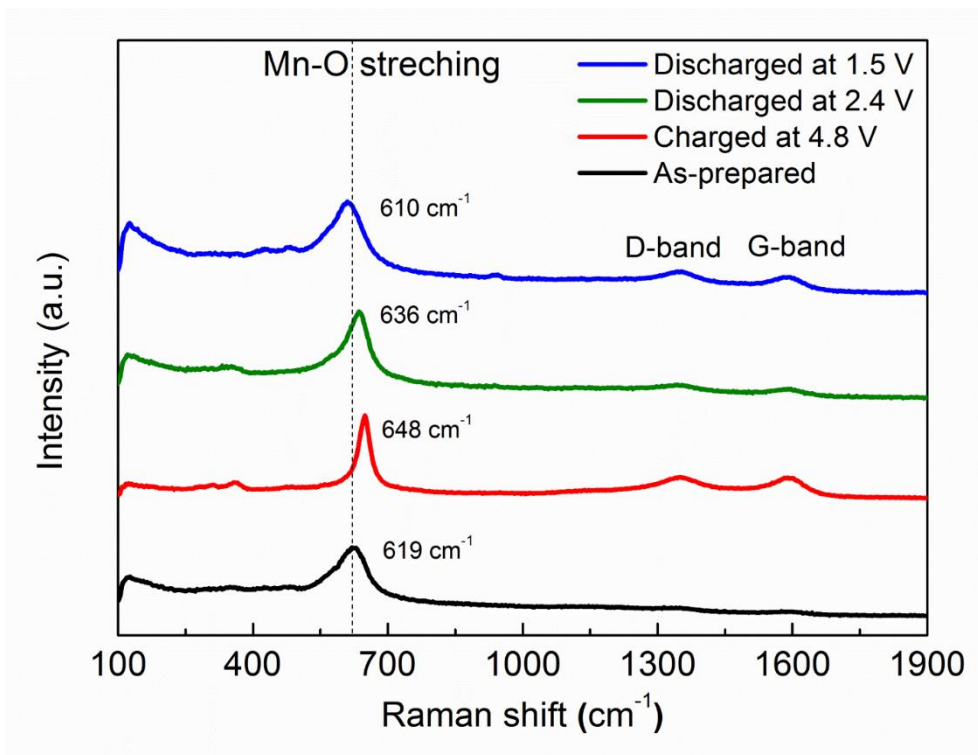


Figure 2.12. *Ex situ* Raman spectra of the LiF-MnO nanocomposite electrode in the charge (4.8 V) and discharge (2.4 V, 1.5 V) state.

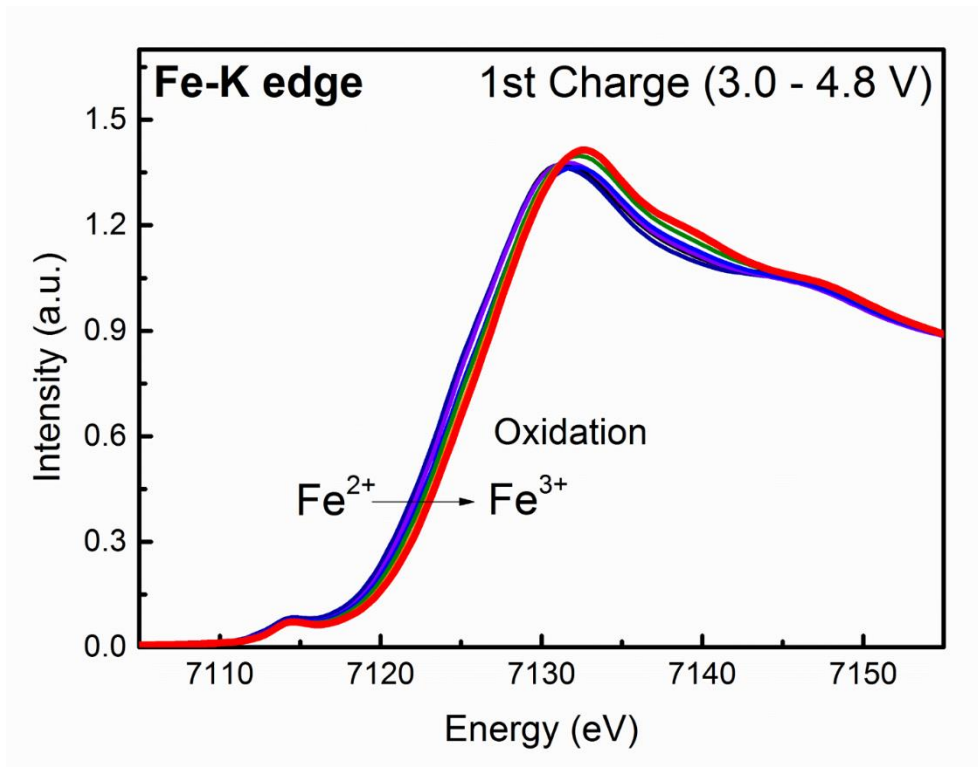


Figure 2.13. *Ex situ* XANES spectra of LiF-FeO nanocomposite in Fe-K edge during the first charge.

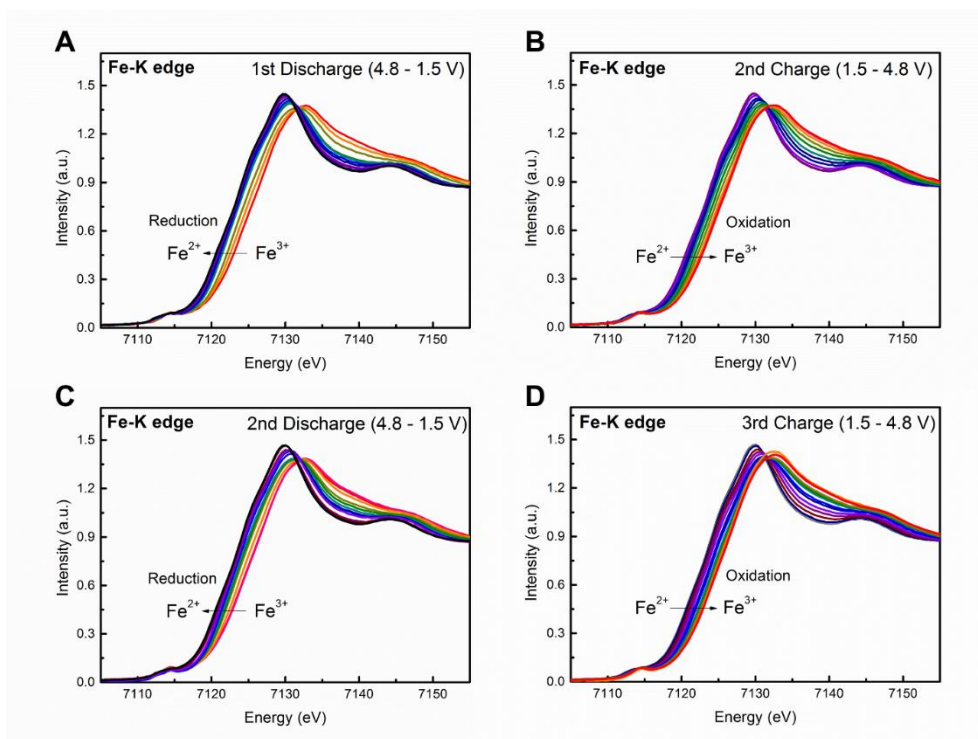


Figure 2.14. *In situ* XANES spectra of the LiF-FeO nanocomposite in the Fe-K edge until the third charge.

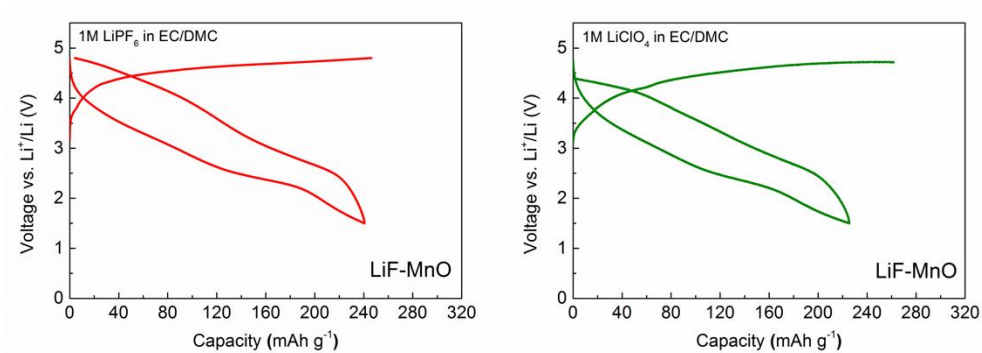


Figure 2.15. Comparison of voltage profile of LiF-MnO in (left) 1 M LiPF₆ in EC/DMC and (right) 1 M LiClO₄ in EC/DMC.

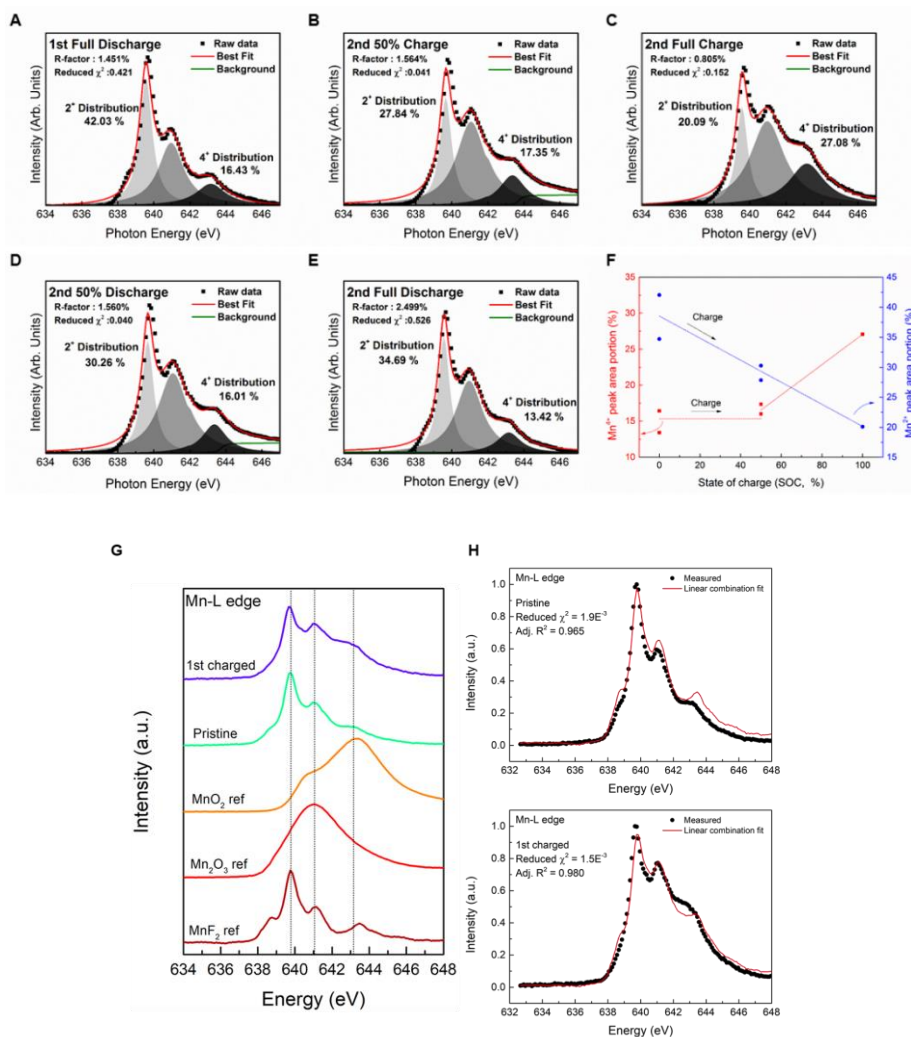


Figure 2.16. Mn-L edge spectra of LiF-MnO nanocomposite from soft X-ray absorption spectroscopy. (A) 1st full discharge, (B) 2nd half charge, (C) 2nd full charge, (D) 2nd half discharge, and (E) 2nd full discharge. (F) Portion of Mn⁴⁺ peak (643.2 eV, red) and Mn²⁺ peak (639.6 eV, blue) area as state of charge. (G) Mn-L edge reference spectra of MnF₂, Mn₂O₃, and MnO₂. (H) Linear combination of pristine and 1st charged samples using reference spectra.

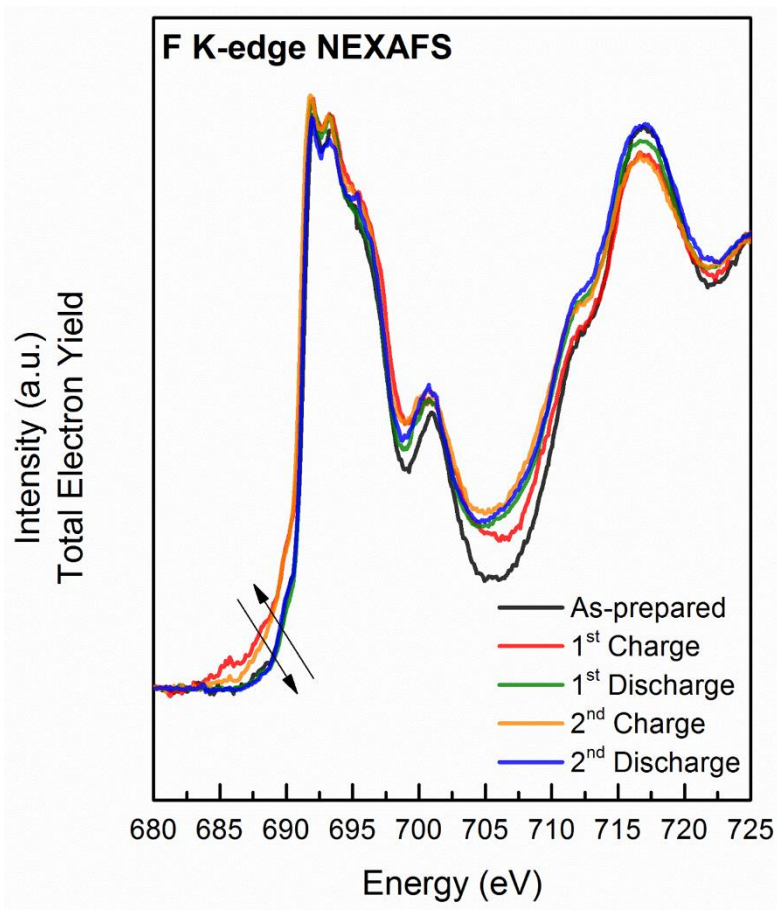


Figure 2.17. F K-edge XAS spectra of LiF-MnO nanocomposite with different electrochemical states.

2.3.4. Surface concentrated chemical and structural changes

The chemical distribution information for the charged and discharged states was obtained using scanning transmission electron microscopy coupled with electron energy-loss spectroscopy (STEM-EELS) spectrum images (Figure 2.18 (A) and (C)). We minimized the electron beam dose with optimized conditions (Figure 2.19). We observed both Mn and F signals from the charged and discharged states and confirmed that the F⁻ ion distribution was not homogeneous but preferentially occurred on the MnO surface. It was generally observed that the fluorine distribution was mainly concentrated on the surface of the particle with 2 ~ 5 nm thickness regardless of the charge and discharge state for the most of the particles, which indicates that the electrochemical reaction with fluorine occurs relatively homogeneously on the surface of the electrode material (Figure 2.20). This trend is different from that for the iron-based oxyfluoride phase, which has a core-shell structure with an O-rich shell and F-rich core²². F coexists with Mn in the surface region in the charged state; however, they tend to exist separately in the discharged state. This result is possibly due to the reversible interaction between Mn and F during electrochemical cycling. Therefore, we compared the valence of Mn in the F-rich shell and F-less core region to clarify the reversible interaction between Mn and F (Figure 2.18 (B) and (D)). A significant change in the Mn-L₃ peak energy was observed in the Mn-L_{2,3} EELS spectra in the charged state. The Mn-L₃ peak observed for the F-rich shell (641.0 eV) has a higher value than 639.8 eV for the F-less core; however, the peak energies from both the shell and core regions were similar in the

discharged state. At charged state, Mn-L edge spectra of shell and core region are analyzed using white line ratio method (L_3/L_2) to compare the oxidation state quantitatively. The shell region has 3.2+ average oxidation state meanwhile core region has 2+ oxidation state. The non-uniform Mn valence distribution across the single particle in the charged state supports the surface-concentrated Mn redox reaction (Figure 2.21). This finding indicates that the F^- ion incorporation accompanying the redox reaction of Mn ions mainly occurs on the MnO surface.

Upon charge, significant local structure evolution was observed including attenuation of rock salt signature and decrease of bond distance from *in situ* extended X-ray absorption fine structure (EXAFS) analysis (Figure 2.18 (E)). X-ray diffraction of the electrode materials do not provide insight on the nature of charged/discharged product due to the loss of long range ordering during the first charge (Figure 2.22). Meanwhile, EXAFS showed evident local structure changes during electrochemical cycling. The signal at longer distances (4–6 Å) gradually decreased at initial charging, indicating a reduction in crystallinity. In addition, electrode undergo the decrease of bond distances at the first and second neighbor. Shorten bond distance of the first neighbor at charge is similar to manganese compounds which have higher oxidation state than Mn^{2+} (Figure 2.23). At the end of charge, the electrode showed completely different local structure from pristine state with attenuated second neighbor²³⁻²⁶. This amorphization and attenuation of the rock salt phase signature were similarly observed in the iron oxyfluoride system during the phase transformation from rock salt to the F-rich rutile phase when

fluorine interacts with the rock salt phase through the reversion reaction²⁶. However, the charged state of the LiF–MnO nanocomposite exhibits a distinct local structure from the rutile-type manganese fluoride phase and retained the cubic local structure similar to the MnO_x phase (Figure 2.23).

The reversible recovery of the local structure as the rocksalt phase was demonstrated after the discharge. The electrode at the end of discharge exhibits similar features to those of the pristine electrode in the local range of 1–6 Å. The first and second neighbor recovered similarly to those in the as-prepared MnO, and the peaks in the 4–6 Å range reemerged, implying the reformation of the MnO-like crystal structure. The local structure of the discharged state was well matched with the standard rocksalt phase MnO model, suggesting that the structural transition is reversible during electrochemical cycling (Figure 2.18 (E) and Figure 2.24). This reversible behavior was observed continuously during the subsequent electrochemical cycling.

A reversible local structure change was observed on the MnO surface in high-resolution high-angle annular dark-field (HAADF) images (Figure 2.18 (F) and (G)). The atomic resolution image of the charged state reveals the different atomic structure in the F-rich shell region compared with that in the F-less core region. The fast Fourier transformation (FFT) image of the core region reveals a periodic pattern projected to the $[0\bar{1}1]$ zone axis of $Fm\bar{3}m$ MnO, which indicates that the core region is well maintained as the MnO phase. Meanwhile, an additional pattern with a large d-spacing (5.02 Å) was observed in the shell region. The local structure is

analogous to the $I4_1/amd$ space group Mn_3O_4 structure considering the crystallographic orientation $[0\bar{1}1]$ zone axis of $Fm\bar{3}m$ MnO , which is coherent with the $[010]$ zone axis of the $I4_1/amd$ space group Mn_3O_4 (Figure 2.25). However, the surface structure was defectively formed, including a vacancy on the Mn tetrahedral site of Mn_3O_4 (Figure 2.18(F)). This result may be due to the instability of Mn^{3+} or Mn^{4+} ions in tetrahedral sites compared with octahedral sites considering the oxidized environment of the surface region by F^- ion incorporation²⁷.²⁸ This face centered cubic (FCC) to body centered tetragonal (BCT) phase transition is known for the diffusionless transformation²⁹, which indicates that the transformation kinetics could be sufficiently fast to accommodate the high current density during the electrochemical cycling (Figure 2.10). Given the coherent distribution of the structure transformed region and F^- ions (Figure 2.18 (A), Figure 2.26), the surface local structure of the charged state is expected to be a defective Mn–O–F-type spinel-like phase. In contrast to the charged state, the discharged electrode exhibited a uniform structure even in shell region as the MnO rock salt phase (Figure 2.18 (G), (H), and Figure 2.27).

This reversible structure evolution is identical to the results from *in situ* EXAFS. Because the thickness of shell region is approximately 2 ~ 4 nm (Figure 2.18 (A) and (F)), if we assume the particle size of MnO as 10 nm, the surface layer occupy 78.4 % of the MnO single nanoparticle (Figure 2.28). Therefore, the local structure change from the *in situ* EXAFS can be originated from the structure evolution on the MnO surface considering the particle size level.

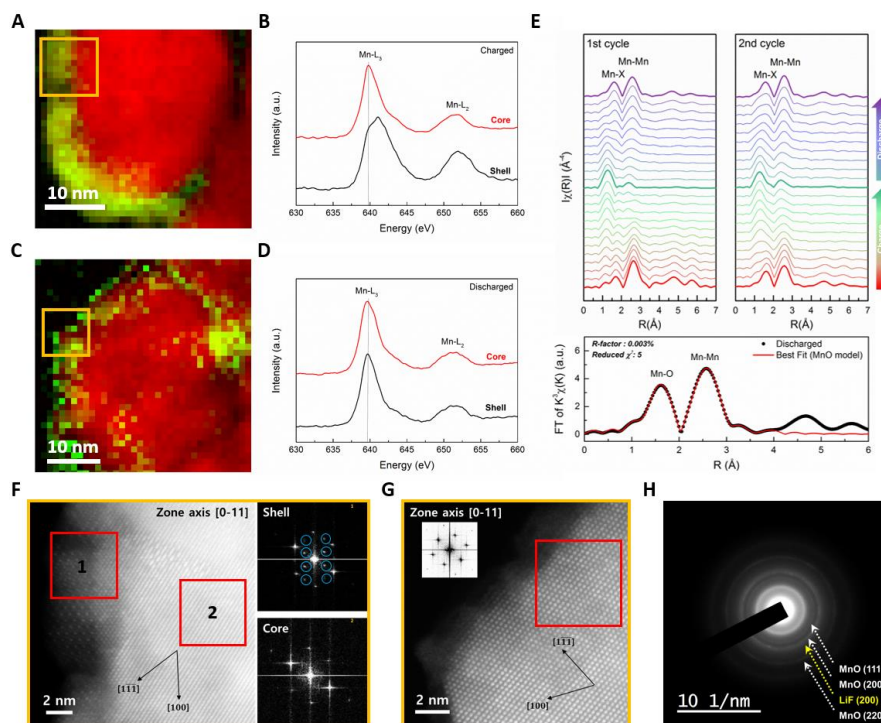


Figure 2.18. Surface concentrated F^- ion interaction including structural evolution (A, C) STEM–EELS images of LiF–MnO nanocomposite in charged and discharged state for the elemental distribution of F (green) and Mn (red). (B, D) EELS spectra of Mn $L_{2,3}$ edges recorded from the shell and core regions of charged and discharged states. (E) In situ EXAFS spectra during two cycles in the 1.5–4.8 V range. The first charge is operated in the 3.0–4.8 V range. EXAFS data and best-fit model for discharged electrode. (F) High-resolution HAADF image of charged state (4.8 V) and (G) discharged state (1.5 V) from yellow box in (A) and (C). The FFT pattern was obtained from the red box. The blue circles indicate an additional FFT pattern compared with the core region. (H) Diffraction pattern of an electrode discharged to 1.5 V.

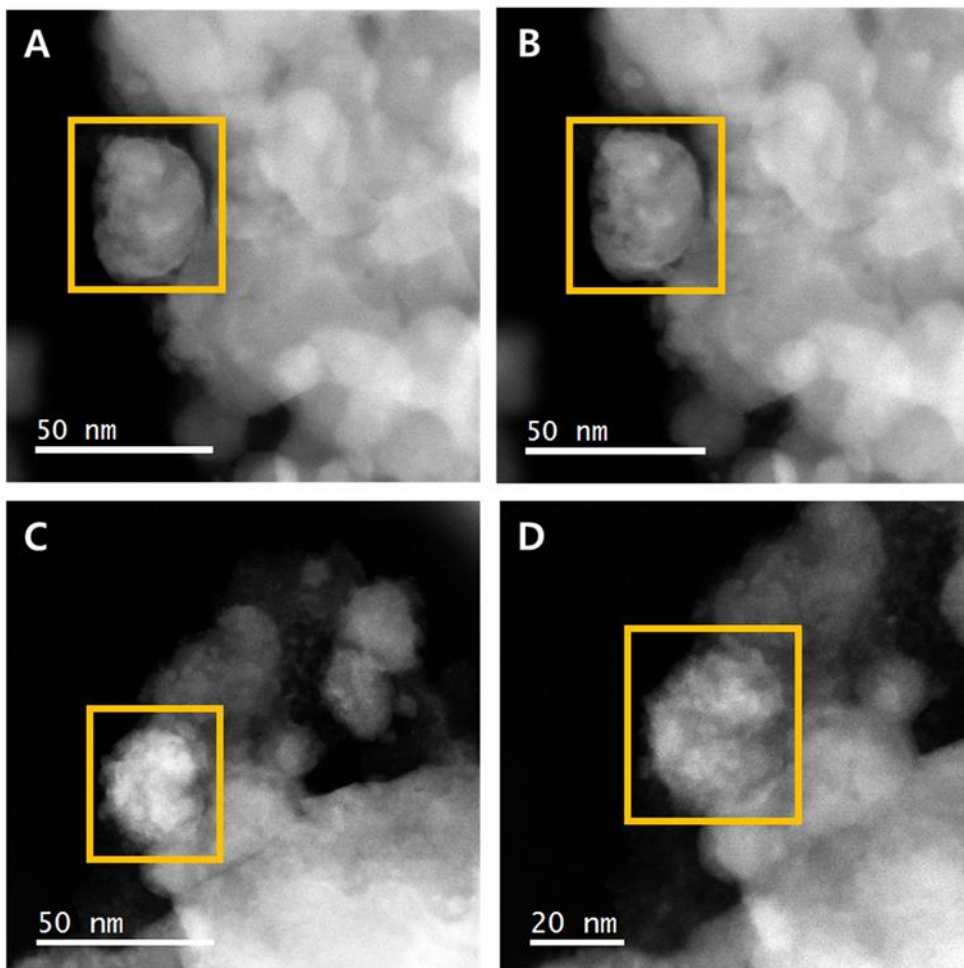


Figure 2.19. Stability of LiF–MnO nanocomposite under electron beam exposure. (A, C) ADF image of LiF–MnO nanocomposite at charged/discharged state before EELS spectrum collection. (B, D) ADF image after EELS spectrum collection (after 2 h).

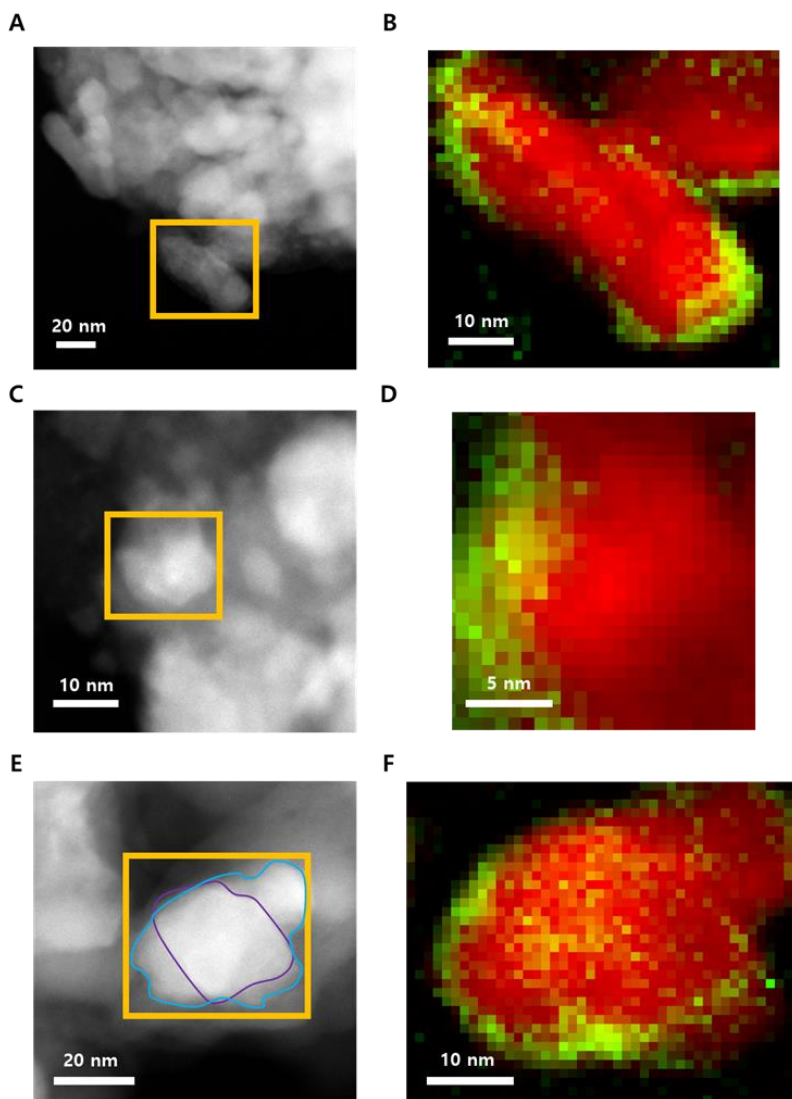


Figure 2.20. ABF and STEM-EELS image of LiF-MnO nanocomposite. (A-D) Charged (4.8 V) and (E, F) discharged (1.5 V) state of LiF-MnO nanocomposite. (F: green, Mn: red) Yellow box shows the location that STEM-EELS measurement was performed. Blue and purple line indicate individual particles.

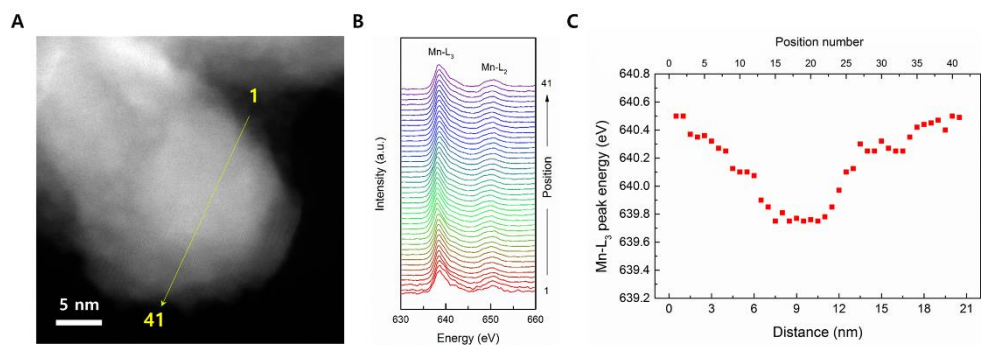


Figure 2.21. Chemical and electronic structure of LiF-MnO nanocomposite at charged state. (A) ADF image of LiF-MnO nanocomposite. (B) EELS spectra of Mn L_{2,3} edges recorded as position following the green arrow in (A). (C) Mn-L₃ peak energy as position.

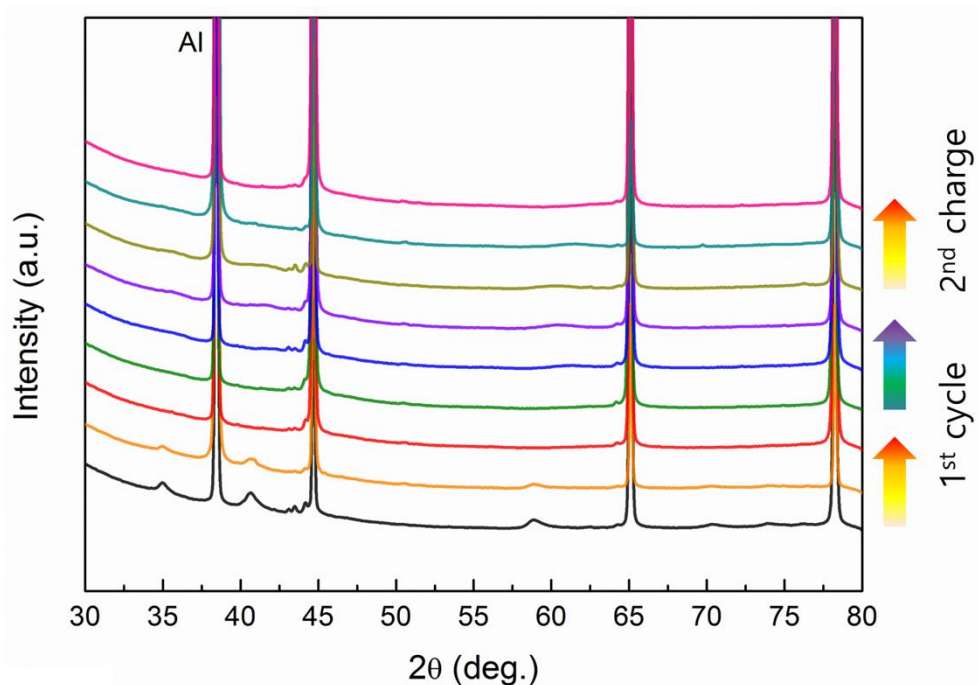


Figure 2.22. *Ex situ* X-ray diffraction patterns of the LiF-MnO nanocomposite from the first charge to second charge.

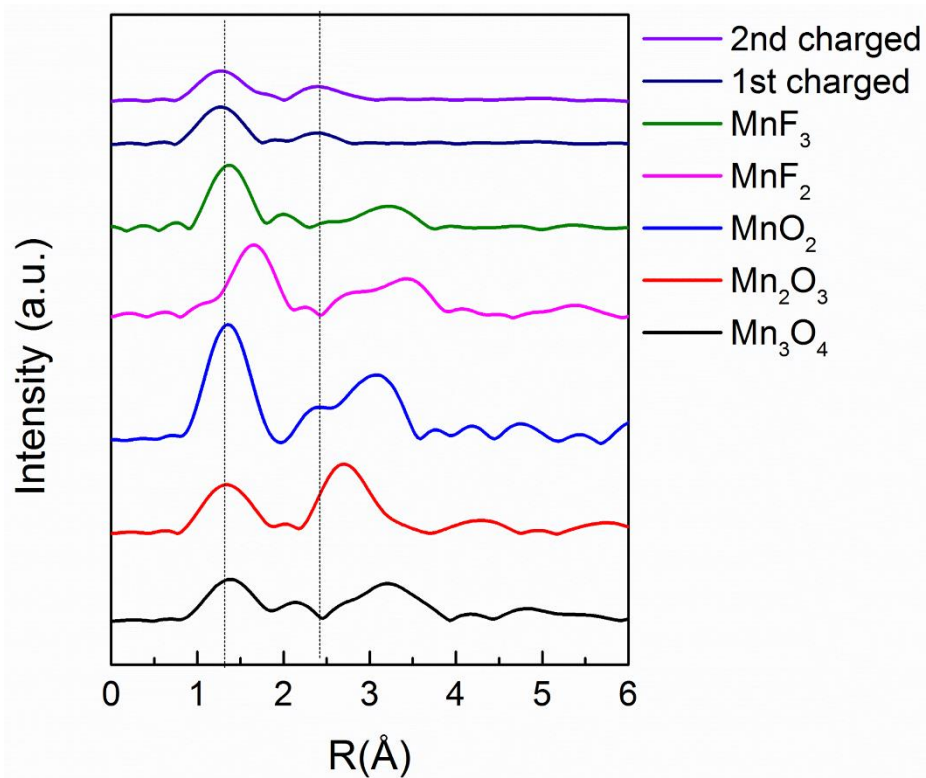


Figure 2.23. Fourier transformed EXAFS at Mn K-edge of various manganese compounds.

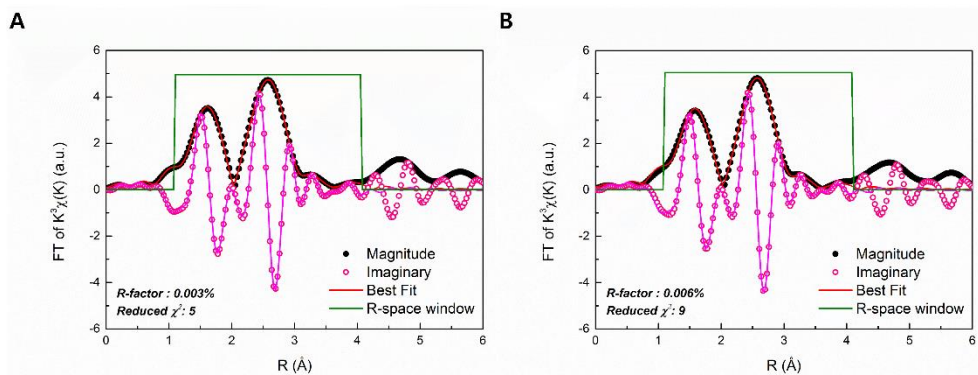


Figure 2.24. Fourier transformed magnitude (black), imaginary part (pink), and best-fit (red) model for the discharged electrode. (A) 1st discharged and (B) 2nd discharged electrode.

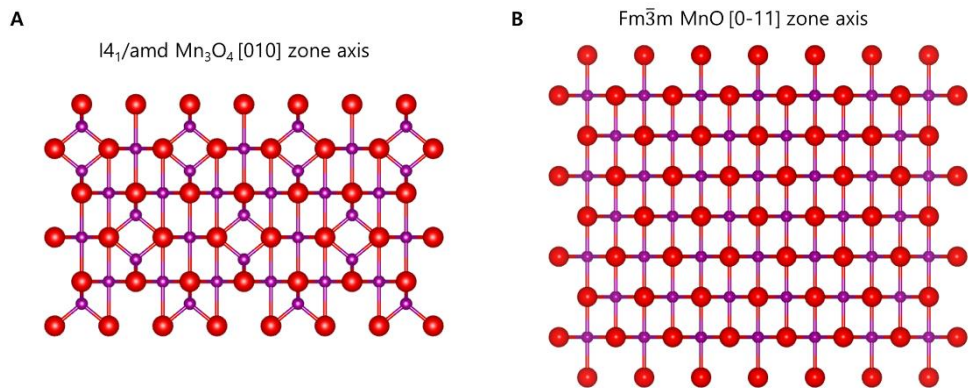


Figure 2.25. Crystal structure of (A) Mn_3O_4 and (B) MnO along the coherent crystallographic orientation.

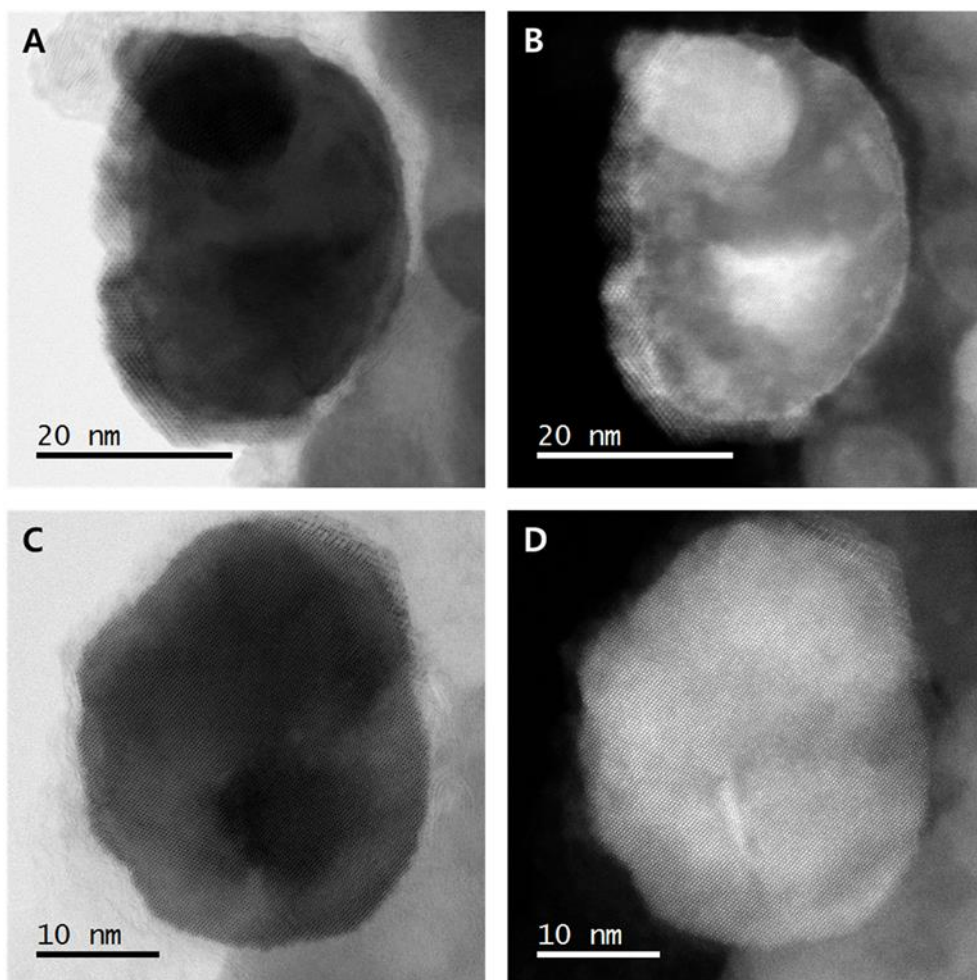


Figure 2.26. BF and ADF of STEM image of LiF-MnO nanocomposite. (A, B) First charged to 4.8 V. (C, D) Discharged to 1.5 V after the first charge.

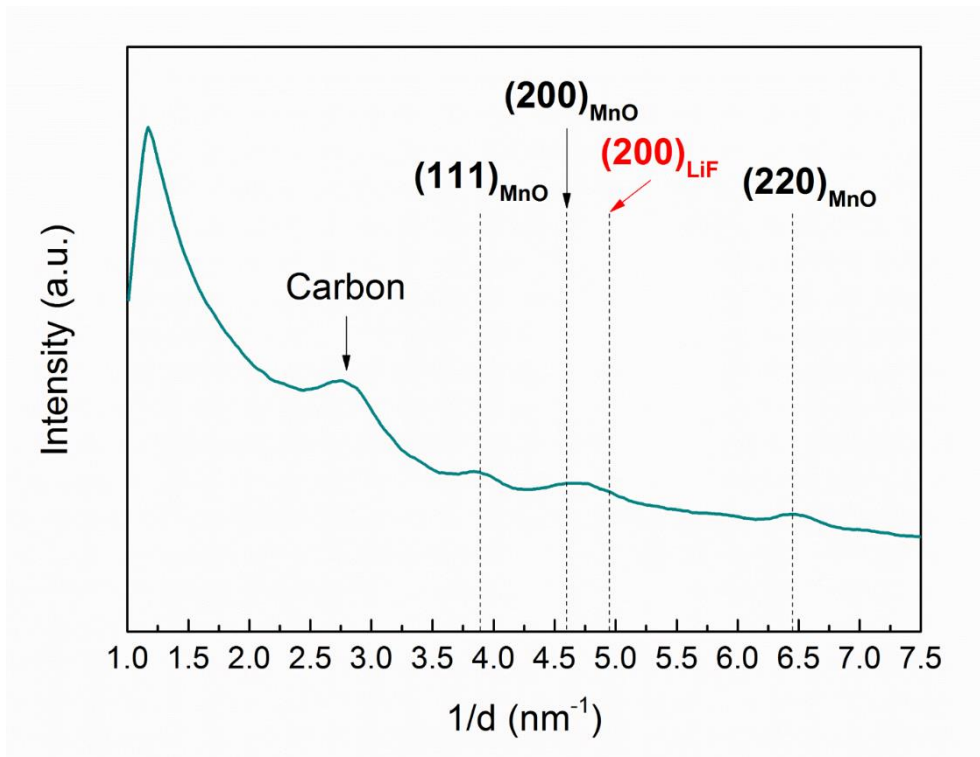


Figure 2.27. Brightness intensity map of the diffraction ring pattern in Figure 2.18H from the center of the transmission electron beam.

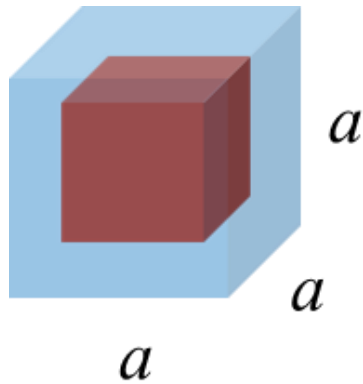


Figure 2.28. MnO nanoparticle (cube shape). Assuming that 2 nm surface region (blue) undergoes the significant structural reordering in a nm size of the cubic particle, the volumetric portion of the blue region is calculated by the equation $\{a^3 - (a-2)^3\}/a^3$.

2.3.5. Particle size effect on electrochemistry

Simple numerical calculations, assuming the involvement of the Mn redox reaction up to 2 nm from the MnO surface, confirm the feasibility of a large capacity (>236.37 mAh/g) for sub-micrometer-scale particles (~10 nm). Based on the simplified model from the first-principles calculations, the capacity could be numerically predicted as a function of the particle size of MnO (Figure 2.29-2.32) Supplementary text). In particular, the large capacity from the surface reaction was feasible because of the two-electron reaction of the Mn ion ($\text{Mn}^{2+}/\text{Mn}^{3+}$ and $\text{Mn}^{3+}/\text{Mn}^{4+}$) on the MnO surface (Figure 2.31). In the simulation, we observed that the capacity can be dramatically increased as the particle size decreases below 10 nm because of the larger surface area of the small-particle electrodes compared with large-particle ones. Our experimental results for the capacity (~240 mAh/g) with ~10-nm particle sizes match with the capacity predicted based on the numerical simulations (Figure 2.32).

The particle size effect of the metal compound on the electrochemical activity in the nanocomposite cathode material was verified with systematic control of the particle size and shape of manganese oxide (Figure 2.33 (A), Figure 2.34). Mn_3O_4 was selected as the metal oxide compound to compare the electrochemical activity as a function of particle size. A LiF-C/ Mn_3O_4 nanocomposite electrode was fabricated by making a mixture with LiF-C and as-synthesized Mn_3O_4 nanoparticles without additional high-energy ball milling³⁰. LiF and Mn_3O_4 were well mixed in the carbon matrix without a change in particle size or morphology (Figure 2.33 (B),

Figure 2.35). The LiF–C/Mn₃O₄ mixture exhibited electrochemical activity as a cathode material with a 3.5-V average voltage redox reaction after the first charge (Figure 2.36). The capacity increased from 96 to 159 mAh/g as the particle size decreased from 20 to 6 nm (Figure 2.33 (C)). This result indicates that the particle size of Mn₃O₄ directly affects the capacity of the LiF–C/Mn₃O₄ nanocomposite cathode and implies that the particle size of metal compounds can be a feasible tool for tuning the capacity in the nanocomposite cathode material system.

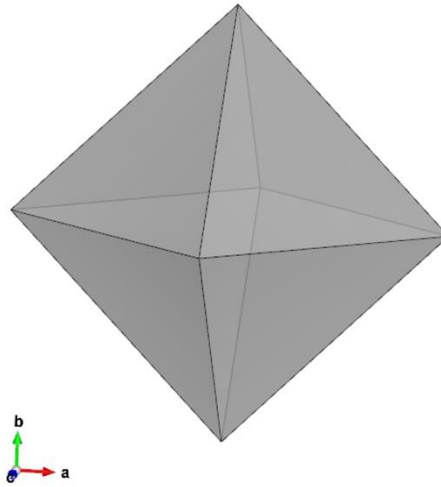


Figure 2.29. Wulff construction of MnO. Only the (111) surface appeared in the equilibrium shape. (See supplementary text.)

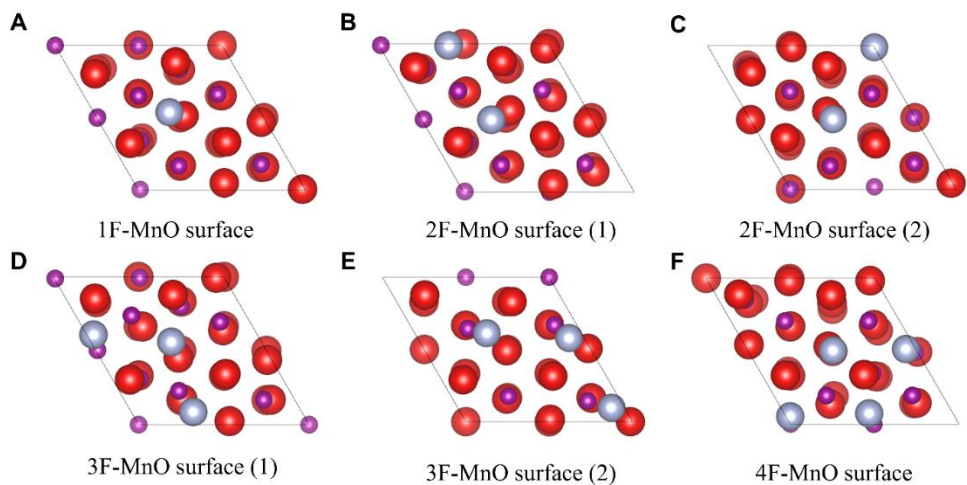


Figure 2.30. Fluorine absorption on the MnO (111) surface. **(A)** 1 F atom absorption, **(B, C)** 2 F atom absorption, **(D, E)** 3 F atom absorption, **(F)** and 4 F atom absorption in the (111) surface unit cell of MnO. (Red: O, Gray: F, Purple: Mn) (See supplementary text.)

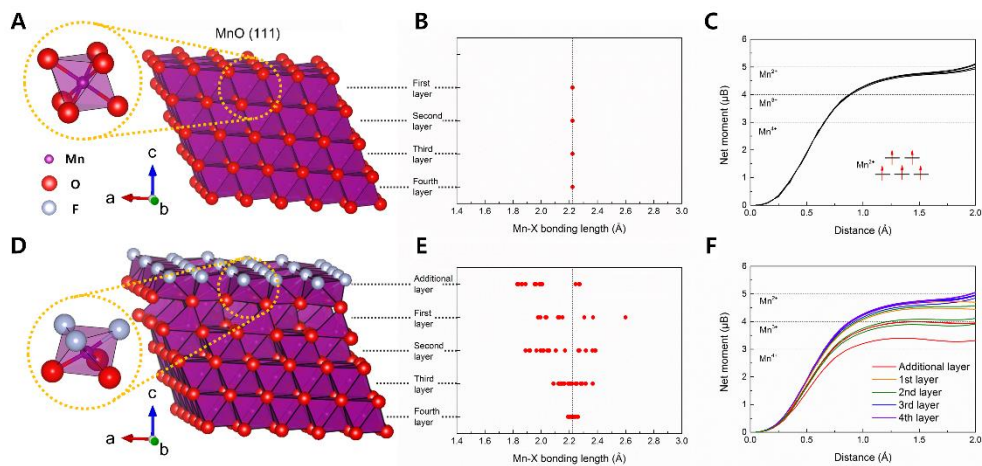


Figure 2.31. (A) Crystal structure of MnO. (B) Bond length between the Mn and oxygen of each octahedron. (C) Integrated spin as a function of the radius around Mn in MnO. (D) Fluorinated MnO crystal structure after fluorination on the (111) plane of MnO. (E) Bond lengths between the Mn and anions (O and F) of each Mn octahedron. The top layer indicates the newly formed Mn octahedron after jumping up to bond with a fluorine ion. (F) Integrated spin as a function of the radius around Mn in fluorinated MnO. Mn was oxidized up to the third layer as a result of fluorination. (See supplementary text)

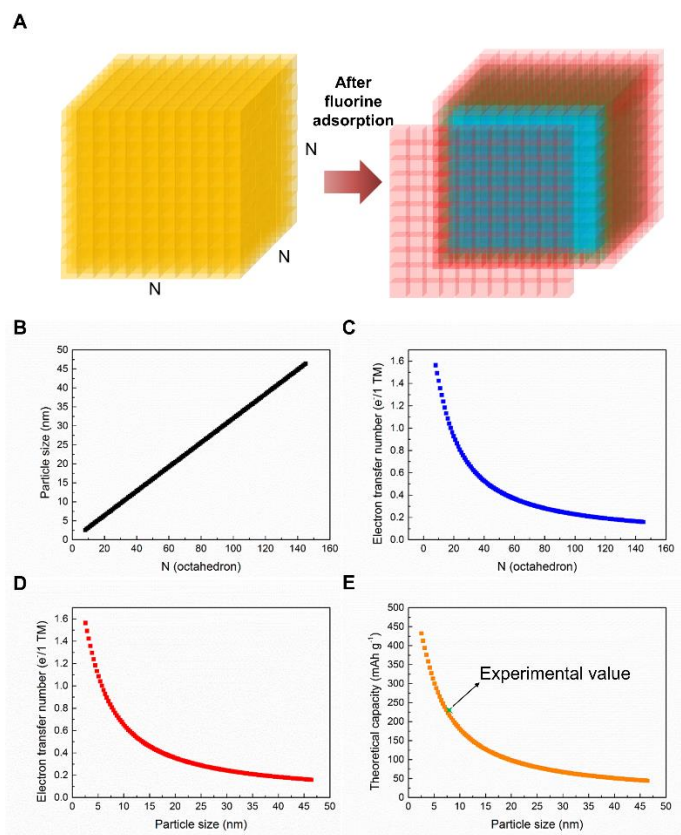


Figure 2.32. Simple model of numerical calculation for capacity of LiF-MnO nanocomposite as a function of the particle size of MnO. **(A)** The metal oxide (MO) is assumed to be composed by an $N \times N \times N$ octahedron cube (MO₆) by considering the similarity with the closed-packed structure. **(B)** Particle size as a function of the number of octahedron (N). **(C)** Electron transfer number as a function of the number of octahedron (N). **(D)** Electron transfer number as a function of particle size. **(E)** Correlation between the particle size and capacity of LiF-MnO nanocomposite based on the numerical calculation. The experimental capacity matches well with the prediction based on the numerical calculation.

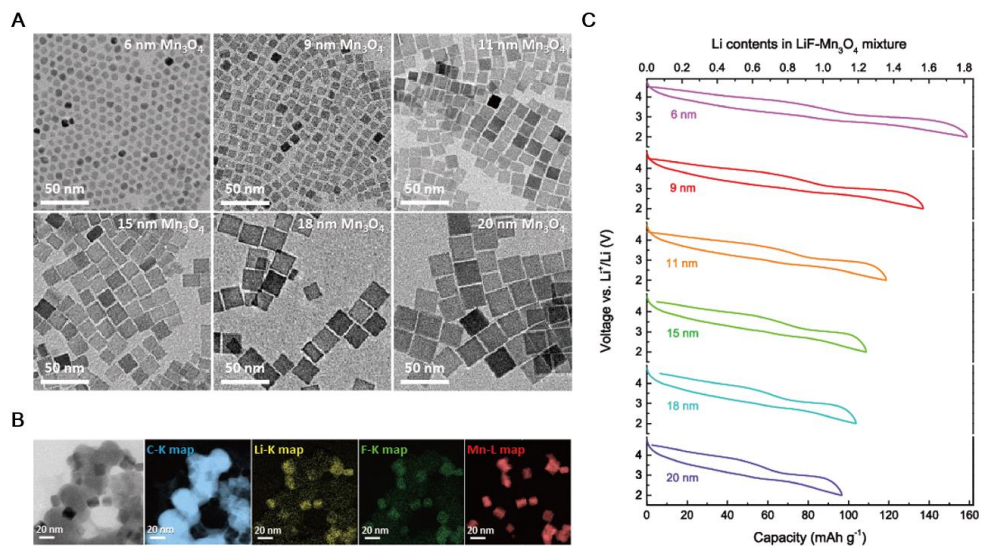


Figure 2.33. Capacity-tunable $\text{LiF-C/Mn}_3\text{O}_4$ nanocomposite cathode materials
 (A) TEM image of Mn_3O_4 nanoparticles. (B) TEM and EFTEM images of $\text{LiF-C/Mn}_3\text{O}_4$ (15 nm) mixture electrode in as-prepared state. (C) Electrochemical profile of $\text{LiF-C/Mn}_3\text{O}_4$ nanocomposite with various particle sizes after the first charge.

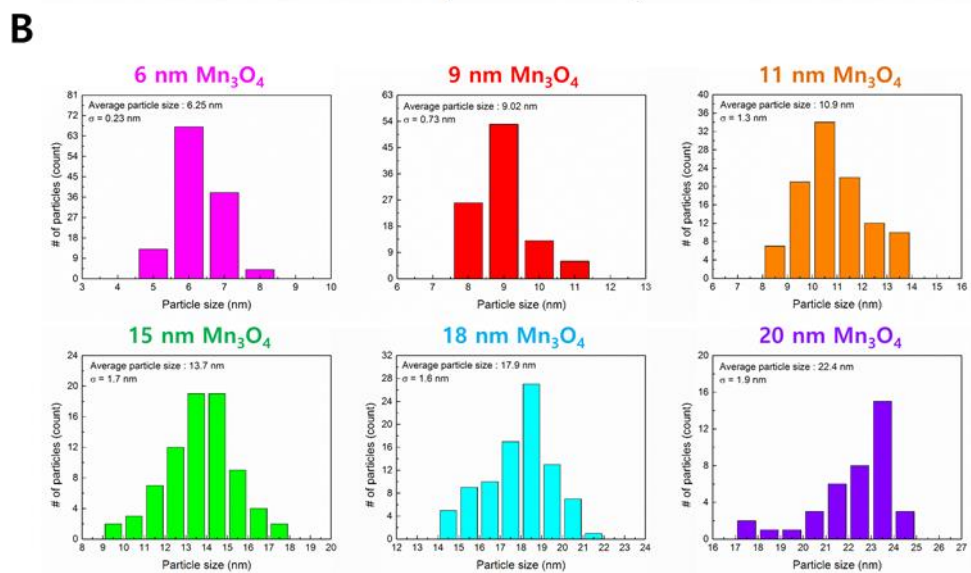
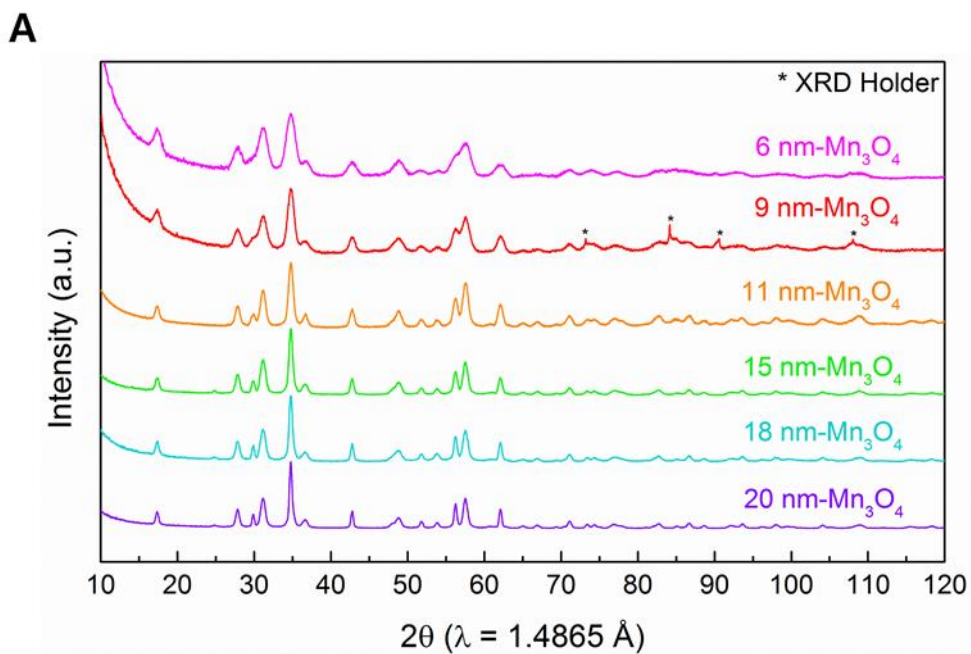


Figure 2.34. (A) High-resolution powder diffraction of Mn₃O₄ nanoparticles. (B) Average particle size and size distribution of Mn₃O₄ nanoparticles.

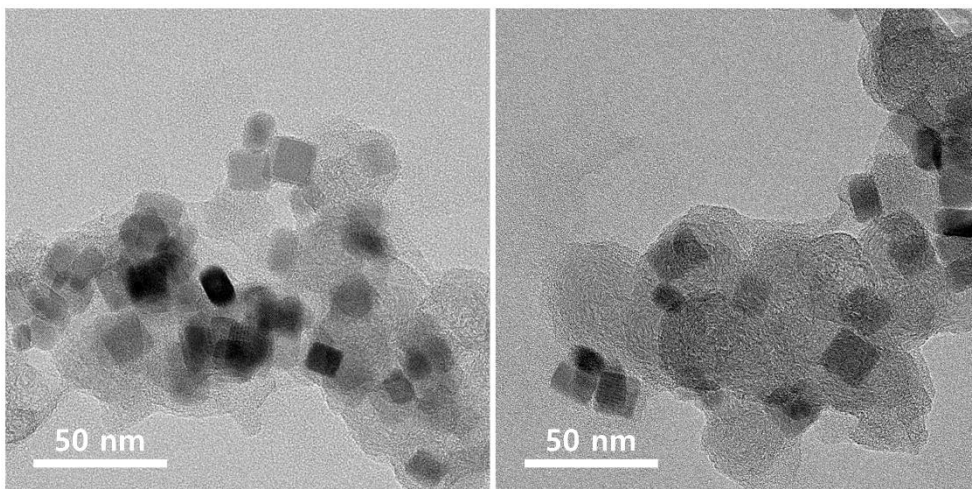


Figure 2.35. Transmission electron microscopy image of LiF-C/Mn₃O₄ mixture electrode. Particle size of Mn₃O₄ nanoparticle is 15 nm.

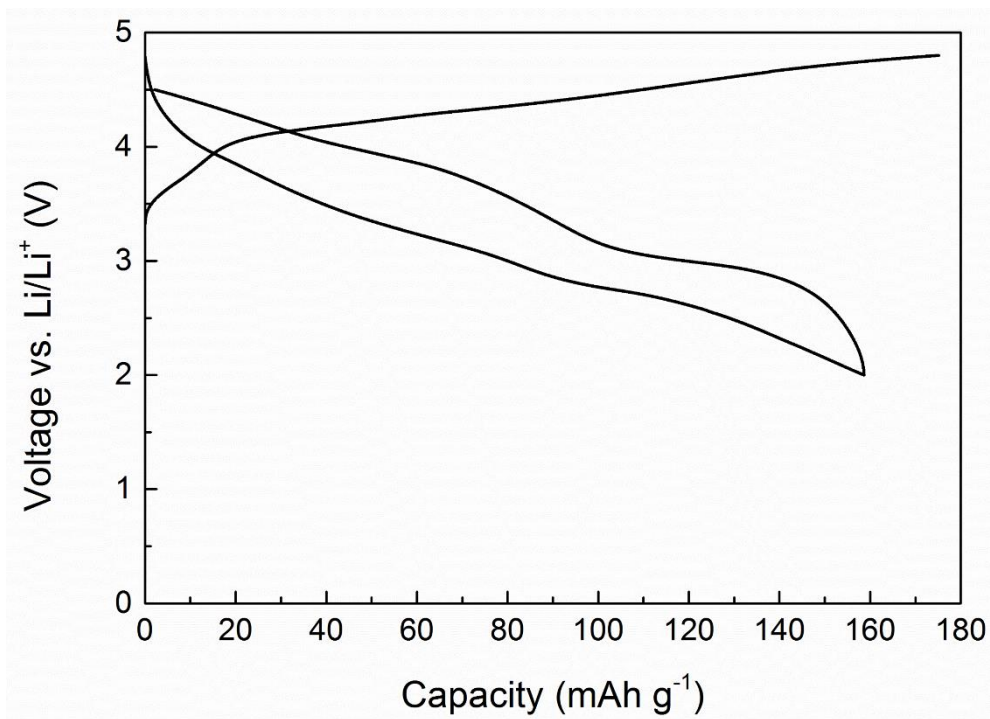


Figure 2.36. Electrochemical profile of LiF-C/Mn₃O₄ mixture electrode with the first charge. Particle size of Mn₃O₄ nanoparticle is 6 nm.

2.3.6. Reaction mechanism

Therefore, the reaction mechanism of the LiF–MnO nanocomposite can be called a “surface conversion reaction”, which is described as follows:



The surface conversion reaction ($\text{MX} + \text{LiA} \leftrightarrow \text{MX–A} + \text{Li}$) can take advantage of the high valence redox reaction of transition metals because the capacity of the LiF–MO nanocomposite is fully utilized based on the $\text{M}^{2+}/\text{M}^{3+}$ or $\text{M}^{3+}/\text{M}^{4+}$ redox reaction. The transition metal is always housed by the anion (by the X anion in the discharged state or by X and A anions in the charged state) in this reaction and can thus maintain the high-valence state offered by the anions and the high-voltage operation of the electrode. LiF functions not only as a Li source for cathode materials but also as an anion source for charge compensation when the oxidation and reduction of a transition metal ion occur. LiF can be regarded as a stabilizer of the oxidized Mn^{3+} (or Mn^{4+}) ion by providing F^- ions from the MnO perspective. In addition, the MnO can be regarded as an assistant that promotes the decomposition of LiF. LiF is difficult to decompose electrochemically as itself because it is a stable ionic compound with a substantially large formation energy corresponding to 6.10 V vs. Li^+/Li (Table 2.1). It is expected that the electrochemical activity of the LiF–MnO nanocomposite originates from a series of reactions in which a slightly oxidized $\text{Mn}^{(2+\delta)+}$ ion is formed by the extraction of an electron during the initial charge, followed by the decomposition of LiF. Therefore, LiF can donate the F^- ion to stabilize the oxidized Mn ion of Mn^{3+} or Mn^{4+} when it decomposed. This process

can only occur when LiF and MnO compounds are intimately well mixed on the nanoscale.

We found that the reaction mechanisms of LiF–MO (M=Fe, Co) nanocomposites are different compared to the case of LiF–MnO. (See supplementary information for details.) Both LiF–MO (M=Fe, Co) nanocomposites showed electrochemical activity based on the M^{2+}/M^{3+} redox reaction, which was enabled by the interaction with fluorine ions. However, specific fluorine ion behavior was slightly different depending on the transition metal compound. In the LiF–FeO case, fluorine ions were better incorporated into the host structure due to the thermodynamic stability of the FeOF compound. As a result, this formulation showed remarkably similar electrochemical properties and local structure changes to those of Li_xFeOF (Figure 2.37–2.39, supplementary text) during subsequent discharge and charge^{25,26}, similar to our previously reported case of LiF–FeF₂, which can be termed a “host formation reaction”⁴. In the case of LiF–CoO, although the trend of change in oxidation state and local structure is similar to the case of LiF–MnO, the changes are relatively small compared to the reversible capacity (Figure 2.40 and 2.41). It implies that LiF–CoO could have different charge compensation mechanism including not only Co redox reaction but also other reaction mechanisms, which needs to be revealed by in-depth study as future work. This difference in reaction processes can be determined by whether the fluorinated phase of the initial metal compound occurs. Note that the iron oxyfluoride phase exists, while the manganese or cobalt oxyfluoride phase has not been reported³¹. The interaction

behavior of the F^- ion with metal compounds and the thermodynamic stability of the charged form seem to determine the overall reaction mechanism.

Table 2.1. Formation energy of lithium compounds at 298.15 K

Li compounds	Formation energy at 298.15 K (kJ mol⁻¹)	Potential from Nernst equation (V)
LiF	-588.660	6.10
LiCl	-384.019	3.98
LiBr	-341.630	3.54
LiI	-269.665	2.79
LiOH	-438.958	4.55
Li₂O	-562.102	2.91
Li₂O₂	-570.954	2.96
Li₃N	-128.640	0.44

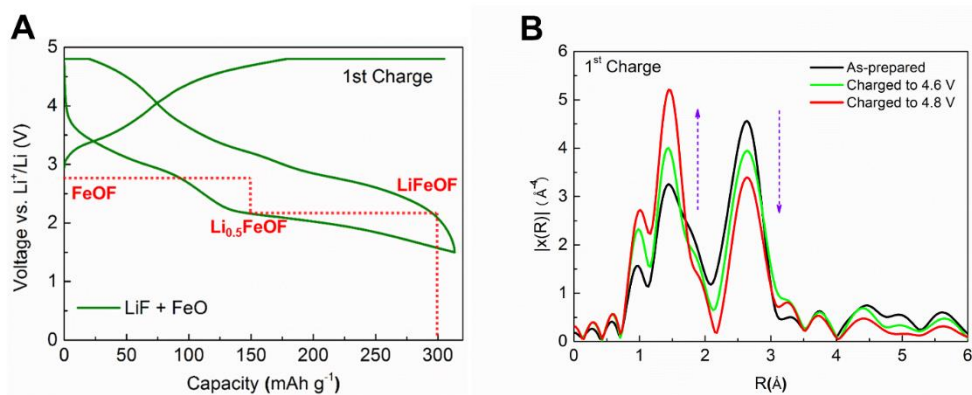


Figure 2.37. (A) Electrochemical profile of the LiF–FeO nanocomposite until the second charge. Red dashed line indicates the reaction voltage of Li_xFeOF estimated by first-principles calculation⁴⁴. (B) *Ex situ* EXAFS spectra of the LiF–FeO nanocomposite during the first charge.

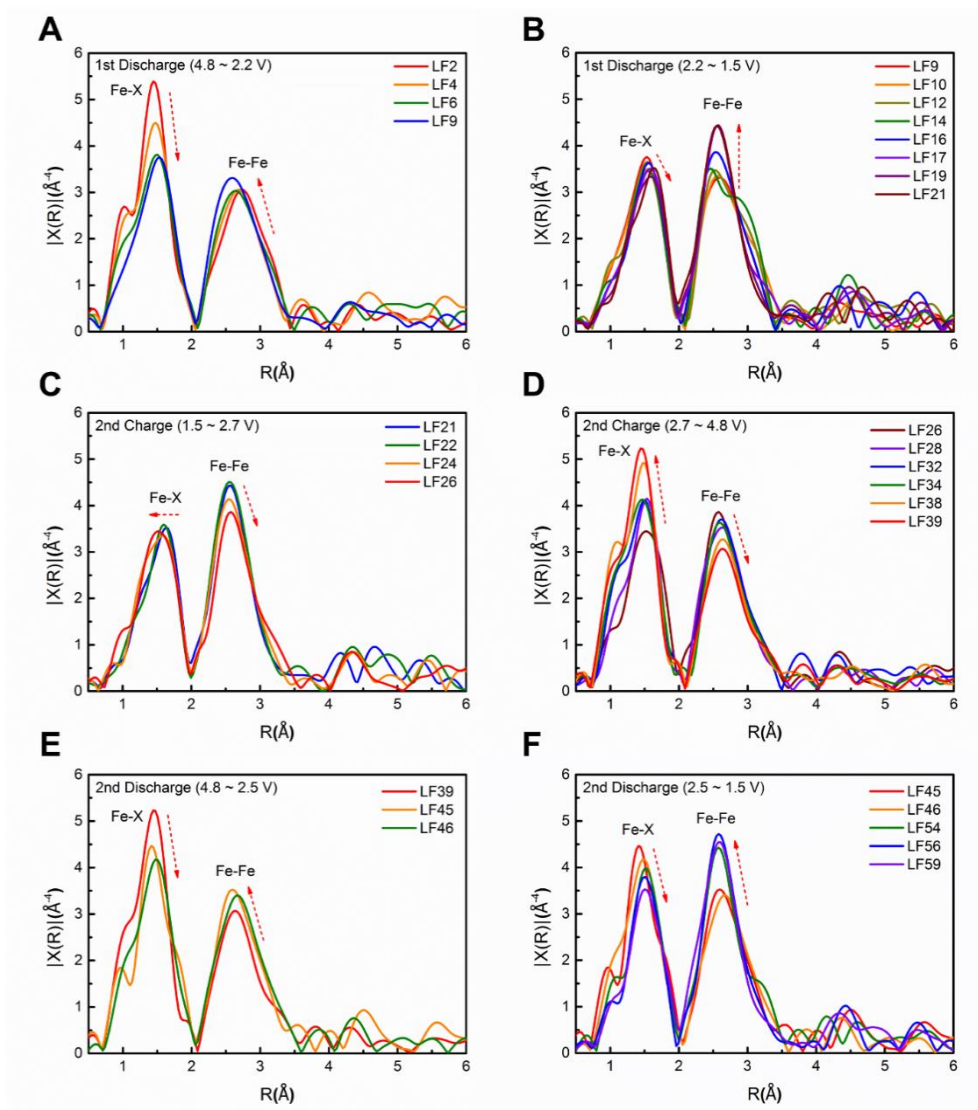


Figure 2.38. *In situ* EXAFS spectra of the LiF–FeO nanocomposite during charge and discharge in the 1.5–4.8 V voltage range. (See supplementary text.)

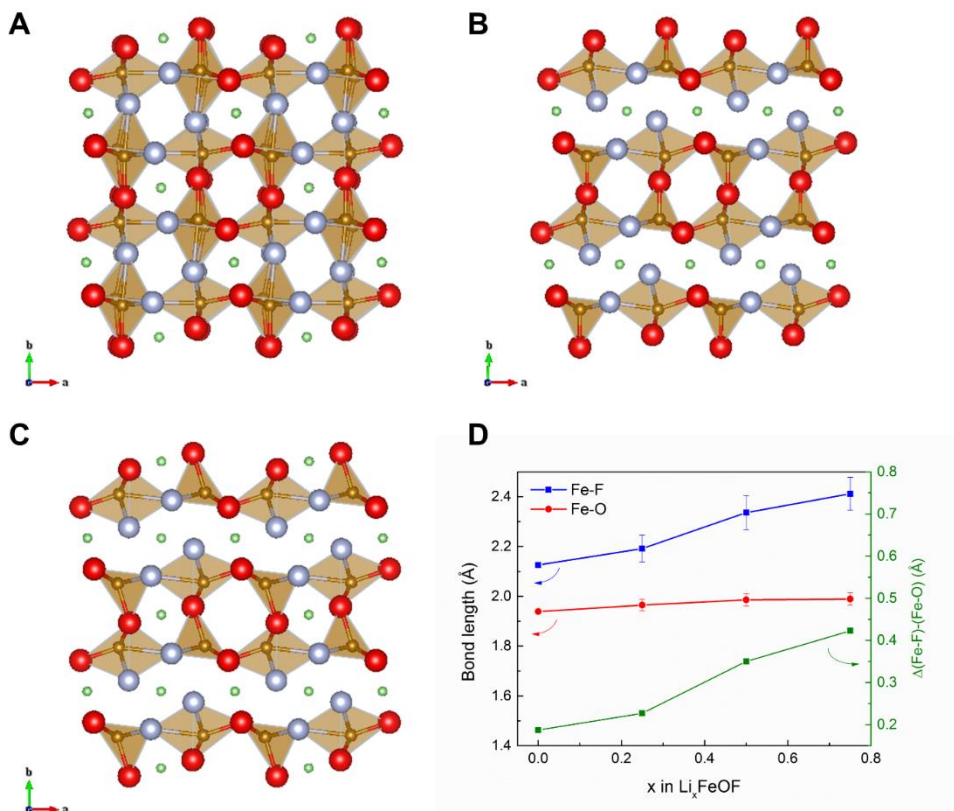


Figure 2.39. Structure of (A) $\text{Li}_{0.25}\text{FeOF}$, (B) $\text{Li}_{0.5}\text{FeOF}$, and (C) $\text{Li}_{0.75}\text{FeOF}$ in the [001] *c*-axis projection. Bond cutoff length was set to 2.6 Å. (D) Average bond length between Fe and anions (O, F) (left axis) and bond length between Fe–F and Fe–O (right axis) as change in the lithium content in the Li_xFeOF structure. (See supplementary text.)

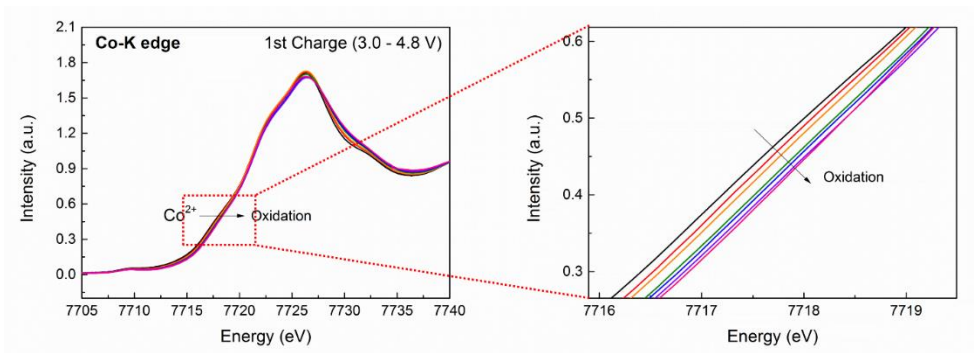


Figure 2.40. *Ex situ* XANES spectra of the LiF–CoO nanocomposite at the Co–K edge during the first charge. The XANES shift was small during the charge in the CoO case compared with MnO and FeO. Although the chemical shift of the Co–K edge was small, 0.5 eV, it should be noted that this value is comparable to the chemical shift (0.9 eV) in Li_xCoO_2 ($0 < x < 0.83$), which may imply that the small shift is a chemical characteristic of Co ions in oxide environments¹⁰. Nevertheless, the clear chemical shift of the Co–K edge, similar to the case of Li_xCoO_2 ($0 < x < 0.83$), indicates that the Co ion redox reaction participates in the reversible electrochemical reaction in the LiF–CoO nanocomposite. Given the relatively small chemical shift value of the Co K–edge in the LiF–CoO nanocomposite compared with the reversible capacity, the capacity of the LiF–CoO nanocomposite could originate from other charge compensation mechanisms, including anion-hybridization of Co ion and the anionic redox reaction.

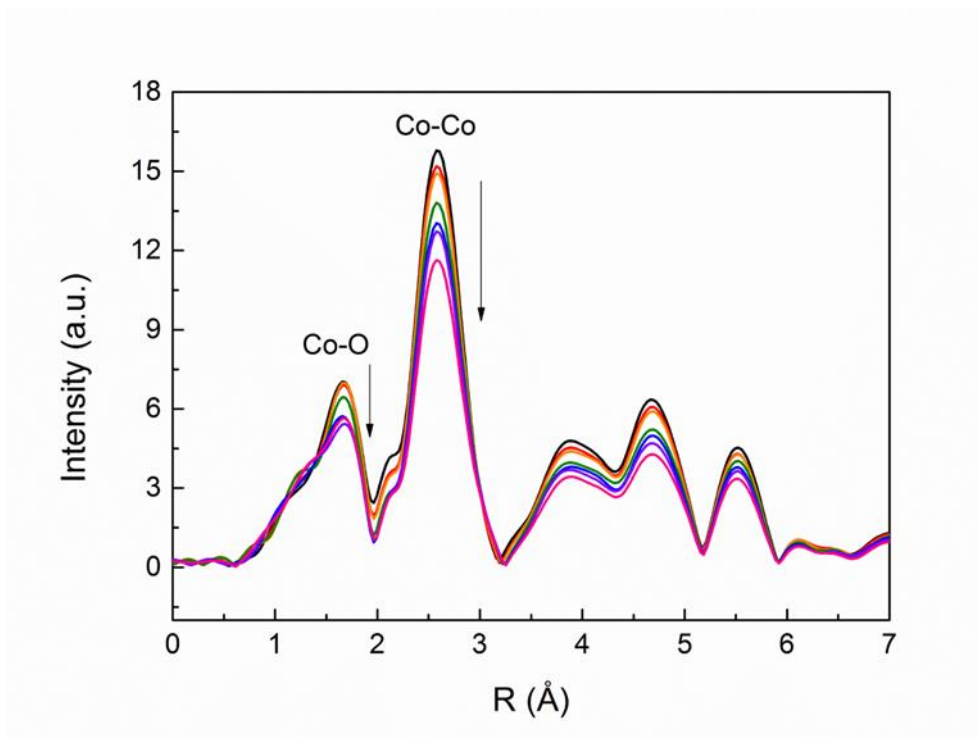


Figure 2.41. Ex situ EXAFS spectra of the LiF-CoO nanocomposite at the Co-K edge during the first charge.

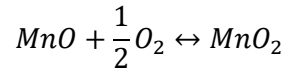
2.3.7. Supplementary text and discussions

2.3.7.1. Surface energies and Wulff shape of MnO

After the convergence test, we found that a vacuum thickness of $>10 \text{ \AA}$ and slab thickness of $>20 \text{ \AA}$ maintains energy convergence within 1 meV/\AA^2 . Surface energies of MnO were calculated using the following formulation,

$$\gamma_{MnO} = \frac{1}{2A} \left[G_{slab} - \frac{1}{2} N_O \cdot G^{bulk} - (N_{Mn} - N_O) \cdot \mu_{Mn}^{bulk} \right]$$

where G_{slab} is the total free energy of the slab supercell, A is the area of the exposed surface, N_O and N_{Mn} are the numbers of oxygen and manganese atoms in the slab, respectively, and μ_O^{bulk} and μ_{Mn}^{bulk} are the chemical potentials of oxygen and manganese in their bulk phases, respectively. The energy of bulk MnO was expressed in chemical potential form to deal with non-stoichiometry. The chemical potential of oxygen was determined by the equilibrium of the following reaction.



The Wulff shape was constructed from surfaces energies, which apparently showed that oxygen terminated (111) surfaces dominated (Figure 2.29). Therefore, we considered only this (111) surface in further calculations.

2.3.7.2. Fluorine atom absorption in MnO surface

Because four Mn atoms were in the first layer of the surface unit cell, we considered 1-4 fluorine absorption in the surface. Figure 2.30 shows all possible fluorine configurations on the (111) MnO surface. We calculated the formation

energy G_f of each absorption state using the following simple equation,

$$G_f = G_{F-MnO} - G_{MnO}^{slab} - n \cdot \mu_F^{LiF}$$

where G_{F-MnO} is energy of each configurations in Figure 2.30, G_{MnO}^{slab} is energy of (111) MnO surface without F absorption, n is the number of F atoms absorbed, and μ_F^{LiF} is chemical potential of fluorine in LiF structure determined by experimental formation energy of LiF. Based on the formation energy calculation, we observed that the 4F-MnO configuration (Figure 2.30F) was more stable than any other F-absorbed configuration in the range of $\mu_F^{LiF} - \mu_F^0 > -5.54$ eV (which corresponds to $P_{F_2} > 3 \cdot 10^{-188}$ atm). This result implies that only the 4F-MnO configuration exists in the experimental environment. Therefore, we only considered this configuration in the structural analysis.

We assumed that F^- ion incorporation occurred on the surface of the MnO crystal. The most stable and dominant surface, the (111) plane, was used to describe surface fluorination as a representative case (Table 2.2). The crystal structure of MnO in the as-prepared state is schematically illustrated in Supplementary Fig. 26A, where Mn octahedra share edges, forming a rock salt structure. All Mn octahedra in the as-prepared oxide have a symmetrical bond length of 2.2 Å between Mn and O atoms, as observed in Figure 2.31B. The oxidation state of the Mn ion was confirmed to be +2 from the integrated spin (5 μ_B) around the Mn atoms (Figure 2.31C).

However, when F^- ions were incorporated on the (111) plane of MnO in Figure 2.31D and 2.31E, the bond lengths between Mn and O, along with the oxidation states, were significantly altered. Some Mn ions located on the top layer jump to the surface and form additional bonds with F^- ions, resulting in an additional top layer of hybrid Mn octahedra formed with oxygen and fluorine (Figure 2.31D). This fluorination on the surface leads to a notable change in the bond lengths and Mn oxidation states, not only in the top layer but also in the layers beneath (up to four subsequent layers), as observed in Figure 2.31E and 2.31F. The bonds between Mn and anions (O, F) were asymmetrically distorted, and the Mn oxidation states were split among the +2, +3, and +4 states from the initial value of +2.

2.3.7.3. Numerical prediction of LiF-MnO capacity as a function of particle size

We assumed that the outermost manganese ion (red) can be oxidized from 2+ to 4+ and that the manganese ions that are within the next two layers below the surface (blue) can offer one electron (Mn^{2+}/Mn^{3+}) based on the first-principles calculations given in Figure 2.31F. The other residual part (green) does not participate in the redox reaction because it is considered as a core far from the surface. We calculated the total number of electrons that can participate in the redox reaction as a function of N. We defined the redox electron number by dividing the total number of participating electrons by the number of overall manganese ions, which can be converted into the gravimetric capacity using the weight of the MnO formula unit. A numerical calculation was performed as follows:

Yellow (overall octahedron): N^3

Red (outermost surface, $2e^-$ redox): $N^3-(N-2)^3$

Blue (Two layers below the outermost surface, $1e^-$ redox): $N^3-(N-6)^3-\{N^3-(N-2)^3\}$

Green (Residual part without red and blue regions, no redox): $(N-6)^3$

Electron number (# e^- /1 TM): $(2*\text{red} + 1*\text{blue})/(\text{yellow}) = (24N^2-120N+224)/N^3$

2.3.7.4. Local structure change of LiF-FeO nanocomposite in electrochemical reaction

Subsequent discharge and charge reactions of the LiF-FeO nanocomposite followed the local structure change of Li_xFeOF (Figure 2.38). During electrochemical cycling, the bond length of the first neighbor (Fe-X) was reversibly increased and decreased by the change in the ionic radius of Fe due to oxidation and reduction, which is shown by most positive electrode materials that can accept the lithium at distinct sites. In addition, the reversible change of intensity of the first neighbor can be attributed to the lithium content of the electrode. In Li_xFeOF , the bond lengths of both Fe-O and Fe-F increase as lithiation occurs. While the variation in the Fe-O bond length is very small, the Fe-F bond length changes dramatically (Figure 2.39). These differing tendencies may trigger asymmetries in the Fe octahedron arising from increases in the bond length difference between Fe-O and Fe-F (green line in Figure 2.39D). Therefore, increasing asymmetry can lead to a decreasing intensity of the first neighbor, as lithiation occurs during discharge. This reversible change was observed during the charge process.

Table 2.2. Formation free energies of the low-index surfaces in MnO

Surfaces	Surface energy (meV/Å²)
(100)	127.7
(110)	70.3
(111)_manganese terminated	166.9
(111)_oxygen terminated	16.5

2.4. Concluding Remarks

An understanding of this unusual electrochemical reaction behavior can offer new design criteria for positive electrode materials in lithium ion batteries. For positive electrode material design, we believe numerous combinations of transition metal compounds and lithium compounds (other than LiF) are possible, and a variety of redox nanocomposite positive electrodes could be developed with tuning of their electrochemical performances. As long as the transition metal compounds contain a valid redox active component, anion participation may activate the lithium storage capability regardless of the crystal structure. Also, as the lithium compounds are readily decomposable in the electrochemical cell, it can supply lithium ions in the lithium ion cells. Moreover, the choice of anions in lithium compounds can be used as an additional rudder to tune the electrochemical properties of the composite electrode.

2.5. References

1. Larcher, D., Tarascon, J. M., Towards greener and more sustainable batteries for electrical energy storage. *Nat. Chem.* **2015**, 7, 19-29.
2. Sathiya, M. *et al.*, Reversible anionic redox chemistry in high-capacity layered-oxide electrodes. *Nat. Mater.* **2013**, 12, 827-835.
3. Lee, J. *et al.*, Unlocking the Potential of Cation-Disordered Oxides for Rechargeable Lithium Batteries. *Science* **2014**, 343, 519-522.
4. Kim, S.-W. *et al.*, Energy storage in composites of a redox couple host and a lithium ion host. *Nano Today* **2012**, 7, 168-173.
5. Tarascon, J. M., Armand, M., Issues and challenges facing rechargeable lithium batteries. *Nature* **2001**, 414, 359-367.
6. Tarascon, J. M., Wang, E., Shokoohi, F. K., McKinnon, W. R., Colson, S., The Spinel Phase of LiMn_2O_4 as a Cathode in Secondary Lithium Cells. *J. Electrochem. Soc.* **1991**, 138, 2859-2864.
7. Padhi, A. K., Nanjundaswamy, K. S., Goodenough, J. B., Phospho-olivines as Positive-Electrode Materials for Rechargeable Lithium Batteries. *J. Electrochem. Soc.* **1997**, 144, 1188-1194.
8. Mizushima, K., Jones, P. C., Wiseman, P. J., Goodenough, J. B., Li_xCoO_2 ($0 < x < 1$): A new cathode material for batteries of high energy density. *Mater. Res. Bull.* **1980**, 15, 783-789.
9. Poizot, P., Laruelle, S., Grugeon, S., Dupont, L., Tarascon, J. M., Nano-sized transition-metal oxides as negative-electrode materials for lithium-ion batteries.

Nature **2000**, 407, 496-499.

10. de Faria, D. L. A., Venâncio Silva, S., de Oliveira, M. T., Raman microspectroscopy of some iron oxides and oxyhydroxides. *J. Raman Spectrosc.* **1997**, 28, 873-878.

11. Fang, X. *et al.*, Electrode reactions of manganese oxides for secondary lithium batteries. *Electrochem. Commun.* **2010**, 12, 1520-1523.

12. Sun, B., Chen, Z., Kim, H.-S., Ahn, H., Wang, G., MnO/C core-shell nanorods as high capacity anode materials for lithium-ion batteries. *J. Power Sources* **2011**, 196, 3346-3349.

13. Gao, M. *et al.*, FeO/C anode materials of high capacity and cycle stability for lithium-ion batteries synthesized by carbothermal reduction. *J. Alloys Compd.* **2013**, 565, 97-103.

14. Dimov, N., Kitajou, A., Hori, H., Kobayashi, E., Okada, S., Electrochemical Splitting of LiF: A New Approach to Lithium-Ion Battery Materials. *ECS Transactions* **2014**, 58, 87-99.

15. Augustyn, V. *et al.*, High-rate electrochemical energy storage through Li⁺ intercalation pseudocapacitance. *Nat. Mater.* **2013**, 12, 518-522.

16. Wang, J., Polleux, J., Lim, J., Dunn, B., Pseudocapacitive Contributions to Electrochemical Energy Storage in TiO₂ (Anatase) Nanoparticles. *J. Phys. Chem. C* **2007**, 111, 14925-14931.

17. Brezesinski, T., Wang, J., Polleux, J., Dunn, B., Tolbert, S. H., Templated Nanocrystal-Based Porous TiO₂ Films for Next-Generation Electrochemical

- Capacitors. *J. Am. Chem. Soc.* **2009**, 131, 1802-1809.
18. Dunn, B., Kamath, H., Tarascon, J.-M., Electrical Energy Storage for the Grid: A Battery of Choices. *Science* **2011**, 334, 928-935.
19. Gilbert, B. *et al.*, Multiple Scattering Calculations of Bonding and X-ray Absorption Spectroscopy of Manganese Oxides. *J. Phys. Chem. A* **2003**, 107, 2839-2847.
20. Qiao, R., Chin, T., Harris, S. J., Yan, S., Yang, W., Spectroscopic fingerprints of valence and spin states in manganese oxides and fluorides. *Curr. Appl. Phys.* **2013**, 13, 544-548.
21. Augustyn, V., Simon, P., Dunn, B., Pseudocapacitive oxide materials for high-rate electrochemical energy storage. *Energy Environ. Sci.* **2014**, 7, 1597-1614.
22. Kim, S.-W. *et al.*, Structure Stabilization by Mixed Anions in Oxyfluoride Cathodes for High-Energy Lithium Batteries. *ACS Nano* **2015**, 9, 10076-10084.
23. Wang, X.-L. *et al.*, Amorphous Hierarchical Porous GeO_x as High-Capacity Anodes for Li Ion Batteries with Very Long Cycling Life. *J. Am. Chem. Soc.* **2011**, 133, 20692-20695.
24. Yamakawa, N., Jiang, M., Key, B., Grey, C. P., Identifying the Local Structures Formed during Lithiation of the Conversion Material, Iron Fluoride, in a Li Ion Battery: A Solid-State NMR, X-ray Diffraction, and Pair Distribution Function Analysis Study. *J. Am. Chem. Soc.* **2009**, 131, 10525-10536.
25. Pereira, N., Badway, F., Wartelsky, M., Gunn, S., Amatucci, G. G., Iron Oxyfluorides as High Capacity Cathode Materials for Lithium Batteries. *J.*

Electrochem. Soc. **2009**, 156, A407-A416.

26. Wiaderek, K. M. *et al.*, Comprehensive Insights into the Structural and Chemical Changes in Mixed-Anion FeOF Electrodes by Using Operando PDF and NMR Spectroscopy. *J. Am. Chem. Soc.* **2013**, 135, 4070-4078.

27. Choi, S., Manthiram, A., Factors Influencing the Layered to Spinel-like Phase Transition in Layered Oxide Cathodes. *J. Electrochem. Soc.* **2002**, 149, A1157-A1163.

28. Kim, H. *et al.*, Multicomponent Effects on the Crystal Structures and Electrochemical Properties of Spinel-Structured M_3O_4 ($M = Fe, Mn, Co$) Anodes in Lithium Rechargeable Batteries. *Chem. Mater.* **2012**, 24, 720-725.

29. Sina, M., Pereira, N., Amatucci, G. G., Cosandey, F., Microstructural Evolution Of Iron Oxyfluoride/Carbon Nanocomposites Upon Electrochemical Cycling. *J. Phys. Chem. C* **2016**, 120, 13375-13383.

30. Oh, M. H. *et al.*, Galvanic Replacement Reactions in Metal Oxide Nanocrystals. *Science* **2013**, 340, 964-968.

31. Vlasse, M., Massies, J. C., Demazeau, G., The refinement of the crystal structure of iron oxyfluoride, FeOF. *J. Solid State Chem.* **1973**, 8, 109-113.

32. Dong, A. *et al.*, A Generalized Ligand-Exchange Strategy Enabling Sequential Surface Functionalization of Colloidal Nanocrystals. *J. Am. Chem. Soc.* **2011**, 133, 998-1006.

33. Kelly, S., Hesterberg, D., Ravel, B., Analysis of soils and minerals using X-ray absorption spectroscopy. *Methods of soil analysis. Part 5*, **2008**, 387-463.

34. Ravel, B., Newville, M., ATHENA, ARTEMIS, HEPHAESTUS: data analysis for X-ray absorption spectroscopy using IFEFFIT. *Journal of synchrotron radiation* **2005**, 12, 537-541.
35. Rehr, J. J., Albers, R., Theoretical approaches to x-ray absorption fine structure. *Reviews of modern physics* **2000**, 72, 621.
36. Lee, S.-Y. *et al.*, Unveiling origin of additional capacity of SnO₂ anode in lithium-ion batteries by realistic ex situ TEM analysis. *Nano Energy* **2016**, 19, 234-245.

Chapter 3. Host formation reaction mechanism: New iron-based intercalation host for lithium-ion batteries

(The essence of this chapter has been published in Chemistry of Materials. Reprinted with permission from [S.-K. Jung *et al.*, *Chem. Mater.* **30** (2018) 1956 DOI: 10.1021/acs.chemmater.7b05017] Copyright (2018) American Chemical Society)

3.1. Research background

The development of novel high-performance cathode materials is pivotal for the further advancement of current lithium-ion batteries to address the ever-growing demands for high-capacity energy storage applications.^{1,2} Extensive efforts have thus been focused on the search for materials with new crystal structures and compositions that would allow a large amount of lithium storage at high redox potential with fast lithium diffusion and electrochemical stability to outperform state-of-the-art cathode materials such as layered, olivine, and spinel lithium transition metal oxides.³ Although identifying a novel cathode material that can rival these materials has been a grand challenge, a new design strategy for cathode materials has been recently proposed that involves making a nanocomposite of lithium compounds (such as LiF) and transition metal compounds (such as MO_x and MF_y where $\text{M}=\text{Mn, Fe, Co}$) blended at the nanoscale.^{4,5} In this approach, the lithium extraction/reinsertion and redox reaction are decoupled and occur separately in the lithium and transition metal compounds, respectively. It was reported that charging of a nanocomposite electrode such as LiF-MO_x induces the dissociation of LiF,

liberating lithium and fluorine ions while the transition metal is concurrently oxidized in the MO_x crystal. The liberated fluorine ions trigger the oxidation of the transition metal by being chemically incorporated in the transition metal compounds.^{4,6} This strategy allows numerous composite materials to function as cathodes; in addition, by taking advantage of the various combinations of lithium compounds and transition metal compounds, new cathode chemistries can be discovered by exploring materials that have previously been disregarded because of their incapability for intercalation.

Although this approach of cathode design is in its infancy and further understanding is needed, two reaction mechanisms have been suggested for nanocomposite cathodes based on their distinct lithium storage behavior, surface conversion reaction, and host formation reaction.⁴⁻¹⁰ The surface conversion reaction accompanies the interaction between the liberated fluorine ion and transition metal mainly on the surface of metal compounds, where the reversible adsorption/desorption of fluorine ions induces the oxidation/reduction of the transition metal (*e.g.*, $\text{LiF} + \text{Mn}^{2+}\text{O} \rightarrow \text{Li}^+ + \text{Mn}^{3+}\text{O-F} + e^-$ for LiF-MnO).⁴ However, the fluorine incorporation on the surface may induce a phase transformation involving the reactive fluorine diffusing into the bulk crystal, forming a new phase. This transformation can occur when a thermodynamically stable phase is present at a certain composition of the transition metal compound with the incorporated fluorine ions. When this phase transformation leads to a new phase with the lithium intercalation capability, it is called a host formation reaction such as for the

electrochemical formation of FeF_3 from the LiF-FeF_2 nanocomposite electrode.⁷

Further understanding of each mechanism and the factors that determine the surface conversion or host formation mechanism would aid in the rational search for optimal combinations of compounds for cathode nanocomposites. The host formation reaction, in particular, may offer a new route to form various intercalation hosts *in situ* during the electrochemical reaction. Our group and Okada *et al.* previously reported that some well-known intercalation hosts such as FeF_3 , LiFeSO_4F , and $\text{Li}_3(\text{VPO}_4)_2\text{F}_3$ can be electrochemically formed during the host formation reaction.^{7,11-13} However, it may also be possible to find a new unexpected intercalation host that has not been obtainable using conventional synthetic routes. Herein, we report the discovery of a new iron-based intercalation host from the host formation reaction using a LiF and FeO nanocomposite. In contrast to our expectations as reported in our previous investigation on LiF and FeO ,⁴ the nanocomposite resulted in the formation of a new crystalline phase, a cubic- FeOF phase, different from the thermodynamically stable and well-known rutile- FeOF . Moreover, unlike the rutile- FeOF that undergoes partial lithiation followed by the conversion reaction, the new FeOF phase exhibited reversible lithium storage without a conversion reaction within the entire region of discharge. The discovery of a new lithium host phase from the nanocomposite implies that the host formation reaction may offer an uncharted strategy to identify novel host crystalline structures for lithium storage.

3.2 Experimental Methods

3.2.1. Synthesis of LiF-FeO nanocomposite

As-received LiF (99.5%; Sigma-Aldrich) and FeO (99%; Sigma-Aldrich) were used without further purification to synthesize the LiF-FeO nanocomposite. The composite material was prepared using planetary ball milling (Pulverisette 5; Fritsch). LiF, FeO, and graphite (20 wt% of the LiF-FeO composite) were inserted into the container (Li/Fe = 2/1, m/m) in an Ar-filled glove box to prevent air exposure. More LiF per FeO (Li:Fe=2:1) was introduced to compensate for the unreacted LiF and to provide sufficient fluorine ions for FeO during the charging process. The precursors were mixed at 400 rpm for 48 h with 5-min rest every 30 min to obtain a finely dispersed composite.

3.2.2. Electrochemical measurements

The electrodes were fabricated with a slurry of 70 wt% of LiF-FeO nanocomposite, 20 wt% carbon black (Super-P; Timcal, Bodio, Switzerland), and 10 wt% polyacrylonitrile (PAN) binder. The powders were dispersed in *N*-methyl-1,2-pyrrolidone (NMP, 99.5%; Sigma-Aldrich), and the slurry was cast onto aluminum foil using a doctor blade. The NMP was evaporated for 4 h at 70 °C in a vacuum oven. Galvanostatic measurements were performed over voltage ranges of 1.5–4.8 V using a potentiogalvanostat (WBCS 3000; WonA Tech, Seoul, Korea) at 60 °C. Coin cells (CR2032; Hohsen, Osaka, Japan) were used to test the electrochemical properties of the LiF-FeO nanocomposite electrode with lithium metal as the counter

electrode, a separator washed with acetone (GF/F Filter; Whatman, Maidstone, Kent, UK), and a 1 M solution of LiPF_6 in a mixture of ethylene carbonate/dimethyl carbonate (1:1, v/v). Cyclic voltammetry experiments were performed after the first charge and after thirtieth charge under the same galvanostatic charge/discharge conditions. The voltage was scanned from 4.8 to 1.5 V with increasing scan rate from 0.1 to 1.0 mV/s. The rate capability of the nanocomposite was tested at current densities of 50, 100, 200, 500 and 1000 mA/g. The rate capability of the electrodes after the host formation reaction was tested after 20 cycles under 50 mA/g. GITT was performed after 20 cycles with 3-h rest time every 10.8 mAh/g (corresponding to $0.05e^-/\text{formula unit}$) at a constant current rate of 50 mA/g.

3.2.3. Characterizations

The as-synthesized LiF–FeO nanocomposite and its phase evolution were characterized using XRD with a D2 PHASER (Bruker, Bremen, Germany) equipped with Cu–K α radiation ($\lambda = 1.54178 \text{ \AA}$) at a scanning speed of $1.0^\circ \text{ min}^{-1}$ in the 2θ range of $20\text{--}70^\circ$. High-resolution powder X-ray diffraction (HRPD) data of nanocomposites were obtained from Beamline 9B at Pohang Accelerator Laboratory (PAL), Republic of Korea. The data were collected over a 2θ range of $30\text{--}100^\circ$ with a step size of 0.01° , step time of 6 s, and wavelength of $\lambda=1.54740 \text{ \AA}$. XAS was performed at the 10C beamline at the Pohang Light Source-II (PLS-II) using a Si(111) double-crystal monochromator. The beam intensity was reduced by 30% to minimize high-order harmonics. The Fe K-edge spectra of the LiF–FeO electrodes were

recorded in transmission mode at room temperature. The storage ring was operated at 2.5 GeV with a ring current of 300–350 mA. Reference spectra of Fe metal were simultaneously collected using Fe foil. The XAS data were analyzed using the Athena program with the energy calibration using the first inflection points in the Fe metal foil spectrum. The EXAFS signal $\chi(k)$ was weighted by k^3 to emphasize the high-energy oscillations and then Fourier-transformed in the k range from 2.0 to 11.5 \AA^{-1} for the Fe K-edge using a Hanning window to obtain the magnitude plots of the EXAFS spectra in R -space (\AA). Near-edge X-ray absorption fine structure (NEXAFS) spectra of the Fe L₃, 2-edge and F K-edge were obtained at the 10D KIST bending magnet beamline at the PLS-II. The measurements were performed at room temperature, and the spectra were collected in the total electron yield (TEY) mode under a base pressure of 1×10^{-9} Torr. The spectra were normalized to the incident photon flux with an energy resolution of 0.1 eV. TEM/STEM measurements were performed using a cold field-emission-type Cs-corrected JEM-ARM200F equipped with an EELS detector (965 GIF Quantum ER) installed at the National Center for Inter-university Research Facilities (NCIRF) at Seoul National University. High-resolution annular-dark-field images were collected with 0.1-nm spatial resolution at 80 kV. For STEM–EELS elemental mapping, the energy dispersion was set as 0.25 eV/ch. The full-width at half-maximum of the zero-loss peak in vacuum was 1.0 eV. The convergence and collection semi-angles were 19 and 52.8 mrad, respectively.

3.2.4. Computational details

Total energy calculations were performed based on density functional theory (DFT) with the Perdew–Burke–Ernzerhof (PBE) generalized gradient approximation (GGA) functional.¹⁴ The projector augmented wave (PAW)^{15,16} method was used as implemented in the Vienna *ab initio* simulation package (VASP).¹⁷ We applied the GGA+U approach to correctly describe localized *d* electrons in Fe ions.¹⁸ A U value of 5.3 eV was used, and it was confirmed that our results were not significantly altered using U values from 3 to 6 eV. The VASP potential set of Fe (PAW_PBE Fe_pv 02Aug2007), O (PAW_PBE O 08Apr2002), and F (PAW_PBE F 08Apr2002) was used. A cutoff energy of 500 eV and an appropriate *k*-point grid based on the Monkhorst–Pack scheme¹⁹ were applied ensuring the total energy converged to less than 1 meV per atom. All the structures were fully relaxed until the residual forces were less than 0.02 eV/Å. For simplicity, the Fe ions were initially assumed to be high-spin ferromagnetic (FM), as in previous DFT studies^{20,21} within spin-polarized calculations. Based on the Fe₂O₃ structure with space group P4₁32, partial removal of Fe atoms and partial substitution of O with F atoms were applied to form a stoichiometric FeOF structure. We generated the structures with various possible Fe site occupancies in tetrahedral sites and calculated the electrostatic energy²² using the python materials genomics (pymatgen)²³ open-source library. Five to nine structures with the lowest electrostatic energies were selected for DFT energy calculations.

3.3. Results and Discussions

3.3.1. Fabrication and electrochemical properties of LiF-FeO

A LiF-FeO nanocomposite was fabricated by mechanically mixing LiF and FeO in an Ar atmosphere following the previously reported processes.⁴ After the mixing procedure, the resulting powder was examined using X-ray diffraction (XRD), and the results are presented in Figure 3.1a. The analysis confirmed that a mixture of LiF and FeO was formed without the production of other secondary phases. Broadening of the diffraction peaks of each phase occurred because of the reduction in the particle sizes after ball milling. The insets of Figure 3.1a show that the LiF and FeO were well mixed, and the typical particle size of FeO was in the range of 20–50 nm. The electrochemical properties of the LiF-FeO nanocomposite as a cathode were evaluated in a lithium half-cell consisting of a lithium metal anode and an electrolyte of 1 M LiPF₆ in a mixture of ethylene carbonate/dimethyl carbonate. Figure 3.1b presents the typical charge/discharge profiles of the LiF-FeO for the first 30 cycles in the voltage range between 1.5 and 4.8 V. It is clear that cathode activity at ~3 V (vs. Li⁺/Li) was achieved with the nano-mixture of LiF and FeO, and the electrode exhibited a reversible capacity of more than 200 mAh/g. The cathode activity of the LiF-FeO nanocomposite was confirmed by X-ray absorption near edge structure (XANES) analysis of the electrode during the electrochemical cycling in Figure 3.1c. The results indicate that the charging accompanies the oxidation of Fe²⁺ to higher oxidation states of Fe with reversible reduction back to

Fe²⁺ during the discharge, which is consistent with previous observations for a LiF–MnO nanocomposite cathode.⁴

Notably, the shape of the electrochemical profile gradually changed with increasing number of cycles, which differs from the findings of a previous report on a LiF–MnO nanocomposite.⁴ The profile tended to develop a plateau-like region, especially near ~3.2 V (vs. Li⁺/Li) with increasing number of cycles. Because of the enlarged plateau-like region, the reversible capacity increased to 272 mAh/g corresponding to 1.26 e⁻/Fe after 30 cycles. Figure 3.1d clearly illustrates that the increase of the reversible capacity was mainly induced by the activation of the redox reaction in the high-voltage region. Although the discharge capacity in the 1.5–2.2 V range remained nearly the same with increasing number of cycles, that corresponding to the higher-voltage range gradually increased from ~ 90 to ~ 150 mAh/g. The enhanced electrochemical activity at 3.2 V was also evident in the dQ/dV analysis, which revealed that both the oxidation and reduction peaks at ~ 3.2 V were noticeably intensified after 30 cycles (red line in Figure 3.1e). Close inspection of the Fe K-edge in the XANES spectra in Figure 3.2 reveals that the increase in the capacity with increasing number of cycles is accompanied by the gradual electrochemical activation of the Fe redox reaction rather than other side reactions such as electrolyte decomposition or polymerization.^{24,25} The variations in the Fe oxidation states with charge and discharge became larger with increasing number of cycles, indicating that the LiF–FeO electrode became more electrochemically active. Moreover, the overall shape of the XANES spectra

continuously changed up to 30 cycles, implying a gradual local structural change around Fe, which will be discussed in detail later.

The voltage profile of the LiF–FeO nanocomposite electrode after cycling is reminiscent of the typical redox reaction of the well-known rutile- $\text{FeO}_x\text{F}_{2-x}$ ($0 < x \leq 1$).^{26,27} In addition, the profile strongly implies that the host formation reaction might have occurred in the LiF–FeO nanocomposite upon cycling, forming the fluorinated phase similar to the rutile- $\text{FeO}_x\text{F}_{2-x}$. However, the electrochemical activity of the new phase induced after cycling displays some critical differences compared with that of the typical rutile- $\text{FeO}_x\text{F}_{2-x}$. In particular, a substantially higher plateau redox potential (~ 3 V vs. Li^+/Li) is observed compared with that of the rutile- $\text{FeO}_x\text{F}_{2-x}$ ($0 < x \leq 1$). Note that the rutile-FeOF electrode generally exhibits an average plateau voltage of 2.65 V (vs. Li^+/Li), which is attributed to the intercalation of lithium into the rutile host.²⁶ In addition, the characteristic redox reaction at 2.4 V (vs. Li^+/Li) of the “FeO–F” phase, as shown in the dQ/dV curve of Figure 3.1e, is not generally observable in rutile- $\text{FeO}_x\text{F}_{2-x}$ ($0 < x \leq 1$) regardless of the fluorine content (x).^{26,27} This finding indicates that the structure of the new FeO–F phase may differ from the typical rutile- $\text{FeO}_x\text{F}_{2-x}$ structure.

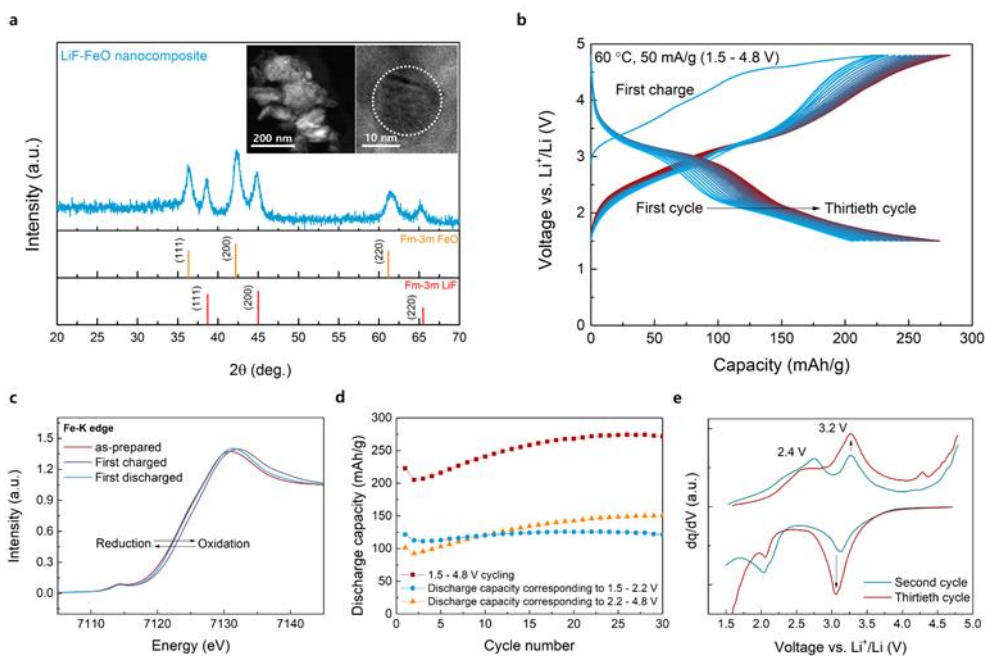


Figure 3.1. Synthesis and electrochemical properties of LiF-FeO nanocomposite. (a) XRD patterns of LiF-FeO nanocomposite. The inset presents a high-resolution TEM (HR-TEM) and scanning transmission electron microscope (STEM) image of the LiF-FeO nanocomposite. (b) Electrochemical profile of the nanocomposite electrode at 60 °C and 50 mA/g current density. (c) XANES analysis of as-prepared first charged and first discharged states. (d) Discharge capacities corresponding to different voltage regions as a function of cycle number. The red square indicates the overall capacity. The yellow triangle and blue circle indicate the capacities in the 2.2–4.8 V and 1.5–2.2 V voltage ranges, respectively. (e) Differential analysis of voltage profile at 2nd and 30th cycles.

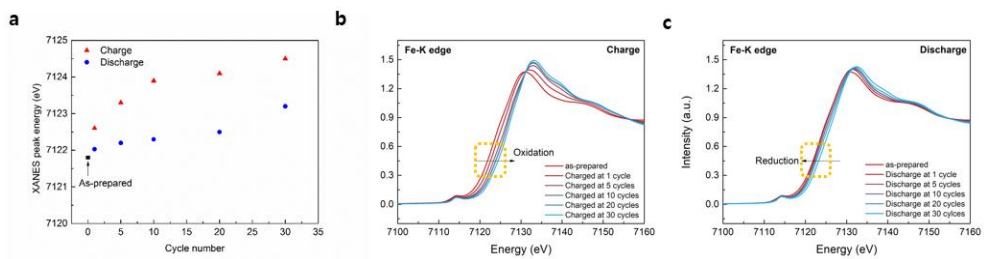


Figure 3.2. (a) XANES peak energy position at normalized intensity of 0.45. XANES analysis of (b) charged and (c) discharged state of LiF-FeO nanocomposite.

3.3.2. New Cubic-FeOF phase evolution

To probe the structural evolution of the LiF–FeO nanocomposite upon cycling, an XRD study was performed on the electrode as a function of cycle number at different states of charge (SOCs) (Figure 3.3). The as-prepared electrode was characterized by the typical diffraction pattern of the rock-salt FeO phase (Fm-3m) with characteristic peaks at 36.4° , 42.5° , and 62.0° ; however, new diffraction peaks gradually appeared at the expense of the original rock-salt peaks after 5 cycles and were clearly observable after 20 cycles, as denoted within the yellow dotted box in Figure 3.3a. These new peaks began to emerge at approximately 36.3° and 43.0° (green arrows) near the peaks corresponding to the FeO phase (red arrows) at the 5th cycle; in addition, another new broad diffraction peak appeared at approximately 30.2° . This phenomenon is also clearly observed from high resolution X-ray diffraction study using synchrotron source in the first charge reaction, which strongly indicates that the phase evolution gradually occurs upon cycling from the first cycle. (Figure 3.4) Notably, none of these new sets of peaks corresponds to the diffraction pattern of the rutile- $\text{FeO}_x\text{F}_{2-x}$ phase, as shown in Figure 3.3b. In contrast, the peak positions of the newly formed FeO–F phase corresponded with the typical Bragg positions of other iron oxide compound references such as the $\text{LiFe}_2\text{O}_3\text{F}$ and FeO_x phases that belong to a cubic crystal system. This finding was rather unexpected as the host formation reaction was believed to be caused by the thermodynamic driving force to form the stable phase at the fluorinated compositions, which would thus result in the most stable rutile- $\text{FeO}_x\text{F}_{2-x}$ phase.

The crystal structure of the new host was more carefully examined using high-angle annular dark-field STEM (HAADF-STEM) analysis, and the results are presented in Figure 3.5. The fast-Fourier transform (FFT) image of the new host structure in the inset of Figure 3.5a clearly shows the periodic pattern of the cubic crystal symmetry of the phase, which is consistent with the XRD results in Figure 3.3b. Based on this image, the diffraction planes could be assigned, as denoted in blue along the [001] zone axis. Even though some signatures of the pristine rock-salt FeO remain, the signal from the (220) plane, which has a *d*-spacing of 0.317 nm cannot be assigned to either FeO or the rutile-FeOF phase and refers to a newly formed FeO–F phase. The cubic FeO–F phase was observed to coexist with the pristine rock-salt FeO phase at the single-particle level, as shown in Figure 3.5b and 3.5c, which correspond to region 1 and 2, respectively, in Figure 3.5a. The coexistence of these two phases could indicate the formation of an intermediate state during the phase transformation, suggesting that a gradual structural evolution occurs from rock-salt to cubic oxyfluoride at the single-particle level. In region 1, an ordered iron atomic arrangement reminiscent of Fe₂O₃-like cubic phase was universally observed. In the high-resolution image of the region, two atomic columns (layer 1 and 2) are well resolved in the [1-10] direction (Figure 3.5d). Each layer was formed by iron atom arrangements with an Fe–Fe spacing of 0.33 nm (layer 1) and 0.17 nm (layer 2) (see the intensity profiles) projected along the [001] zone axis. This iron atomic arrangement is identical to that in typical cubic Fe₂O₃ belonging to the P4₁32 space group. The chemical distribution of Fe, O, and F was also investigated

using electron energy loss spectroscopy (EELS), and the resulting spectra are presented in Figure 3.5e–3.5i. Regardless of the SOCs of the electrodes, the homogenous distribution of Fe and F was detected covering multiple number of particles at relatively low magnification. Moreover, the STEM–EELS analysis of the Fe-L, F-K, and O-K edges of the HR-TEM images in Figure 3.6 confirms the incorporation of F ions throughout the entire particle. This finding contrasts with previous observations for the LiF–MnO system of surface-concentrated interactions between Mn and F ions⁴ and strongly suggests that a substantial amount of F was incorporated to form a new FeO–F structure in the LiF–FeO system.

Further evidence of the new FeO–F host formation was obtained by probing the local structure using EXAFS analysis, as shown in Figure 3.7. Notably, the peak intensity of the first neighbor of the iron rapidly increased with increasing number of cycles; this peak corresponds to the neighboring anion of iron. This finding indicates that the formation of a new ordered structure most likely occurs through the incorporation of fluorine ions; however, it was difficult to distinguish the oxygen and fluorine ions in the EXAFS analysis. The fluorine ion incorporation into the FeO, however, could be verified using soft X-ray absorption spectroscopy (XAS) at the F-K edge (Figure 3.8). The F-K edge spectrum revealed a typical fluorine ion signal for LiF with a small shoulder peak at 700.5 eV in the as-prepared state; however, the peak disappeared after 20 cycles with the advent of the energy level to approximately 684.0 eV, which implies that the fluorine environment changed, including the decomposition of LiF. The pre-edge peak at approximately 684.0 eV is usually

observed for iron fluoride and oxyfluoride compounds with a high Fe valence state and is related to the transition from 1s of fluoride to 2p orbitals, which are hybridized with 3d orbitals of Fe.²⁸⁻³¹ This result provides direct evidence that Fe–F bonds are present in the newly formed Fe₂O₃-like phase.

The combined XAS and XRD results strongly support the view that the incorporation of fluorine ions into FeO triggered the formation of the new FeO–F based structure rather than that of rutile-FeOF. Using first-principles calculations, we verified the feasibility of the formation of the new polymorph of FeOF considering that the newly formed FeO–F has an analogous structure to that of Fe₂O₃ with the P4₁32 space group (Figure 3.9). Partial removal of Fe atoms and substitution of O with F atoms was performed to generate the stoichiometric FeOF structure starting from the P4₁32 Fe₂O₃. The formation energies of the hypothetical P4₁32-type FeOF (cubic-FeOF) with various configurations were compared with the reported formation energy of rutile-FeOF.²¹ The most stable cubic-FeOF phase had a formation energy slightly higher than that of rutile-FeOF by +26.6 meV/atom, indicating its possible presence in a metastable state. Given that the value of $k_B T$ (k_B is Boltzmann's constant) at room temperature is 25.9 meV, we believe that the cubic-FeOF can be formed under electrochemical conditions.

Probing the change of the lattice parameter with charging and discharging also revealed that the new phase is capable of storing lithium in its host structure *via* intercalation. The lattice parameter of the new FeO–F phase was observed to be 8.347 Å, belonging to the P4₁32 space group according to the full-pattern matching.

However, the lattice parameter increased from 8.347 to 8.390 Å after discharging and reversibly decreased back to 8.352 Å after recharging. This reversible change of the lattice parameter indicates that lithium is reversibly de/intercalated into the FeO–F host structure (Figure 3.10). In addition, we observed that the lithiation mechanism of the new phase was clearly distinguished from that of the rutile-FeO_xF_{2-x} phase. Although it is known that the rutile-FeO_xF_{2-x} phase undergoes a conversion reaction involving the Fe metallic phase when more than 0.5 lithium per iron in FeO_xF_{2-x} is inserted, the new phase retained the extended stability of the host structure without the appearance of the Fe metallic phase in the discharge product for as much as 1.25 lithium insertion per iron in FeO–F. The signature of the Fe metal phase, the resultant phase of the typical conversion reaction, is usually detected from rutile-FeO_xF_{2-x} after the discharge in the EXAFS spectrum, which exhibits bonds at 2.2, 3.6, and 4.5 Å; however, no trace of the Fe metal phase was observed for FeO–F after the full discharge.^{32,33} In addition, the generation of Fe metal can be sensitively detected by EXAFS analysis even for small amounts when the conversion reaction is involved.³³ Nevertheless, no signature of the Fe metal phase was observed in the discharged state of the LiF–FeO electrode, as shown in Figure S4b and S4d.

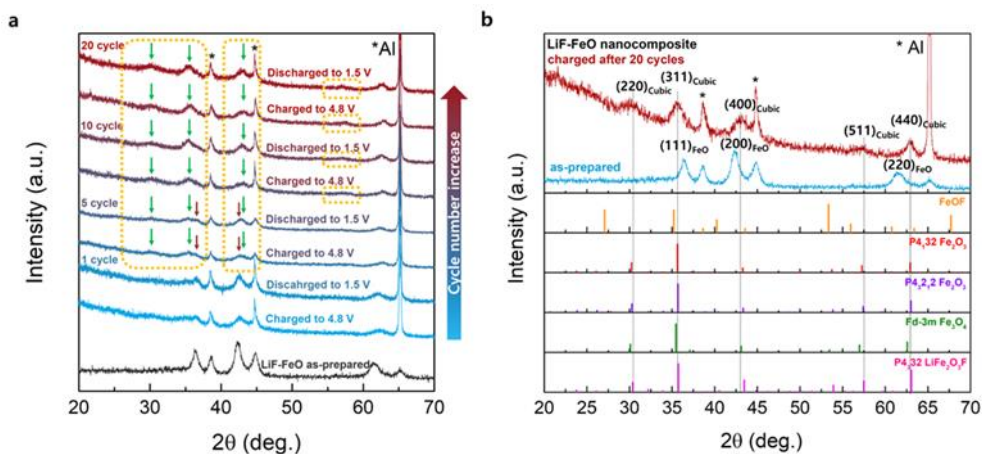


Figure 3.3. Structural evolution of the LiF–FeO nanocomposite during electrochemical cycling. (a) XRD patterns of electrodes at charged/discharged states after different cycle numbers (1, 5, 10, 20 cycles). The green arrows identify the emergence of new peaks, and the red arrows identify the original peak positions of the FeO rock-salt phase. (b) Comparisons of XRD patterns of the electrode in the charged state after 20 cycles with possible reference candidates. The grey dotted lines refer to the peaks of the new phase. The asterisk indicates a peak belonging to the Al foil current collector.

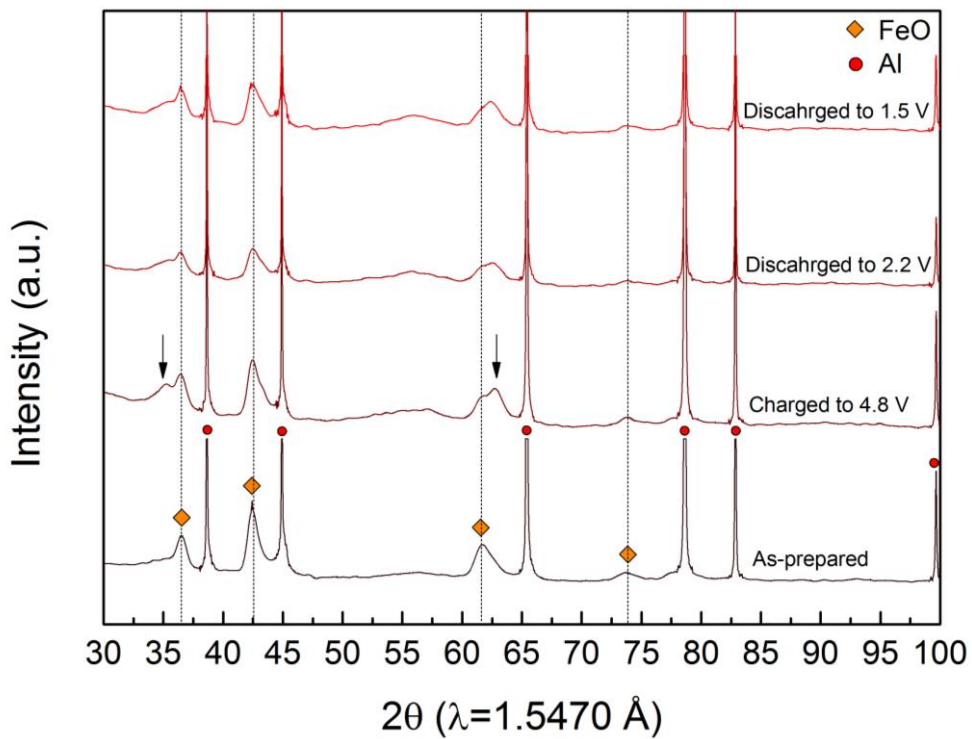


Figure 3.4. High resolution X-ray diffraction of LiF-FeO nanocomposite electrodes during the first cycle. Arrow indicates new diffraction peaks from phase evolution on the first charge.

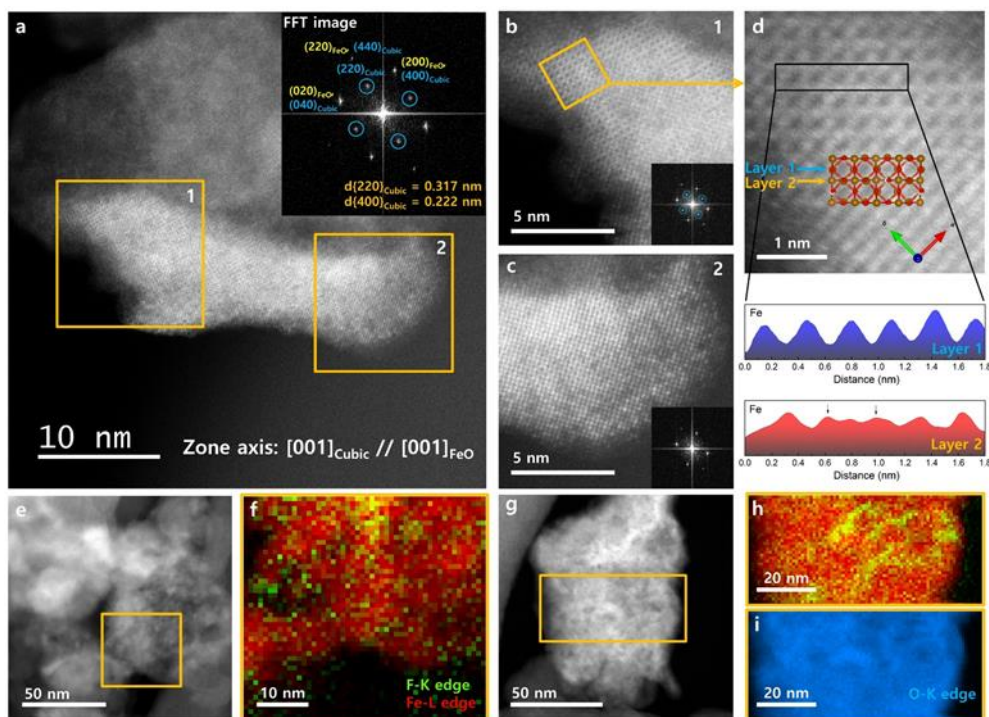


Figure 3.5. Atomic structure and chemical distribution in LiF-FeO nanocomposite after cycling. (a) HAADF image of the electrode after the 20th charging process (inset: fast-Fourier transform images). The blue circle refers to the electron diffraction spot of a new phase. High-resolution images of (b) region 1 and (c) region 2 in (a). (d) Fe atomic arrangements in the new phase showing two different layers. HAADF-STEM images of the electrodes after the 20th (e) charging and (g) discharging process. (f) Corresponding STEM-EELS images of LiF-FeO nanocomposite for yellow box in (e) with the elemental distribution of F (green) and Fe (red). (h, i) STEM-EELS images of LiF-FeO nanocomposite corresponding to the yellow box in (g) with the elemental distribution of F (green), Fe (red), and O (blue).

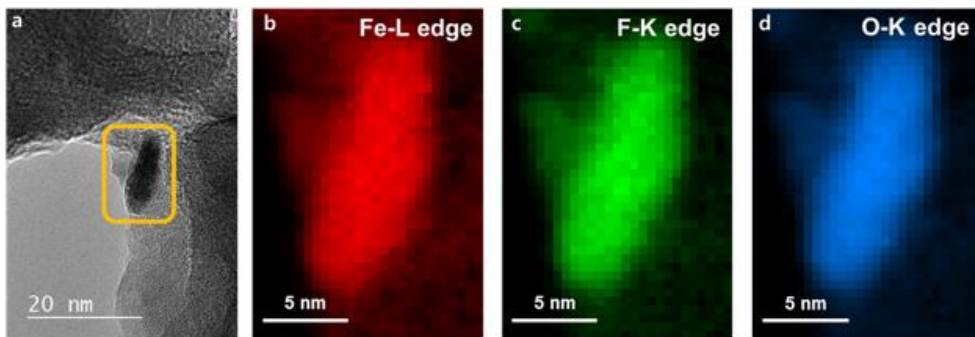


Figure 3.6. (a) HR-TEM image of 20th charged LiF–FeO nanocomposite. (b–d) STEM–EELS images at Fe-L, F-K, and O-K edges.

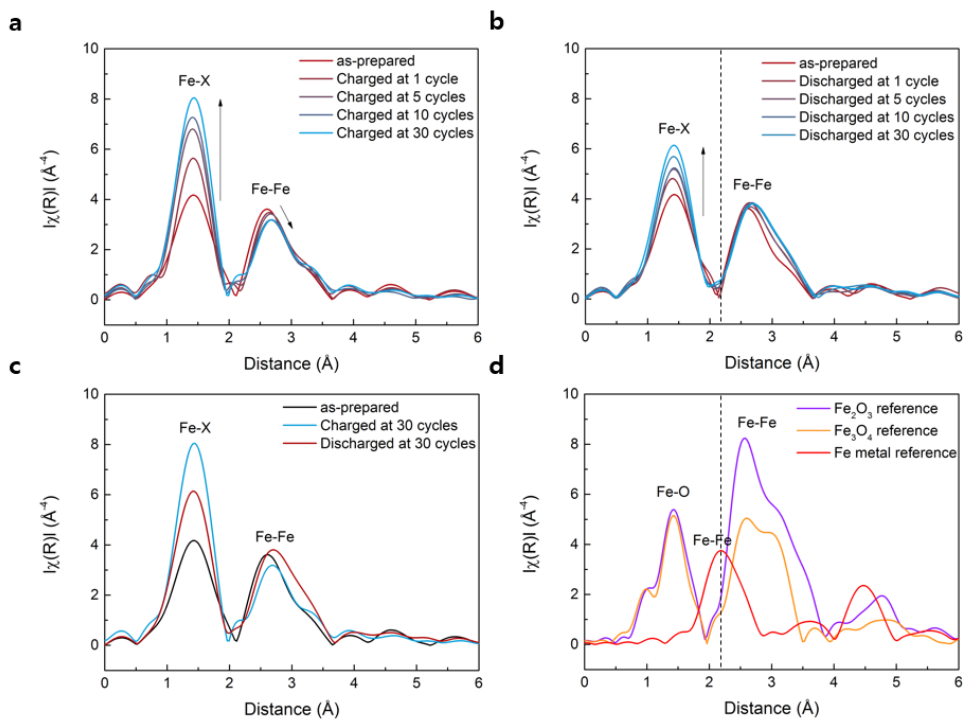


Figure 3.7. EXAFS analysis of (a) charged and (b) discharged states of LiF–FeO nanocomposite. (c) EXAFS spectra of 30th charged/discharged electrodes. (d) EXAFS spectra of Fe_2O_3 , Fe_3O_4 , and Fe metal references.

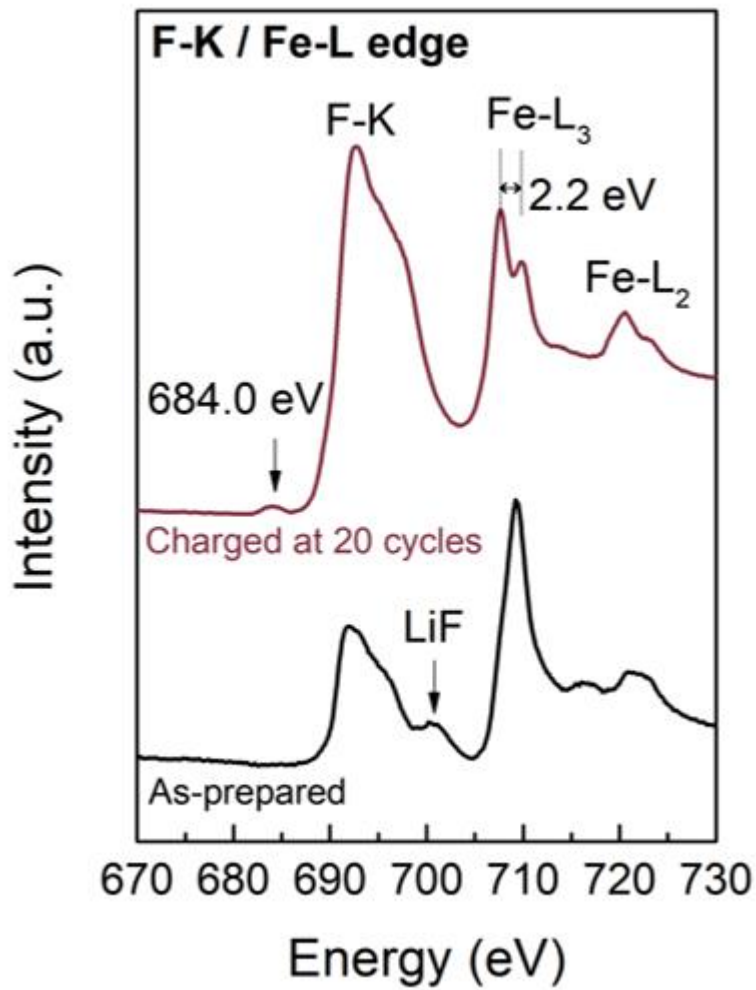


Figure 3.8. Soft XAS analysis of as-prepared and 20th charged state of LiF–FeO nanocomposite in F-K and Fe-L edge range.

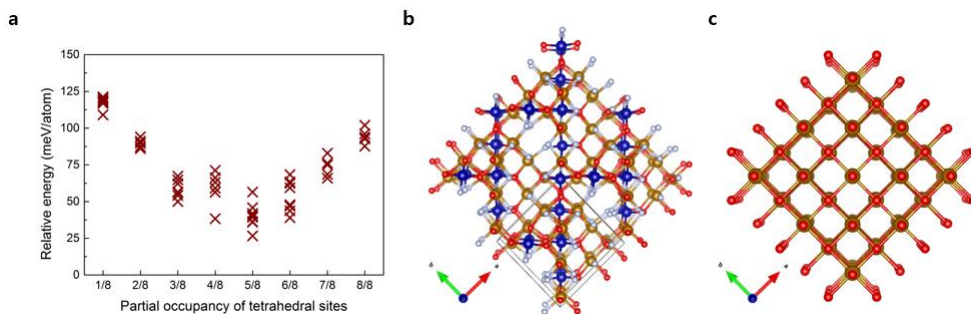


Figure 3.9. (a) Relative formation energy of P4₁32-type FeOF as partial occupancy of iron in tetrahedral site compared with reported rutile-FeOF. (b) Most stable structure of P4₁32-type FeOF (+26.6 meV/f.u. vs. rutile-FeOF) along the c-axis (red: oxygen, white: fluorine, yellow: iron in octahedral site, blue: iron in tetrahedral site). (c) Structure of FeO along the c-axis.

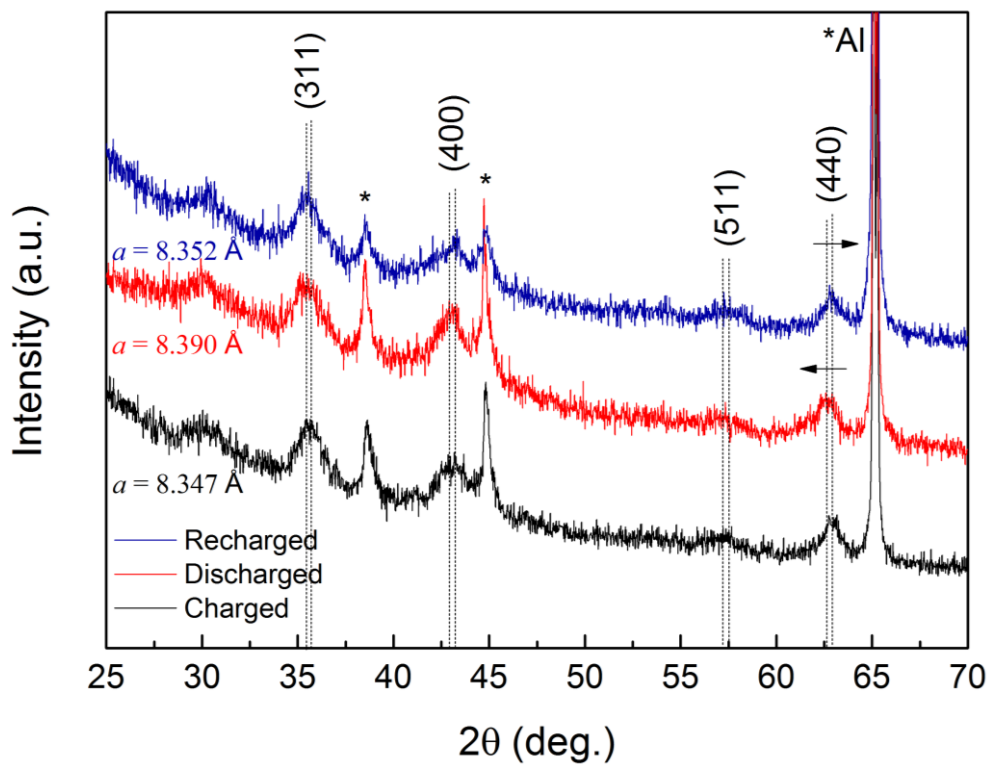


Figure 3.10. XRD patterns of charged and discharged states of FeO-F phase with lattice parameters.

3.3.3. Charge storage behavior in a cubic-FeOF intercalation host

The charge storage behavior of the FeO–F phase based on cyclic voltammetry supports the diffusion-controlled lithium intercalation process into the new host structure (Figure 3.11). We measured the anodic and cathodic peak currents with increasing scan rate from 0.1 to 1.0 mV/s. As observed in Figure 3.11a and 3.11b, the peak current for the 3.2 V redox reaction of the first charged LiF–FeO nanocomposite increased without a voltage shift with increasing scan rate, indicating a surface conversion reaction, as we previously reported.⁴ However, the same experiment after thirtieth charge revealed increases of the anodic and cathodic peak currents with a voltage shift in directions away from each other, which is commonly observed in an intercalation-based electrode with a diffusion-controlled reaction mechanism.³⁴ The distinct electrochemical response clearly illustrates the transformation of the LiF–FeO system into a new intercalation host structure for lithium-ion storage. Quantitative analysis of the portion of the diffusion-controlled intercalation process in the LiF–FeO nanocomposite was performed by deconvoluting the current responses at a fixed potential as a combination of surface capacitive effects (k_1v) and diffusion-controlled insertion effects ($k_2v^{1/2}$).^{35,36} According to the analysis, the contribution of the diffusion-controlled intercalation was 16.7% of the overall discharge capacity during the first charge (Figure 3.11c). In contrast, the contribution of the intercalation process increased significantly from 16.7% to 69.2% after the structural change (Figure 3.11c and 3.11d). It is also noteworthy that this increase was accompanied by the gradual increase of the

capacity during the electrochemical cycling. We further examined the change of the charge-storage behavior by investigating the rate capability before and after the new cubic-FeOF host formation. As shown in Figure 3.12, the rate tests were separately carried out for two sets of the electrodes; the electrodes before the host formation reaction (measuring the first discharge capacities at different current rates) and the electrodes after the host formation reaction (after 20 electrochemical cycles). Due to this reason, the capacities at 50 mA/g current density are different for two cases as shown in Figure 3.12, where the electrode before the host formation reaction delivers a capacity about 180 mAh/g, while 260 mAh/g of capacity is acquired for the electrode after the host formation reaction. This is consistent with the results shown in Figure 3.1b. Regarding the electrodes before the host formation reaction in Figure 3.12a, the increase of the current density from 50 mA/g to 1000 mA/g reduces the capacity only slightly from 180 mAh/g to 150 mAh/g, indicating a good power performance attributable to the faster kinetics of surface-controlled reaction, *i.e.* surface conversion reaction.⁴ The electrodes after the host formation reaction still retain the respectable power capability. Figure 3.12b shows that the capacities of 260, 236, 208, 161 and 125 mAh/g could be delivered at 50, 100, 200, 500 and 1000 mA/g, respectively. We compared the rate capability test upon cycling before and after pre-cycles and the same trend was observed as shown in Figure 3.12c. During the 20 pre-cycles, the capacity increased from 185 mAh/g to 260 mAh/g, however, the rapid decrease of capacity corresponding to 47.8 % of initial capacity was observed as increase of current density from 50 mA/g to 1000 mA/g. Meanwhile, the electrode

without pre-cycles showed high rate performance exhibiting the 80 % of initial capacity at 1000 mA/g current density. Even the capacity value at 1000 mA/g is larger than the cycled electrode (145 mAh/g vs. 125 mAh/g). The capacity was recovered in both electrodes at 50 mA/g current density. Even the electrodes without pre-cycles showed larger capacity (~ 210 mAh/g) than initial cycles (~190 mAh/g) after measuring the rate capability and it is may be due to the gradual host structure formation during the electrochemical cycling. The overall discharge capacities are higher in the case of the electrodes after the host formation reaction due to the presence of the insertion host, cubic-FeOF, however, the rate capability is slightly reduced due to the comparatively sluggish diffusion-controlled reaction which mainly governs the charge storage of cubic-FeOF. This finding implies that the shift of the main charge-storage behavior of the LiF-FeO nanocomposite arising from the formation of the new host structure led to the capacity increase.

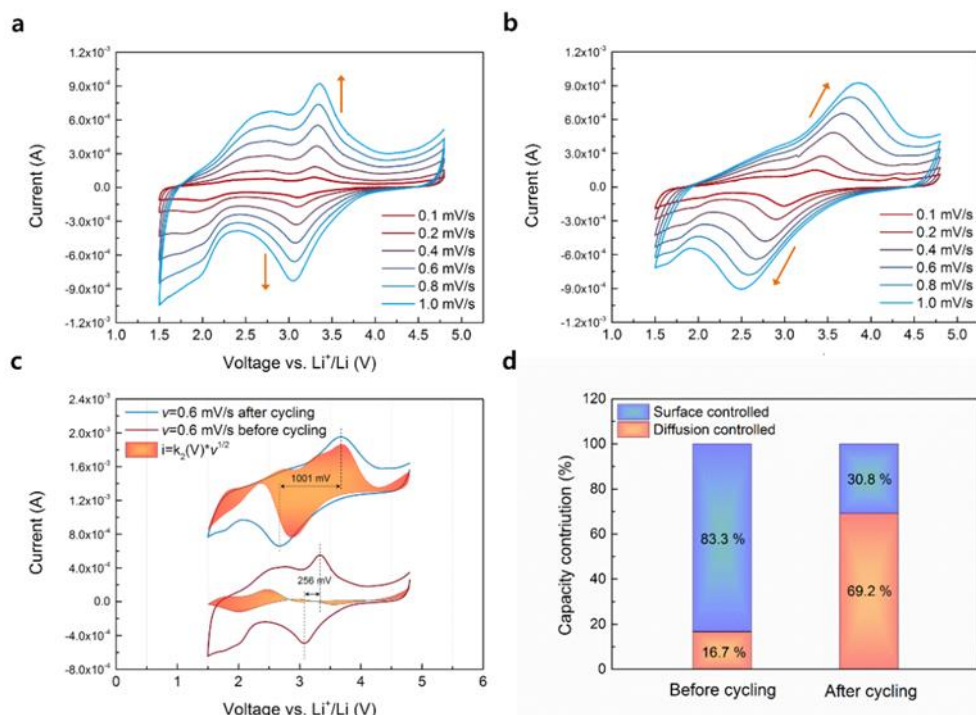


Figure 3.11. Transition from surface-controlled to bulk-diffusion-controlled reaction. (a) Cyclic voltammetry curves at various scan rates from 0.1 to 1.0 mV/s after the first charge and (b) thirtieth charge process. (c) Comparison of current response with voltage at 0.6 mV/s before cycling and after the 30 cycles. The shaded region was obtained from the diffusive current calculated using $i(V) = k_2(V) \cdot v^{1/2}$. (d) Quantitative values of charge storage for LiF-FeO nanocomposite electrodes before cycling and after 30 cycles.

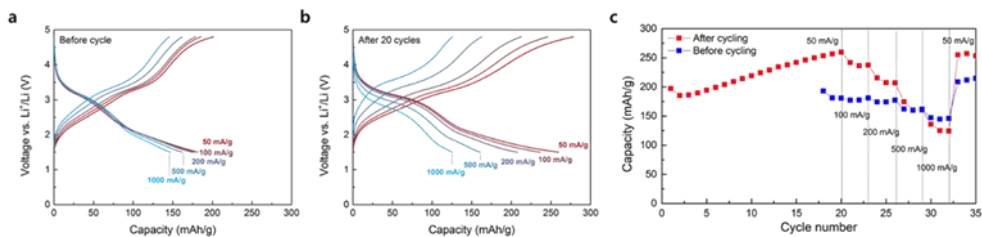
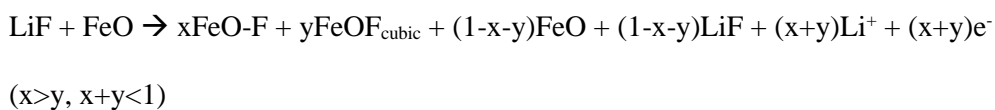


Figure 3.12. Rate performance of LiF-FeO nanocomposite. Charge and discharge profiles of LiF-FeO nanocomposites (a) during the first cycle before the formation of the new host structure and (b) after 20 cycling (after the formation of the new iron host structure). (c) Rate performance at 60 °C upon cycling before and after pre cycles.

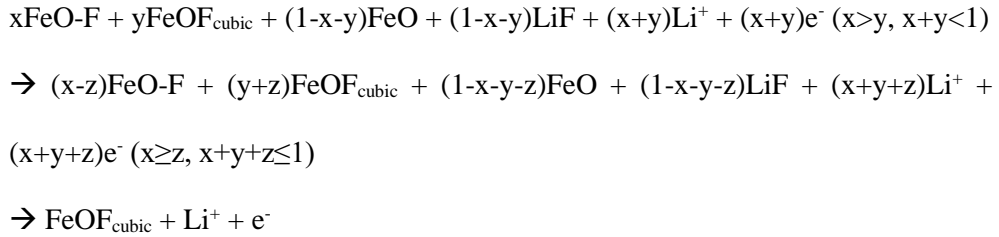
3.3.4. Reaction mechanism

A series of host formation reaction mechanism that occurs during the electrochemical cycling can be described as follows. During the initial few cycles, the fluorine incorporation primarily takes place on the FeO surface forming the metastable FeO-F, which is analogous to surface conversion reaction.⁴ The formation of the cubic-FeOF will simultaneously proceed, even though its contribution to the capacity is smaller than that of the surface conversion reaction based on the FeO-F.

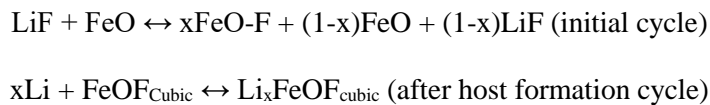


As the electrochemical cycles continue, the portion of the cubic-FeOF formation and its contribution to the capacity substantially increases in comparison to the surface conversion reaction based on the FeO-F. Finally, all the nanocomposite completes the phase transformation to the cubic-FeOF phase, which serves as a new lithium ion insertion host. This host formation accompanies the notable capacity increase due to the enhanced redox activity near 3 V (*vs.* Li⁺/Li). Because of the kinetic limitations involving the diffusion of fluorine ions into the crystal structure and rearrangements of iron, the serial host formation reactions are induced, but the

transition process could be accelerated by the high temperature operation of 60 °C (Figure 3.13).



Therefore, electrochemical reaction may be written depending on the cycle numbers as follows. Lithium storage behavior of LiF–FeO nanocomposite changes from the surface conversion reaction to a bulk diffusion-controlled reaction through the host formation of a new polymorphic cubic-FeOF.



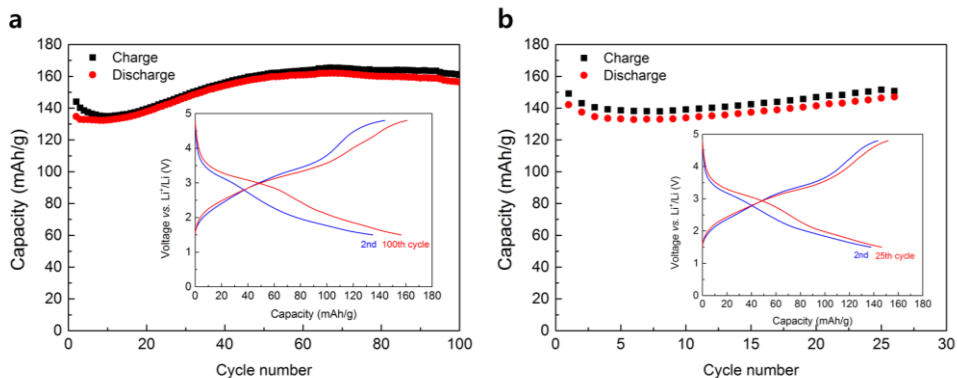


Figure 3.13. (a) Charge and discharge capacity of LiF–FeO nanocomposite as cycles at room temperature. Inset is the charge/discharge voltage profile at 2nd and 100th cycle. (b) Cycle performance at room temperature after the first charge at 60 °C.

3.3.5. Discussion

The new host structure formation from the nanocomposite of LiF and FeO indicates that the host formation reaction is not simply determined by the thermodynamically known stable phase of the specific compositional phase such as rutile-FeOF in this case. Although the thermodynamic driving force may induce the transformation, the metastable states can be trapped in the room-temperature reaction. In addition, the trapped phase may serve as a new host structure for lithium. As demonstrated here, the polymorphic FeOF does not necessarily follow the charge/discharge mechanism of rutile-FeOF. Although a rutile-FeOF electrode yields a mixture of LiF, Li-Fe-O, and FeF_x as intermediate discharge products and FeF_x decomposes into LiF and Fe metal at the end of discharge,²⁷ the discharge product of the cubic-FeOF does not contain Fe metal but rather maintains the host structure. This coherent structural change, accompanied by a slight lattice parameter change, could minimize the compositional non-uniformity that can be induced by the typical conversion reaction, which is one of major origins of the voltage hysteresis in iron oxy/fluoride systems.³⁷ Compared with the discharging reaction of the new cubic-FeOF, a mixture of separated phases such as LiF, Fe, and Li_2O from the rutile- $\text{FeO}_x\text{F}_{2-x}$ is likely to exhibit more severe compositional non-uniformity. This suggests that cubic-FeOF may exhibit a lower voltage hysteresis than rutile- $\text{FeO}_x\text{F}_{2-x}$. Indeed, in our separate experiment, the cubic-FeOF phase exhibited a lower value of the voltage hysteresis based on the galvanostatic intermittent titration

technique (GITT) ($\Delta V = 0.41 \pm 0.15$ V) compared with the reported value of rutile-
 $\text{FeO}_x\text{F}_{2-x}$ ($\Delta V = 0.56\text{--}0.86$ V) at $x = 0.66$ (Figure 3.14).^{27,37,38}

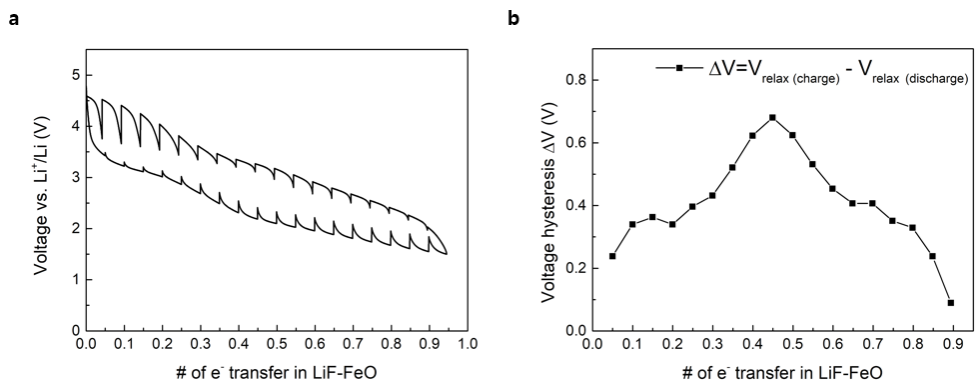


Figure 3.14. (a) GITT curve of LiF-FeO nanocomposite and (b) voltage hysteresis after GITT as a function of lithium content.

3.4 Concluding Remarks

In summary, we reported a new iron-based intercalation host material by exploring the host formation reaction of a LiF–FeO nanocomposite. A new polymorph cubic-FeOF was obtained for the first time, which is distinctive from the well-known rutile-FeOF, through electrochemical cycling. The electrode exhibited cathode activity (~ 3 V vs. Li⁺/Li) with a reversible capacity of more than 200 mAh/g. In addition, the electrochemical cycling induced a capacity increase to 272 mAh/g in the high-voltage region (~ 3.2 V) involving gradual structural evolution into a new host structure. XRD and TEM analyses indicated that the crystal structure of the newly formed phase belonged to a cubic crystal system with atomic arrangements distinguished from those of rutile-FeOF. Furthermore, the electrochemical reaction route of the cubic-FeOF differed from that of the rutile-FeOF that typically exhibits a conversion reaction after partial lithiation, with the extended intercalation-based lithium storage behavior. These findings imply that the host formation reaction provides an unexplored avenue to identify novel intercalation hosts in lithium, sodium and even potassium batteries system^{8,9,39}, while further understanding of the fundamental science behind these findings is required for nanocomposite cathodes.

3.5. References

1. Pearce, P. E. *et al.* Evidence for anionic redox activity in a tridimensional-ordered Li-rich positive electrode β -Li₂IrO₃. *Nat. Mater.* **2017**, 16, 580-586.
2. Seo, D.-H. *et al.* The structural and chemical origin of the oxygen redox activity in layered and cation-disordered Li-excess cathode materials. *Nat. Chem.* **2016**, 8, 692-697.
3. Whittingham, M. S. Lithium batteries and cathode materials. *Chem. Rev.* **2004**, 104, 4271-4302.
4. Jung, S.-K. *et al.* Lithium-free transition metal monoxides for positive electrodes in lithium-ion batteries. *Nat. Energy* **2017**, 2, 16208.
5. Dimov, N.; Kitajou, A.; Hori, H.; Kobayashi, E.; Okada, S. Electrochemical Splitting of LiF: A New Approach to Lithium-Ion Battery Materials. *ECS Trans.* **2014**, 58, 87-99.
6. Zhang, L.; Chen, G.; Berg, E. J.; Tarascon, J.-M. Triggering the In Situ Electrochemical Formation of High Capacity Cathode Material from MnO. *Adv. Energy Mater.* **2017**, 7, 1602200.
7. Kim, S.-W. *et al.* Energy storage in composites of a redox couple host and a lithium ion host. *Nano Today* **2012**, 7, 168-173.
8. Hwang, I. *et al.* NaF-FeF₂ nanocomposite: a new type of Na-ion battery cathode material. *Nano Res.* **2017**, 10(12), 4388-4397.

9. Zhang, L.; Batuk, D.; Chen, G.; Tarascon, J.-M. Electrochemically activated MnO as a cathode material for sodium-ion batteries. *Electrochem. Commun.* **2017**, *77*, 81-84.
10. Kataoka, R.; Kitta, M.; Takeichi, N.; Kiyobayashi, T. Electrochemical In Situ Synthesis: A New Synthesis Route for Redox Active Manganese Oxides for Rechargeable Sodium Ion Battery through Initial Charge Process. *J. Electrochem. Soc.* **2017**, *164*, A226-A230.
11. Kitajou, A.; Kobayashi, E.; Okada, S. Electrochemical Performance of a Novel Cathode material "LiFeOF" for Li-ion Batteries. *Electrochemistry* **2015**, *83*, 885-888.
12. Kitajou, A.; Arai, J.; Okada, S. Cathode Properties of Amorphous XLiFeSO_4 ($x = 1.0, 1.2$ and 1.5) Composite for Li-Ion Batteries. *Meeting Abstracts* **2016**, MA2016-02, 258.
13. Okada, S. *et al.* Possibility of Composite Cathodes with Sacrificial Salts. *Meeting Abstracts* **2016**, MA2016-03, 33.
14. Perdew, J. P.; Burke, K.; Ernzerhof, M. Generalized gradient approximation made simple. *Phys. Rev. Lett.* **1996**, *77*, 3865-3868.
15. Blöchl, P. E. Projector augmented-wave method. *Phys. Rev. B* **1994**, *50*, 17953-17979.
16. Kresse, G.; Joubert, D. From ultrasoft pseudopotentials to the projector augmented-wave method. *Phys. Rev. B* **1999**, *59*, 1758-1775.
17. Kresse, G.; Furthmüller, J. Efficient iterative schemes for ab initio total-energy calculations using a plane-wave basis set. *Phys. Rev. B* **1996**, *54*, 11169-11186.

18. Dudarev, S.; Botton, G.; Savrasov, S.; Humphreys, C.; Sutton, A. Electron-energy-loss spectra and the structural stability of nickel oxide: An LSDA+ U study. *Phys. Rev. B* **1998**, *57*, 1505-1509.
19. Monkhorst, H. J.; Pack, J. D. Special points for Brillouin-zone integrations. *Phys. Rev. B* **1976**, *13*, 5188-5192.
20. Doe, R. E.; Persson, K. A.; Meng, Y. S.; Ceder, G. First-principles investigation of the Li-Fe-F phase diagram and equilibrium and nonequilibrium conversion reactions of iron fluorides with lithium. *Chem. Mater.* **2008**, *20*, 5274-5283.
21. Chevrier, V. L.; Hautier, G.; Ong, S. P.; Doe, R. E.; Ceder, G. First-principles study of iron oxyfluorides and lithiation of FeOF. *Phys. Rev. B* **2013**, *87*, 094118.
22. Ewald, P. P. Die Berechnung optischer und elektrostatischer Gitterpotentiale. *Ann. Phys.* **1921**, *369*, 253-287.
23. Ong, S. P. *et al.* Python Materials Genomics (pymatgen): A robust, open-source python library for materials analysis. *Comput. Mater. Sci.* **2013**, *68*, 314-319.
24. Cabana, J.; Monconduit, L.; Larcher, D.; Palacín, M. R. Beyond Intercalation-Based Li-Ion Batteries: The State of the Art and Challenges of Electrode Materials Reacting Through Conversion Reactions. *Adv. Mater.* **2010**, *22*, E170-E192.
25. Nazri, G.-A.; Pistoia, G. *Lithium batteries: science and technology*; Springer Science & Business Media, **2008**.
26. Pereira, N.; Badway, F.; Wartelsky, M.; Gunn, S.; Amatucci, G. G. Iron Oxyfluorides as High Capacity Cathode Materials for Lithium Batteries. *J. Electrochem. Soc.* **2009**, *156*, A407-A416.

27. Wiaderek, K. M. *et al.* Comprehensive Insights into the Structural and Chemical Changes in Mixed-Anion FeOF Electrodes by Using Operando PDF and NMR Spectroscopy. *J. Am. Chem. Soc.* **2013**, 135, 4070-4078.
28. Vinogradov, A. S. *et al.* Low-lying unoccupied electronic states in 3d transition-metal fluorides probed by NEXAFS at the F 1s threshold. *Phys. Rev. B* **2005**, 71, 045127.
29. Sina, M. *et al.* Structural phase transformation and Fe valence evolution in $\text{FeO}_x\text{F}_{2-x}/\text{C}$ nanocomposite electrodes during lithiation and de-lithiation processes. *J. Mater. Chem. A* **2013**, 1, 11629-11640.
30. Cosandey, F.; Su, D.; Sina, M.; Pereira, N.; Amatucci, G. G. Fe valence determination and Li elemental distribution in lithiated $\text{FeO}_{0.7}\text{F}_{1.3}/\text{C}$ nanocomposite battery materials by electron energy loss spectroscopy (EELS). *Micron* **2012**, 43, 22-29.
31. Nakai, S. *et al.* Core-exciton absorption in the F K absorption spectra of 3d transition-metal fluorides. *Phys. Rev. B* **1988**, 37, 10895-10897.
32. Nam, K.-W.; Wang, X.-J.; Pereira, N.; Amatucci, G.; Yang, X.-Q. In Situ X-ray Absorption Spectroscopy (XAS) Study of Nanocomposite C- FeF_2 , C-FeOF and C- FeF_3 Conversion Materials during Charge-Discharge Cycling. *Meeting Abstracts* **2010**, MA2010-02, 1013.
33. Zhang, W. *et al.* In Situ Electrochemical XAFS Studies on an Iron Fluoride High-Capacity Cathode Material for Rechargeable Lithium Batteries. *J. Phys. Chem. C* **2013**, 117, 11498-11505.

34. Yu, D. Y. W. *et al.* Study of LiFePO₄ by Cyclic Voltammetry. *J. Electrochem. Soc.* **2007**, 154, A253-A257.
35. Wang, J.; Polleux, J.; Lim, J.; Dunn, B. Pseudocapacitive Contributions to Electrochemical Energy Storage in TiO₂ (Anatase) Nanoparticles. *J. Phys. Chem. C* **2007**, 111, 14925-14931.
36. Augustyn, V. *et al.* High-rate electrochemical energy storage through Li⁺ intercalation pseudocapacitance. *Nat. Mater.* **2013**, 12, 518-522.
37. Li, L. *et al.* Origins of Large Voltage Hysteresis in High-Energy-Density Metal Fluoride Lithium-Ion Battery Conversion Electrodes. *J. Am. Chem. Soc.* **2016**, 138, 2838-2848.
38. Ko, J. K. *et al.* Transport, Phase Reactions, and Hysteresis of Iron Fluoride and Oxyfluoride Conversion Electrode Materials for Lithium Batteries. *ACS Appl. Mater. Interfaces* **2014**, 6, 10858-10869.
39. Li, Y. *et al.* Recent advances of electrode materials for low-cost sodium-ion batteries towards practical application for grid energy storage. *Energy Storage Mater.* **2017**, 7, 130-151.

Chapter 4. Chemical origins of the activity in nano-mixture cathode materials

4.1. Research Background

Craving for new cathode materials is incessantly maintained as a hope for seeking the solution of utmost challenges in current lithium ion battery (LIB) technologies. Until so far, we have had a narrow field of view limited to the intercalation compounds such as layered type LiCoO_2^1 or $\text{Li}(\text{Ni},\text{Mn},\text{Co})\text{O}_2^2$ or LiFePO_4^3 with olivine structure. Recently, a nano-scale mixture with alkali metal compounds and transition metal compounds was reported as a new design concept of cathode materials. This could provide new opportunities for excavating cathode materials thanks to the numerous combinations between lithium compounds and transition metal compounds. This new strategy enables us to extend the scope of searching the cathode materials to such as FeF_2 , MnO_x ($1 < x < 2$), FeO , CoO , and NiO which were traditionally disregarded as cathode material due to the absence of intrinsic lithium and low voltage^{4, 5, 6, 7, 8, 9, 10}. Even this design strategy is generally applied to Na ion battery beyond Li system^{11, 12, 13}.

These nanocomposite electrodes unexceptionally accompany the activation process in the first charge to function as cathode materials with high voltage and capacity^{4, 7}. Decomposition of LiF , which is usually used as lithium compound,

occurs by the lithium extraction during the first charge with the oxidation of transition metal ion simultaneously. Liberated fluorine ion from LiF incorporated into transition metal compounds to balance the charge neutrality. The activation process can be classified into two groups as the reaction mechanism, which is determined by the fluorine ion incorporation behavior. One is the host formation reaction, and the other is surface conversion reaction^{7,14}. In the case of host formation reaction, a new host structure for lithium intercalation is formed after the first charge reaction (*e.g.* $\text{LiF} + \text{FeO} \rightarrow \text{Li}^+ + \text{FeOF} + e^-$). Meanwhile, in surface conversion reaction, fluorine ion incorporation accompanying the oxidation of transition metal ion and structural evolution happens only at the surface of transition metal compounds particles (*e.g.* $\text{LiF} + \text{MnO} \rightarrow \text{Li}^+ + \text{MnO-F} + e^-$).

The activation process of nanocomposite electrodes during the first charge accompanies different voltage profile with high potential compared to the profiles of subsequent electrochemical cycles. High cut-off voltage charging up to 4.8 V is required to induce fully oxidized state of metal compounds by liberating the fluorine ion as much as possible from LiF for large capacity and high voltage. These electrochemical features of the first charging reaction are shown regardless of reaction mechanisms as fluorine incorporation behavior (surface conversion or host formation reaction). However, the understanding on the first charge activation process is still unclear and even the origin of the electrochemical activity is unknown in nano-mixture cathode materials.

Here, we study on the chemical origin of activity and the first charging

activation process of the nanocomposite with the MnO as a model system by systematical change of fluorine source from LiF to MF_x ($\text{MF}_x = \text{NaF}$, KF , RbF , CsF , MgF_2 , CaF_2 and AlF_3). We found that binding energy of electron belong to fluorine ion in metal fluoride has strong correlation with the overpotential of the first charge profile, and even the activity of nanocomposite. As a result, tuning the binding energy of F 1s electrons improves the activity of the nanocomposite by reducing the overpotential of the first charge. In addition, the stability of cation in electrolyte as salts affects the overpotential. The feasibility of various metal fluorides as fluorine donor can open an opportunity to expand the nanocomposite electrode design concept to other batteries system. Fundamental understanding on the first charge reaction can provide the intuition for designing the alkali metal compounds for nanocomposite electrodes

4.2. Experimental Methods

4.2.1. Synthesis of MF_x-MnO nanocomposites

To synthesize the MF_x-MnO (M= Li, Na, K, Rb, Cs, Mg, Ca, Al; x = 1~3) nanocomposites, as received LiF (Acros-Organics), NaF (Acros-Organics), KF (Sigma-Aldrich), RbF (Alfa Aesar), CsF (Alfa Aesar), MgF₂ (Sigma-Aldrich), CaF₂ (Alfa Aesar), AlF₃ (Alfa Aesar), and MnO (Sigma-Aldrich) were used without any further treatment. Each nanocomposite was prepared by planetary ball milling (Pulverisette 5; Fritsch). Stoichiometric amount of MF_x, MnO (F/Mn = 1/1, m/m) and additional 20 wt% of graphite (Bay carbon Inc.) were inserted into the container, and sealed in an argon-filled glove box to minimize air exposure. The powders in the containers were mixed at 400 RPM for 48 hours with 5 minutes rest every 30 minutes using 20 silicon nitride balls (10 mm) to obtain nano-sized composites. LiCsF₂ was mechanochemically synthesized by planetary ball milling of LiF and CsF (1:1, m/m). The procedure to synthesize LiCsF₂-MnO nanocomposite was the same as that described above (F/Mn = 1/1, m/m).

4.2.2. Electrochemical measurement

Electrodes were fabricated with the following procedure. A 70 wt% MF_x-MnO nanocomposites, 20 wt% conducting carbon (super-P; Timcal, Bodio, Switzerland), and 10 wt% polyacrylonitrile (PAN) binder were mixed in *N*-methyl-1,2-pyrrolidone (NMP, 99.5%; Sigma-Aldrich) to make slurry. The slurry was casted onto aluminium foils using a doctor blade in an argon-filled glove box. The NMP

was evaporated overnight at 60 °C in an argon-filled glove box. The dried electrode was punched with 1/2 inch punching tool. Coin cells (CR2032; Hohsen) were assembled in an argon-filled glove box with the MF_x-MnO nanocomposite electrode, lithium metal counter electrode, a separator washed with acetone (GF/F Filter; Whatman), and an electrolyte of 1 M LiPF₆ in ethyl carbonate/dimethyl carbonate (EC/DMC, 1:1, v/v). To see the effect of fluorine source in electrolyte, a fluorine free electrolyte of 1 M LiClO₄ in EC/DMC (1:1, v/v) was also used. In order to have statistically valid results, galvanostatic charge/discharge profiles were measured 5 times for each MF_x-MnO nanocomposite electrodes and salt in a voltage range of 1.5–4.4 V vs. Li⁺/Li and a current density of 50 mA g⁻¹ with a potentiogalvanostat (WBCS 3000; WonA Tech, Seoul, Korea) at 60 °C. In galvanostatic intermittent titration technique (GITT) measurements, each of eight MF_x-MnO electrode was charge with C/5 rates (C/N rate means fully charge to theoretical capacity in N hours). The theoretical capacity was calculated based on the amount of one F per MnO reacted. Each nanocomposite was charged with C/5 rate with 30 min and rested for 6h.

To investigate the effect of M-F binding energy on electrochemical property, galvanostatic measurement of LiCsF₂-MnO nanocomposite was performed with a 1 M LiPF₆ in EC/DMC (1:1, v/v) in voltage ranges of 1.5–4.2 V, 1.5–4.3 V, 1.5–4.4 V, 1.5–4.5 V, 1.5–4.6 V, 1.5–4.7 V, and 1.5–4.8 V. The same measurement using different cut-off voltage was also performed with LiF-MnO nanocomposite to compare.

4.2.3. Characterization

4.2.3.1. X-ray diffraction

Prepared MF_x-MnO nanocomposites and LiCsF₂ powder were characterized by XRD using a D2 PHASER (Bruker) equipped with Cu K α radiation ($\lambda = 1.54178 \text{ \AA}$) at a scanning speed of $1.0^\circ \text{ min}^{-1}$ and a 2θ range of 20° – 80° with step size of 0.01° . The Williamson-Hall plot analysis was performed to analyze the average crystalline size of eight MF_x-MnO nanocomposites. The Williamson-Hall plot was done with FullProf_Suite program and the equipment factor (U, V and W) was calibrated with LaB₆ powder to get precise data.

4.2.3.2. X-ray photoelectron spectroscopy (XPS)

The chemical states and composition of the MF_x-MnO, and LiCsF₂-MnO nanocomposites were identified by XPS (Thermo VG Scientific). The spectra were calibrated with the carbon 1s peak position.

4.2.3.3. Computational details

Density functional theory calculations were performed to obtain the enthalpy of interaction H_{int} between cations (Li⁺, Na⁺, Ca⁺) and salt anions (PF₆⁻, ClO₄⁻), where H_{int} was defined as follows:

$$H_{int} = H_{MX} - H_M - H_X$$

Here, H_{MX} , H_M and H_X is the enthalpy of cation-anion complex, isolated cation

and isolated anion, respectively. For all geometric optimization, we used Gaussian 09 code¹⁵ with B3LYP/6-311G (3df) level of exchange-correlation functionals and basis sets^{16, 17}. In order to describe the electrolyte environment, polarizable continuum model¹⁸ as implemented in Gaussian 09 code was included in all calculations using a dielectric constant of EC/DMC solvent.

4.3. Results and Discussions

4.3.1. Electrochemical activities of MF_x-MnO as metal fluorides

The MF_x-MnO (MF_x=LiF, NaF, KF, RbF, CsF, MgF₂, CaF₂ and AlF₃) nanocomposites were synthesized by high energy ball milling, following the previous reports, and the F to Mn ratio is fixed to 1 to 1 in this report (Figure 4.1). All the nanocomposites were successfully synthesized maintaining each characteristic peaks of metal fluorides and MnO as shown in X-ray diffraction patterns (XRD) (Figure 4.1a) without unintended chemical reaction which can induce phase evolution except metal fluorides and MnO. Meanwhile XRD peaks of MnO in each nanocomposite showed different peak intensity and broadness which indicates different particle size and crystallinity. Different hardness or physical properties of each metal fluoride may affect the particle size or crystallinity of MnO during mechanochemical mixing process. The difference in XRD peak broadness and intensity was further analyzed with Williamson-Hall plot analysis (Figure 4.2 a). The Williamson-Hall plot results show that the particle size of MnO in each MF_x-MnO is different in range from 10 nm for LiF-MnO and NaF-MnO to 80 nm for 1/3AlF₃-MnO (Figure 4.2b). We classified the nanocomposites into two groups (group A and group B) by average particle size which was obtained from Williamson-Hall plot to compare and analyze the electrochemical activity of each nanocomposite because the MnO based nanocomposite follows the “surface conversion” reaction mechanism that the capacity is affected by the particle size of MnO⁷. The group A composed of MnO with nearly 20 nm of average particle size includes M= Li, Na,

K, Mg, and Ca, and the others (Rb, Cs, and Al) belong to group B which has larger particle size than 45 nm (Figure 4.2b). The following experimental results will be compared within group A and B, respectively, categorized here.

First, we measured the electrochemical properties of nanocomposites to confirm the feasibility of various metal fluorides as fluorine donor with the same voltage range of 1.5 – 4.4 V vs. Li⁺/Li in a lithium half-cell configuration and all the cell test results shown here were tested at 60 °C. Please note that all the nanocomposite electrodes were evaluated in lithium hybrid cell except the Li case and we estimate the amount of fluorine ion incorporated into MnO through dividing specific discharge capacity by theoretical capacity in order to fairly compare among MF_x-MnO nanocomposites. As shown in Figure 4.1b and 4.1c charge/discharge profile of the nanocomposites after the first charge is analogous to the typical profile of LiF-MnO nanocomposite, which indicates that lithium ions mainly involved in discharge reaction regardless of cation species in starting compounds. Additionally, we found that not only monovalent alkali metal fluorides beyond LiF but also multivalent ion fluorides can act as fluorine ion donor in nanocomposite electrode, which imply the feasibility of nanocomposite electrode design strategy for extended application to other battery systems such as Mg, Ca, and Al. In the case of Na, K, Rb, and Cs, over 0.5e⁻ participated in discharge reaction with clear redox reaction in 3.75 V and 2.5 V. It is consistent to the previous report that Mn^{3+/4+} redox reaction mainly occurs at 3.75 V while Mn^{2+/3+} manifested at 2.5 V. However, the others showed smaller capacity with reduced 3.75 V redox reaction. The capacity of LiF-MnO usually reaches to 0.9 e⁻

corresponding to ~ 240 mAh/g ($0.9 e^-/\text{Mn}$) within the 4.8 V, however, it showed decreased value of $0.5 e^-$ at 4.4 V cut-off voltage condition and the capacity loss is attributed to decreased activity at 3.75 V redox reaction. Also, $\text{MF}_x\text{-MnO}$ with high reversible capacity (Na, K, Rb and Cs) shows higher capacity above 2.7 V than that of $\text{MF}_x\text{-MnO}$ with low reversible capacity (Li, Mn, Ca and Al) (Figure 4.3). Figure 4.1d shows the correlation between the first charge capacity and reversible discharge capacity of each nanocomposite. It is obvious that the discharge capacity increased as first charge capacity increases. Note that the first charge capacity is induced by the decomposition of metal fluoride and simultaneous oxidation of manganese ion. It implies that decomposition properties of metal fluorides can be another factor that determines the capacity together with particle size of transition metal compound.

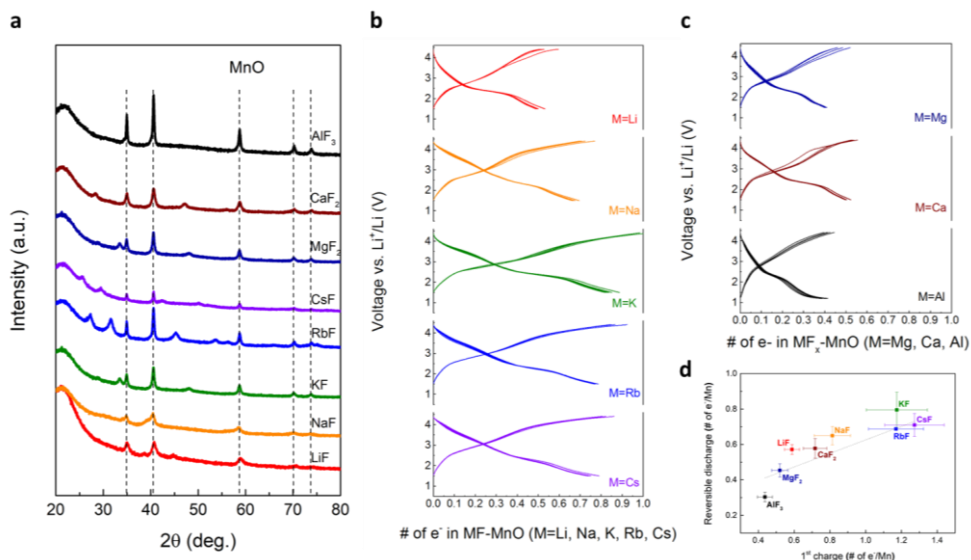


Figure 4.1. Synthesis and electrochemical activities of $\text{MF}_x\text{-MnO}$ nanocomposites. (a) X-ray diffraction patterns of $\text{MF}_x\text{-MnO}$ (M=Li, Na, K, Rb, Cs, Mg, Ca, Al) nanocomposites. (b) Electrochemical profiles of $\text{MF}_x\text{-MnO}$ (M=Li, Na, K, Rb, Cs) (c) (M=Mg, Ca, Al) nanocomposites after the first charge to 4.4 V vs. Li^+/Li in 1 M LiPF_6 in EC/DMC (1:1, v/v) electrolyte. (d) Relation between the number of electrons transferred in the first charge and reversible discharge capacity of $\text{MF}_x\text{-MnO}$ nanocomposites.

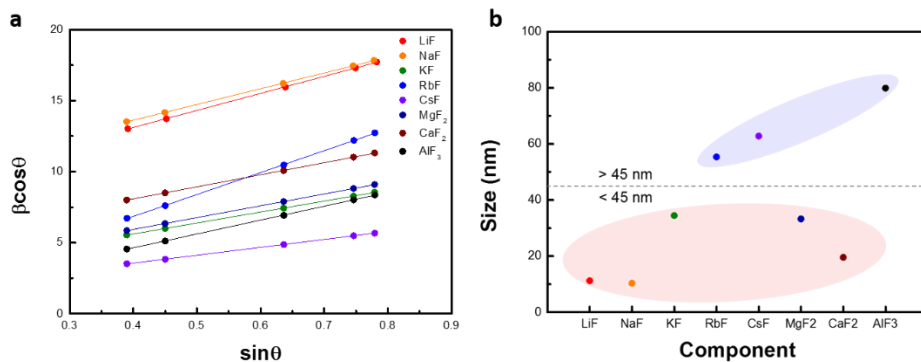


Figure 4.2. (a) Williamson-Hall plot of MnO XRD peaks measured from $\text{MF}_x\text{-MnO}$ nanocomposite ($M=\text{Li, Na, K, Rb, Cs, Mg, Ca, Al}$). (b) Calculated mean size of MnO in each nanocomposite. Nanocomposites are classified into two groups according to MnO size in order to ignore the MnO size effect on electrochemical activity of nanocomposite.

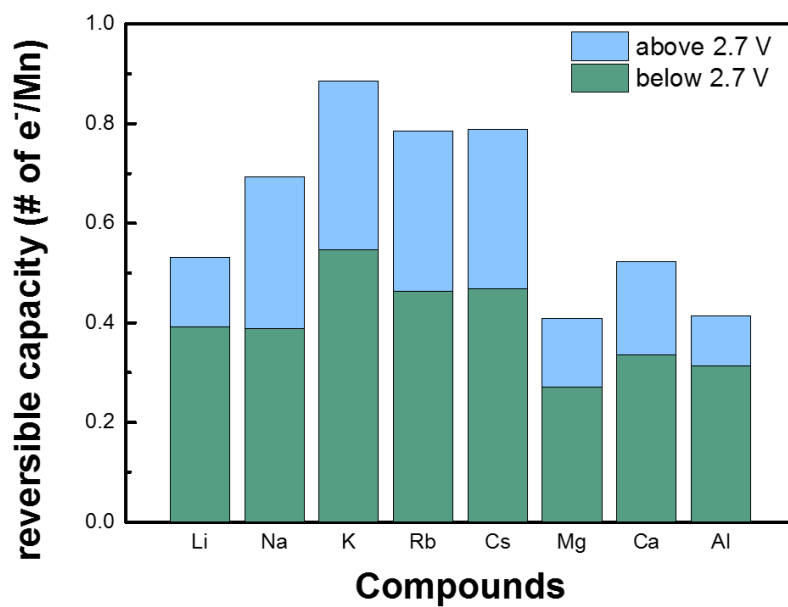


Figure 4.3. The reversible capacity of eight MF_x-MnO nanocomposite electrode. The blue bar represent the capacity expressed above the 2.7 V and the green bar represent the capacity expressed below the 2.7 V.

4.3.2. Overpotential of the first charge determining the activity

To find clues to different discharge capacity of the each $\text{MF}_x\text{-MnO}$ compound, we closely looked at the beginning of their first charge profile. We analyzed and compared the first charge profile of eight $\text{MF}_x\text{-MnO}$ nanocomposite as group of A and B, because the discharge capacity of $\text{MF}_x\text{-MnO}$ is critically affected by the size of MnO which following ‘surface conversion’ reaction mechanism. The different first charge profiles of $\text{MF}_x\text{-MnO}$ nanocomposites are shown in Figure 4.4a for group A compounds and 4.4b for group B compounds. It is clear that the initial voltage liberating fluorine ion is affected by the species of MF_x compounds. In group A, the initial first charging voltage forming 0.1F-MnO increases in the order of $\text{K}<\text{Na}<\text{Li}<\text{Ca}<\text{Mg}$ (Figure 4.4a). Meanwhile, reversible capacity shows the maximum at potassium and decreases in the order of $\text{K}>\text{Na}>\text{Li}>\text{Ca}>\text{Mg}$ (inset of Figure 4.4a). The same trend was also found in group B compounds. The initial first charge potential of group B compounds increases in the order of $\text{Cs}<\text{Rb}<\text{Al}$. The reversible capacity showed the opposite trend to the charging potential (inset of Figures 4.4b). These results show that the charging potential critically affect and determine the reversible capacity of $\text{MF}_x\text{-MnO}$ nanocomposite.

We performed the galvanostatic intermittent titration technique (GITT) to analyze the origin of the different charging potential of $\text{MF}_x\text{-MnO}$ nanocomposite (Figure 4.4c). On all $\text{MF}_x\text{-MnO}$ electrodes, the cells were rested for 6 hours after every $0.1\text{ e}^-/\text{Mn}$ charging with C/5 rate (Figure 4.5). We observed the overpotential

and relaxed voltage at 0.1F-MnO of GITT that metal fluorides began to be decomposed (Figure 4.4c). The reaction overpotential from ohmic (IR) drop is negligible and the overpotential value has variation as nanocomposites within the range from 200 mV to 1200 mV. The relaxed voltage was nearly same as 3.08 V with small variation (90 mV) regardless of metal fluorides, which means that thermodynamic equilibrium potential is mainly determined by the number of fluorine ion incorporated into MnO. These results show that the overpotential induced by kinetic hindrance of decomposition affects the first charge potential of $\text{MF}_x\text{-MnO}$ nanocomposite. Therefore, the overpotential negatively affects the discharge capacity of nanocomposite as shown in Figure 4.4d.

The origin of overpotential could be induced by low electronic conductivity of metal fluorides because fluorides compounds are well known as insulator due to the large bandgap energy induced by high electronegativity of fluorine atom. As shown in table 1, we compared band gap energy of each metal fluoride calculated by density functional theory (DFT) calculation. All the metal fluorides showed insulator characteristic with large band gap energy ($5 \sim 9 \text{ eV}$)¹⁹, however, the correlation between the band gap energy and overpotential is ambiguous. In addition, the effect of electronic conductivity of MF_x on overpotential may be insignificant given the fact that oxidation and reduction occur not on the metal fluoride but on the MnO even though the low electronic conductivity of metal fluorides in electrode can increase the cell resistivity.

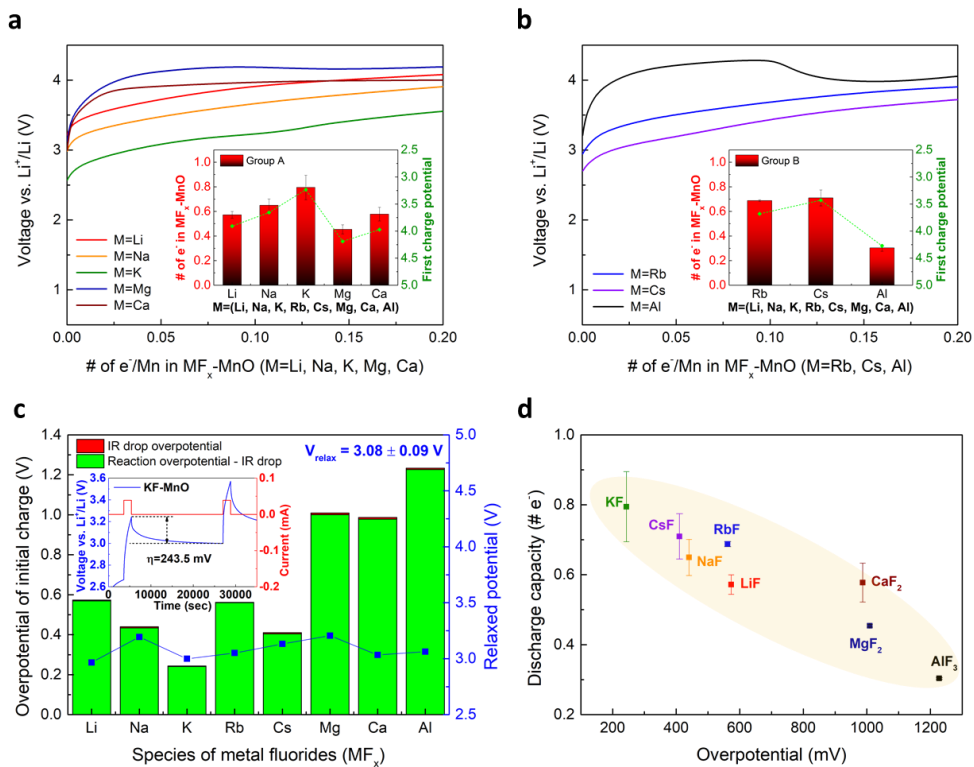


Figure 4.4. Origins of the first charge activation in $\text{MF}_x\text{-MnO}$ nanocomposites.

(a) Initial profile of the first charge of $\text{MF}_x\text{-MnO}$ nanocomposites ($M=\text{Li, Na, K, Mg, Ca}$; Group A) (b) ($M=\text{Rb, Cs, Al}$; Group B). Inset figures are the correlation of reversible capacity and first charge potential at 0.1F-MnO. (c) Overpotential and relaxed voltage at 0.1F-MnO. Inset figure is GITT of KF-MnO. (d) Overpotential at 0.1F-MnO vs. electrochemical activities.

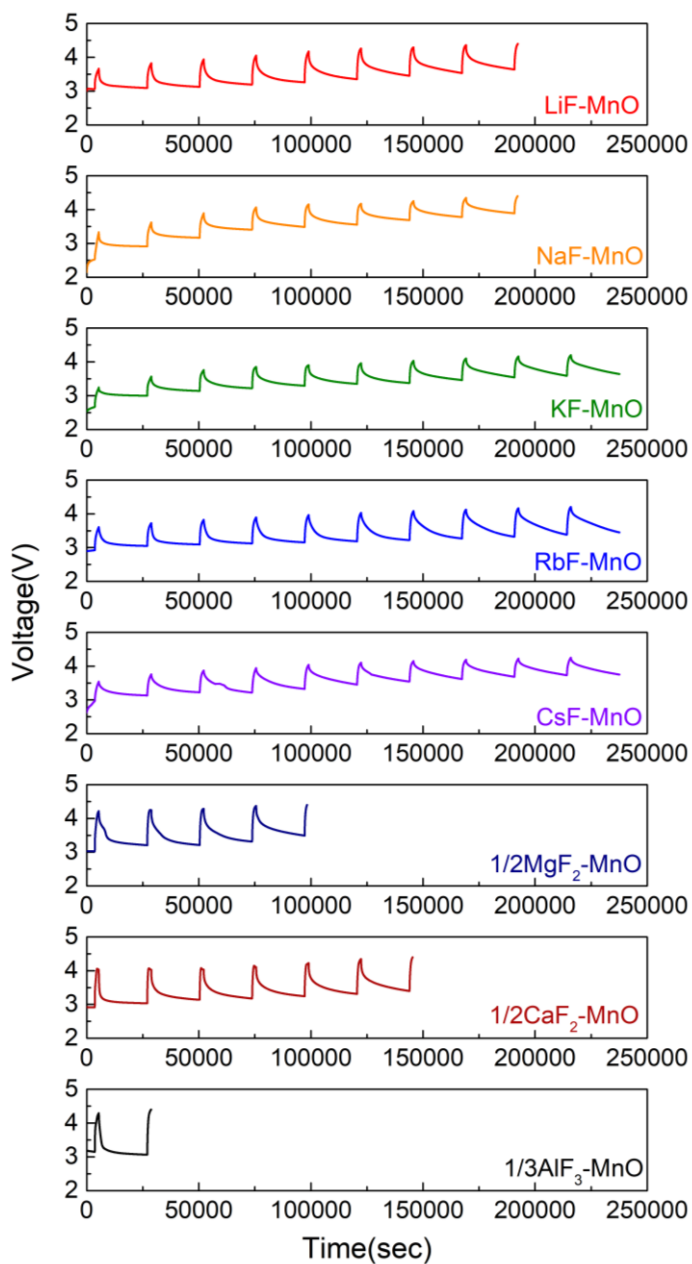
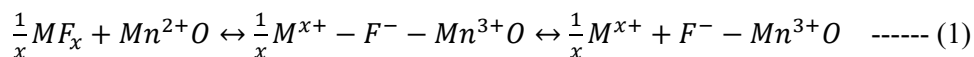


Figure 4.5. Galvanostatic intermittent titration technique (GITT) curves of $\text{MF}_x\text{-MnO}$ nanocomposites.

4.3.3. Effects of binding energy of F 1s on overpotential and activity

Equation 1 illustrates the activation process of the nanocomposite in the first charge, which can be divided into two processes involving the MF_x decomposition (liberation of fluorine ion) and oxidation of manganese ion. Actually, these two reaction occur simultaneously. Because the sole fluorine ion is highly unstable, fluorine ion will form a bonding with transition metal ion immediately with the oxidation through the intermediate state.



Therefore, oxidation of Mn in electrochemical reaction includes the additional energy to rip off fluorine ion from MF_x . The metal-fluorine bond strength in MF_x compounds can be estimated by the degree of electrostatic attraction force between cation and anion in ionic bond. In general, estimation of the bond strength in an ionic compound can be compared quantitatively by lattice energy. The lattice energy is defined as the energy to separate cation and anion infinitely as gaseous state from a solid crystal. Although the precise value of lattice energy is hard to obtain experimentally due to the infeasible formation of gaseous ion state, it can be inferred by the Born-Haber cycle or theoretical approach. Given the lattice energy can be derived from electric potential of ionic lattice and potential energy by Born and Lande as following equation 2, large attraction force between cation and anion in MF_x corresponding to large lattice energy can reduce the electrostatic shielding of nuclear charge from all other electron in the fluorine atom. Meanwhile, if the force become smaller (small lattice energy), electron shielding effect will increase,

followed by the decreased F 1s electron binding energy. Thus, the binding energy of F 1s core electron can be an indicator to compare the level of difficulty to rip off fluorine ion from MF_x.

$$E = -\frac{N_A M z^+ z^- q_e^2}{4\pi\epsilon_0 r_0} \left(1 - \frac{1}{n}\right) \text{ ----- (2)}$$

X-ray photoemission spectroscopy (XPS) of the F 1s region is measured for the eight MF_x-MnO nanocomposites to acquire the binding energy of core electron and the peak values of each spectrum are compared (Figure 4.6a). The lattice energy values of metal fluorides and electron binding energy of F 1s has strong correlation as shown in Table 4.1. Electron binding energy of F 1s in alkali-metal fluorides and lattice energy decreases as period of alkali-metal increases. Because bond strength of ionic bond decreases when ionic radius of cation increases. In the multivalent metal fluorides case (MgF₂, CaF₂, AlF₃), both parameters were higher than alkali metal case because of the high columbic force between fluorine and cations.

We analyzed the correlation between the binding energy of core electron in fluorine ion and overpotential of corresponding MF_x-MnO nanocomposites (Figure 4.6b). Interestingly, overpotential of initial charging has strong positive correlation with binding energy, which means that the attraction force between cation and fluorine affects the overpotential. In addition, the overpotential from group B has higher values (250 ~ 300 mV) than group A even at the similar binding energy. High overpotential of group B may be originated from slow kinetics induced by small surface area concentration due to the large particle size, which provides limited

active site for fluorine incorporation. Therefore, the binding energy accordingly has strong correlation with activity of nanocomposite (Figure 4.7). Linear regression analysis for group A ($\text{MF}_x\text{-MnO}$; $M=\text{Li, Na, K, Ca}$ and Mg) and group B ($\text{MF}_x\text{-MnO}$; $M=\text{Rb, Cs}$ and Al) indicates that each group has strong negative correlation according to Pearson correlation coefficient with $r = -0.97$.

The binding energy effect on activity of $\text{MF}_x\text{-MnO}$ nanocomposite was further examined by making a solid solution with LiF and CsF . LiF and CsF are known to make a solid solution in spite of the large lattice mismatch over 40 % through coordination change around the Li and Cs ions²⁰. The LiCsF_2 was synthesized through ball milling LiF and CsF powders. The XRD results of LiCsF_2 is shown in Figure 4.6c and all the peaks are matched with LiCsF_2 reference peak position (PDF# 22-1076). The F 1s binding energy of the LiCsF_2 is 684.3 eV and this value is almost half of the value of LiF (685.1 eV) and CsF (683.1 eV). The electrochemical profile of $0.5\text{LiCsF}_2\text{-MnO}$ and LiF-MnO is shown in Figure 4.6d. The voltage profile of the first charge is much lower in LiCsF_2 when compared with pure LiF . The lower binding energy in LiCsF_2 results in lower charging overpotential which leads to higher first charge capacity than pure LiF (Figure 4.6e). The capacity increased corresponding to $0.3\text{e}^-/\text{Mn}$ with the increase of 3.75 V redox activity.

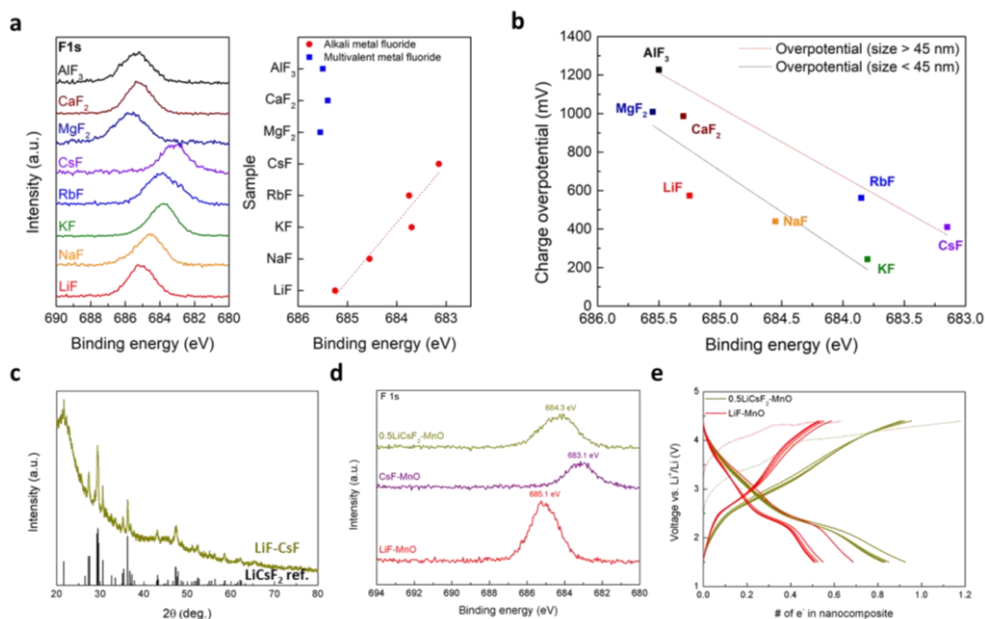


Figure 4.6. Effect of F 1s binding energy on the first charge overpotential and electrochemical activity of MF_x-MnO nanocomposites. (a) Binding energy of metal fluorides(MF_x)-MnO nanocomposites (MF_x-MnO, M=Li, Na, K, Rb, Cs, Mg, Ca, Al) from X-ray photoemission spectroscopy. (b) Dependency of the first charge overpotential on binding₂ energy of F 1s in MF_x-MnO nanocomposites. (c) XRD patterns of LiCsF₂ after mechanochemical synthesis. (d) Binding energy of LiF-MnO, CsF-MnO and 0.5LiCsF₂-MnO nanocomposite from X-ray photoemission spectroscopy. (e) Enhanced electrochemical activities of 0.5LiCsF₂-MnO nanocomposite. Each dotted line is 1st charge profile respectively.

Table 4.1. Correlation between the experimentally obtained F 1s binding energy and lattice energy of metal fluorides from Born-Haber cycle.

	LiF	NaF	KF	RbF	CsF	MgF₂	CaF₂	AlF₃
F 1s binding energy (eV)	685.25	684.55	683.8	683.85	683.15	685.55	685.3	685.5
Lattice energy (kJ/mol)	1045	924	822	784	737	2962	2600	5200

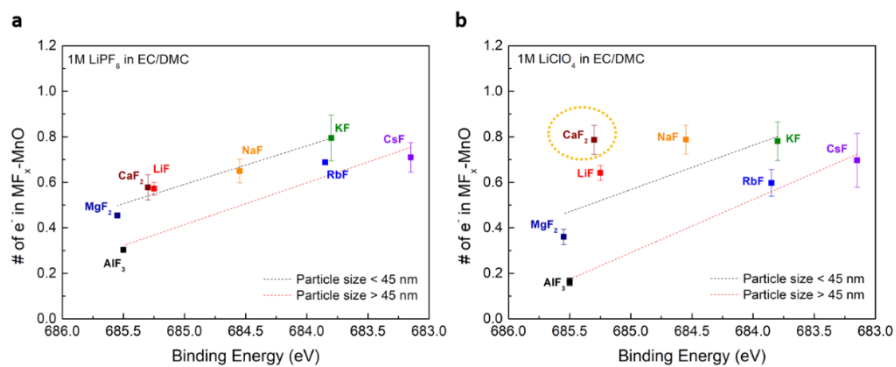
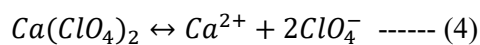
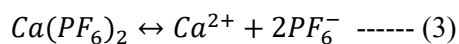


Figure 4.7. Relation between F 1s binding energy of MF_x (M=Li, Na, K, Rb, Cs, Mg, Ca and Al) and activity of MF_x-MnO nanocomposite electrode in (a) 1 M LiPF₆ in EC/DMC and (b) 1 M LiClO₄ in EC/DMC electrolyte. Each black and red line represents the linear relation between binding energy and activity in group A (black) and group B (red) compounds.

4.3.4. Effect of stability of cation in electrolyte on activity

Actually, the concept of lattice energy is hard to solitary applied to understand our system because final state of cation and anion is totally different with the gaseous state. Therefore, we considered the origin of overpotential and activity not only fluorine but also cation point of view. Stability of cation in electrolyte can affect to the kinetics of MF_x decomposition and following fluorine donation to MnO. First, we compare the electrochemical activity with the test performed by F free ClO_4 based electrolyte to eliminate the capacity that could be activated by PF_6^- salt decomposition⁸. The reversible capacities are comparable in both PF_6 and ClO_4 based electrolytes given each error ranges except Al and Ca (Figure 4.8a). For the Al case, larger capacity was obtained from LiPF_6 salt than from ClO_4 salt due to the electrolyte decomposition showing unstable voltage profile during the first charging with sudden increase and drop of voltage (Figure 4.9). Interestingly, however, the reversible capacity shows remarkably higher value in ClO_4 based electrolyte in the $1/2\text{CaF}_2\text{-MnO}$ system. It is surprising result since even the ClO_4 could not donate F to MnO and it shows comparable or lower capacity than PF_6 case in other seven compounds and in previous reports^{7, 8}. Simply, CaF_2 donates fluorine ion to MnO more easily in ClO_4 salt electrolyte than PF_6 salt based electrolyte. The DFT calculation was performed to find clue about this abnormal behavior in $\text{CaF}_2\text{-MnO}$ case (Figure 4.8b). The DFT calculation shows that the binding enthalpy between Ca^{2+} and 2ClO_4^- is lower than the value between Ca^{2+} and 2PF_6^- (about 0.1 eV) in the same dielectric constant condition with EC/DMC solvent. This means that the bond

strength between Ca^{2+} and 2ClO_4^- is much larger than between Ca^{2+} and 2PF_6^- . Therefore, the solvation of Ca^{2+} in ClO_4^- medium is energetically more favorable than PF_6^- medium indicating the reaction constant for reaction (4) is higher than reaction (3). Thus, in the $1/2\text{CaF}_2\text{-MnO}$ system, the driving force for the forward reaction (Ca^{2+} production) is greater in ClO_4^- based electrolytes, which promotes the decomposition of CaF_2 and consequently results in a higher reversible capacity in the ClO_4^- based electrolyte than in the PF_6^- based electrolyte. The same calculation was done in LiF and NaF for comparison. In contrast to CaF_2 case, the binding enthalpy of LiF and NaF was calculated in similar range in both ClO_4^- and PF_6^- cases. Proving this trend, we compared the initial first charge profile of Li , Na and Ca system. Surprisingly, the initial charge voltage of $1/2\text{CaF}_2\text{-MnO}$ in ClO_4^- salt system is 95 mV lower than that of $1/2\text{CaF}_2\text{-MnO}$ in PF_6^- salt (Figure 4.8c). Meanwhile, LiF-MnO and NaF-MnO showed almost same initial charge profiles in PF_6^- and ClO_4^- salt system (Figure 4.8d and 4.8e).



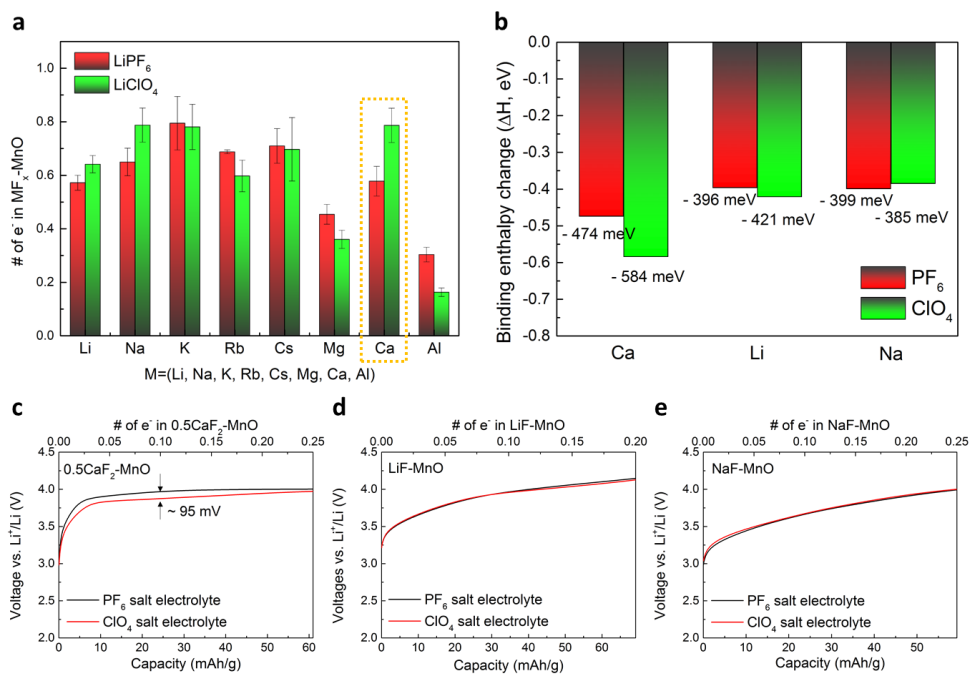


Figure 4.8. Effect of electrolyte salt on electrochemical activities of MF_x-MnO nanocomposites. (a) Reversible capacities of eight MF_x-MnO nanocomposites tested in 1 M LiPF₆ in EC/DMC (red) and 1 M LiClO₄ in EC/DMC (green). Each of data set was tested 5 times and the error bar is also shown in the graph. (b) The binding enthalpy of Ca²⁺, Li⁺ and Na⁺ with ClO₄⁻ (red) and PF₆⁻ (blue) calculated with DFT. (c) Initial profile of the first charge of 0.5CaF₂-MnO, (d) LiF-MnO, and (e) NaF-MnO nanocomposites as electrolyte salts.

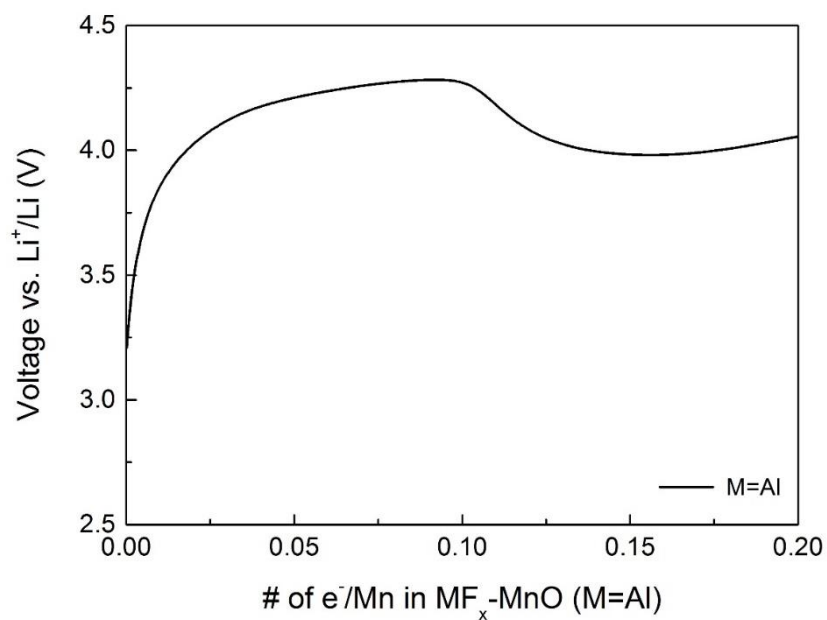


Figure 4.9. Initial charge profile of 1/3AlF₃-MnO nanocomposite electrode tested in 1 M LiPF₆ in EC/DMC.

4.3.5. Origins of the overpotential in the first charge activation

All the results above assist to understand the origin of the overpotential (η) in the first charge activation and electrochemical activity of $\text{MF}_x\text{-MnO}$ nanocomposites as summarized in Figure 4.10a. Considering the fact that the simultaneous process occurs including cation dissolution in electrolyte and fluorine ion incorporation into MnO, we found the factors that induce overpotential in the first charge reaction in terms of M and F each. First, the energy required to separate the F from the MF_x is dependent on the core electron binding energy of F because it has correlation with ionic bond strength corresponding to lattice energy. Second, we confirmed that the stability of cation in electrolyte can affect to overpotential, which is experimentally verified in special case of Ca. Lastly, the overpotential can be affected by the particle size of MnO, which is confirmed by the comparison between group A and B in the correlation of binding energy versus overpotential, because $\text{MF}_x\text{-MnO}$ follow the surface reaction mechanism. These three factors can be combined to form the overall overpotential as shown in Figure 4.10b. Since the sole F⁻ ion is remarkably unstable, the activation energy barrier (E_A) to form intermediate state of $\text{M}^{x+}\text{-F}_x\text{-MnO}$ can determine the overall overpotential. Among the parameters, F 1s binding energy corresponding to ionic bond strength serves as the main factor in determining the overpotential rather than electrolyte. Therefore, decreasing the ionic bond strength between cation and anion in lithium or alkali metal compounds can be the most effective to lower the overpotential of the first charge leading to obtain large activity in nano-mixture cathode. In addition, given

the fact that all types of MF_x can donate F^- ion, the effect of electrolyte also could be significant when the nano-mixture electrode design concept is applied to other rechargeable battery system beyond Li and Na such as K, Mg, and Ca.

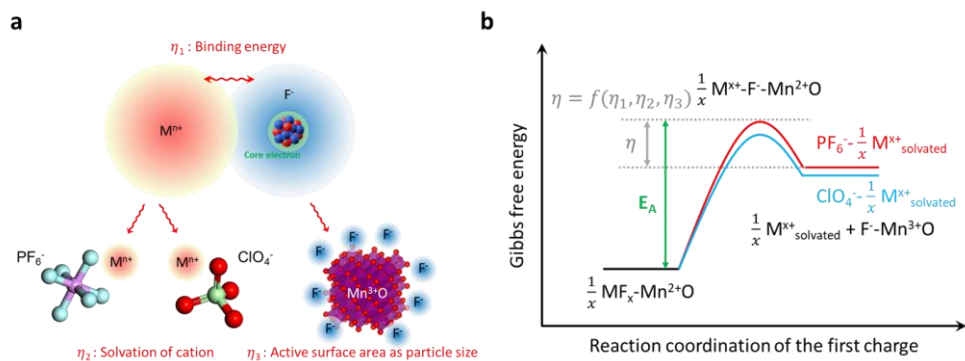


Figure 4.10. Origins of the first charge overpotential(η) affecting electrochemical activity in $\text{MF}_x\text{-MnO}$ nano-mixture cathode materials. (a) Activation barrier for liberating fluorine ion is affected by the attraction force of cation (M^{x+}) which can be estimated by F 1s binding energy. Stability of cation in electrolyte determines the kinetics of cation dissolution into electrolyte during the first charge. Particle size of MnO is another origin of overpotential because the surface conversion mechanism is affected by the active surface area for fluorine incorporation. (b) Schematic of the Gibbs free energy versus reaction coordination of the first charge that shows overall overpotential required for the uphill reaction. Red and blue line indicate two cases when system energy can be changed by stability of cation in electrolyte.

4.4. Concluding Remarks

In summary, we revealed the chemical origins of activity and first charge overpotential which is shown in nanocomposite electrode without exception. We systematically change the metal fluorides as a fluorine source for MnO as a model system ($\text{MF}_x\text{-MnO}$, $M=\text{Li, Na, K, Rb, Cs, Mg, Ca, Al}$). The first charge overpotential determines the reversible capacity and the overpotential is mainly affected by the binding energy of core electron in fluorine ion of MF_x corresponding to ionic bond strength. The stability of cation in electrolyte can assist to lower the overpotential minorly. Consequently, decreasing the binding energy is effective to achieve higher first capacity with low overpotential leading to higher reversible capacity. Finally, the feasibility of various metal fluorides as fluorine donor can open avenue for designing the cathode using nanocomposite concept to multivalent ion battery system.

4.5. References

1. Mizushima K, Jones P, Wiseman P, Goodenough JB. Li_xCoO_2 ($0 < x < 1$): A new cathode material for batteries of high energy density. *Materials Research Bulletin* **1980**, 15(6): 783-789.
2. Ohzuku T, Makimura Y. Layered lithium insertion material of $\text{LiNi}_{1/2}\text{Mn}_{1/2}\text{O}_2$: A possible alternative to LiCoO_2 for advanced lithium-ion batteries. *Chemistry Letters* **2001**, 30(8): 744-745.
3. Padhi AK, Nanjundaswamy KS, Goodenough JB. Phospho-olivines as positive-electrode materials for rechargeable lithium batteries. *Journal of the electrochemical society* **1997**, 144(4): 1188-1194.
4. Kim S-W, Nam K-W, Seo D-H, Hong J, Kim H, Gwon H, et al. Energy storage in composites of a redox couple host and a lithium ion host. *Nano Today* **2012**, 7(3): 168-173.
5. Dimov N, Kitajou A, Hori H, Kobayashi E, Okada S. Electrochemical splitting of LiF: a new approach to lithium-ion battery materials. *ECS Transactions* **2014**, 58(12): 87-99.
6. Okada S, Tsunoe D, Kitajou A, Hori H, Dimov N, Barpanda P. Possibility of Composite Cathodes with Sacrificial Salts. *Meeting Abstracts; 2016: The Electrochemical Society; 2016*. p. 33-33.
7. Jung S-K, Kim H, Cho MG, Cho S-P, Lee B, Kim H, et al. Lithium-free transition metal monoxides for positive electrodes in lithium-ion batteries. *Nature Energy* **2017**, 2: 16208.

8. Zhang L, Chen G, Berg EJ, Tarascon JM. Triggering the In Situ Electrochemical Formation of High Capacity Cathode Material from MnO. *Advanced Energy Materials* **2017**, 7(8).
9. Tomita Y, Nasu H, Izumi Y, Arai J, Otsuka S, Yamane Y, et al. Synthesis and charge-discharge properties of LiF-NiO composite as a cathode material for Li-ion batteries. *Journal of Power Sources* **2016**, 329: 406-411.
10. Tomita Y, Kimura N, Izumi Y, Arai J, Kohno Y, Kobayashi K. Synthesis and electrochemical properties of 4LiF-NiMn₂O₄ composite as a cathode material for Li-ion batteries. *Journal of Power Sources* **2017**, 354: 34-40.
11. Hwang I, Jung S-K, Jeong E-S, Kim H, Cho S-P, Ku K, et al. NaF-FeF₂ nanocomposite: New type of Na-ion battery cathode material. *Nano Research*: 1-10.
12. Zhang L, Batuk D, Chen G, Tarascon J-M. Electrochemically activated MnO as a cathode material for sodium-ion batteries. *Electrochemistry Communications* **2017**, 77: 81-84.
13. Kataoka R, Kitta M, Takeichi N, Kiyobayashi T. Electrochemical In Situ Synthesis: A New Synthesis Route for Redox Active Manganese Oxides for Rechargeable Sodium Ion Battery through Initial Charge Process. *Journal of The Electrochemical Society* **2017**, 164(2): A226-A230.
14. Jung S-K, Hwang I, Cho S-P, Oh K, Ku K, Choi I R, Kang K. New iron-based intercalation host for lithium-ion batteries. *Chemistry of Materials* **2018**, 30(6): 1956-1964

15. Frisch MJ, Trucks GW, Schlegel HB, Scuseria GE, Robb MA, Cheeseman JR, et al. Gaussian 09. Wallingford, CT, USA: Gaussian, Inc.; **2009**.
16. Becke AD. Phys. Re V. A **1988**, 38, 3098.(b) Becke. J Chem Phys **1993**, 98: 5648.
17. McLean A, Chandler G. Contracted Gaussian basis sets for molecular calculations. I. Second row atoms, $Z=11-18$. *The Journal of Chemical Physics* **1980**, 72(10): 5639-5648.
18. Tomasi J, Mennucci B, Cammi R. Quantum mechanical continuum solvation models. *Chemical reviews* **2005**, 105(8): 2999-3094.
19. Jain A, Ong SP, Hautier G, Chen W, Richards WD, Dacek S, et al. Commentary: The Materials Project: A materials genome approach to accelerating materials innovation. *Apl Materials* **2013**, 1(1): 011002.
20. Zhang X, Trimarchi G, d'Avezac M, Zunger A. Long-range order instead of phase separation in large lattice-mismatch isovalent AX– BX systems. *Physical Review B* **2009**, 80(24): 241202.

Chapter 5. Conclusion

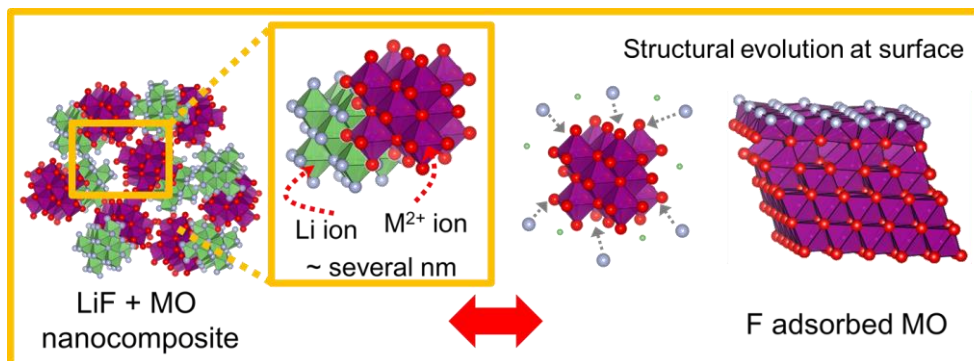
Conventional cathode materials for lithium rechargeable batteries usually contain intrinsic lithium and transition metal ion is same crystal structure with diffusion path for lithium. In this research, a new design concept of cathode materials is suggested to develop high energy density batteries by extending the boundaries of cathode materials that used to occupy minor portion in numerous compounds in nature. Cathode materials are designed as a nano-mixture of lithium compounds and transition metal compounds by mechanochemical mixing. In chapter 2, I verified the feasibility and general applicability of cathode design strategy by using the metal monoxide and lithium fluoride as transition metal compounds and lithium compounds each. Even though the metal monoxides (MO, M=Mn, Fe, Co) have neither intrinsic lithium nor diffusion path, nanocomposite of LiF-MO showed high capacity exhibiting over 200 mAh/g with ~ 3 V average potential. Representative cathode LiF-MnO showed surface-controlled reaction kinetic behavior leading to high power capability. High power characteristic is induced by surface concentrated oxidation and reduction with structural evolution of MnO. The surface reaction occurs by reversible incorporation of fluorine ion formed by LiF during the charge process as depicted in Figure 5.1. Surface area of transition metal compounds directly affects to the electrochemical activity of the nanocomposite cathode. Especially, the capacity is tunable by control the particle size of transition metal compounds, which is in contrast to the conventional cathode. This reaction mechanism is called ‘surface conversion’.

In addition to the surface conversion reaction, another reaction mechanism called ‘host formation’ is shown in some combination of lithium and transition metal compounds. In chapter 3, host formation reaction is observed from LiF and FeO nanocomposite system. Host formation reaction indicates the irreversible transformation to fluorine incorporated new phase of transition metal compounds. In contrast to surface conversion reaction that reversible fluorine incorporation mainly occurs on the surface of particle, incorporated fluorine ion induce phase transition of bulk to a new phase that can accommodate the lithium in the structure. In the case of LiF-FeO nanocomposite, new phase of cubic-FeOF phase is observed after host formation reaction. Cubic-FeOF phase which belongs to cubic crystal system has different structure to the thermodynamically stable rutile-FeOF phase of tetragonal crystal system. Cubic-FeOF phase of metastable state is gradually induced during electrochemical cycling due to its similar structure of FeO rock salt phase. In general, rutile-FeOF accompanies intercalation and conversion reaction sequentially during the discharge meanwhile cubic-FeOF shows intercalation reaction in the whole range of discharge reaction, which is advantageous to voltage hysteresis (Figure 5.2).

In chapter 4, the chemical origins of common issue on the nanocomposite cathode exhibiting the large overpotential in the first charging reaction regardless of reaction mechanism is revealed. Both surface conversion and host formation reaction accompany common reaction corresponding to the decomposition reaction of lithium compounds during the first charge. Various metal fluorides (LiF, NaF, KF, RbF, CsF, MgF₂, CaF₂, AlF₃) and MnO are used as a model system to investigate the origin of the large overpotential. In the lithium hybrid cell system, the large

overpotential of each nanocomposite is kinetically induced depending on metal fluoride species. The overpotential is affected by the lattice energy, which is thermodynamic energy value that is required to decompose ionic compound as ion state respectively. Especially, binding energy of core electron in fluorine ion has strong linear correlation with lattice energy, which imply that binding energy can be a physical parameter to control the overpotential. As a result, solid solution of LiF and CsF shows lower overpotential than sole LiF case in the first charge, which leads to the larger discharge capacity in LiCsF₂ system.

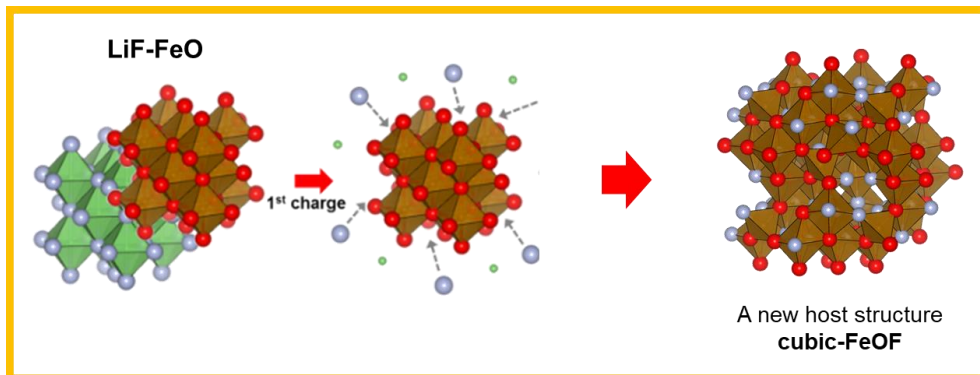
In this thesis, I suggested new design strategy of nanocomposite cathode materials and revealed the reaction mechanism with the origins of the electrochemical activity. Although the research on nanocomposite is currently infant stage, I believe that this thesis contributed to develop new chemistry and scientific understanding on nanocomposite electrochemistry. I hope that numerous candidate of cathode that can be practically applicable is excavated through the nanocomposite cathode design strategy.



Reaction mechanism: **Surface conversion reaction**
(Redox reaction + Structural evolution)



Figure 5.1. Surface conversion reaction mechanism in LiF-MnO nanocomposite electrode.



Reaction mechanism: **Host formation reaction**

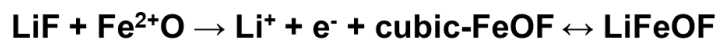


Figure 5.2. Host formation reaction mechanism in LiF-FeO nanocomposite electrode.

국 문 초 록

전자기기의 개발 및 그 활용이 다양화 되고, 다각화 됨에 따라 리튬 이차 전지 에너지 저장 시스템에 대한 수요가 폭발적으로 증가하고 있다. 리튬 이차 전지의 공급뿐만 아니라 높은 에너지 밀도, 우수한 파워 및 수명과 같은 특성들도 함께 요구되고 있다. 이에 따라 리튬 이차 전지 성능을 주로 결정하는 양극 소재에 대한 연구와 탐색이 진행되었고, 특성 개선 등의 다양한 시도와 더불어 많은 후보 물질들이 발굴되었다. 그러나 에너지 밀도를 개선하는데 있어 현실적으로 적용 가능한 방법은 기존 양극 소재로 잘 알려진 층상형 화합물의 전이금속 조성을 바꾸는 것 이외에는 (예: LiCoO_2 , $\text{LiNi}_{1-x-y}\text{Co}_x\text{Mn}_y\text{O}_2$) 다른 방법이 없었다. 게다가 실용적으로 적용 가능한 수준의 파워 및 수명 특성은 오직 스피넬이나 올리빈 물질과 같은 종류의 소수의 물질 개발 만을 통해 가능 하였다. 이러한 맥락에서, 현재 배터리 기술은 소형 전자기기를 뛰어넘어 전기자동차나 에너지 저장 시스템과 같은 중대형 전자장비등에 확장 적용되기에는 여러 큰 문제에 직면해 있다.

특히 삽입 및 탈리 반응을 하는 지금까지 개발된 대부분의 양극소재들은 무게당 용량을 개선하는데 본질적인 한계점을 갖고 있다. 일반적 양극소재들은 대개 열린 형태의 동일 결정 구조 안에 산화 환원 반응을 할 수 있는 전이금속 및 리튬이 함께 포함되어 있다. 가능한 많은 양의 리튬을 저장 할 수 있다면 용량도 크게 증가 될 수 있지만 리튬을 저장 할 수 있는 침입형 자리의 개수는 전이금속의 동일한 개수로 보통 제한된다. 만약 일부 전이 금속을 리튬으로 치환하여 강제로 리튬을 저장 할 수 있는 침입형 자리의 수를 늘리더라도, 그로 인한 전이금속 이온의 감소는 모든 리튬을 대응할 만큼의 충분한 전자를 제공 할 수 없게 된다. 따라서 음이온에 의한 추가 용량을 발현하는

과잉 리튬 물질을 제외하고, 결정 구조내 삽입 및 탈리 반응을 하는 양극소재군은 태생적으로 용량을 증가시키는데 있어 결정학적인 한계점을 갖고 있다.

따라서 삽입 및 탈리 반응을 하는 기존 양극 소재의 문제점을 극복하기 위해서는 새로운 양극 소재 디자인 방법이 필요하다. 본 논문에서는 그 대안으로 리튬 및 전이금속 화합물이 혼합된 형태의 새로운 나노 복합체 양극 소재군을 제시한다. 이 양극 소재는 첫 충전시 리튬 화합물의 분해로부터 발생된 음이온이 전이금속 화합물로 혼입되는 과정을 통해 전이금속의 산화를 수반하며 전기화학적 활성을 갖게 된다. 반응 메커니즘은 음이온의 혼입 거동에 따라 표면 전환 반응과 호스트 형성 반응으로 구분되는데, 특히 표면 전환 반응 메커니즘의 경우 전이금속의 산화 환원이 주로 물질 표면에서 일어난다. 덕분에 입자 사이즈 조절을 통한 표면적 조절을 통해 발현되는 용량을 변화시킬 수 있다. 이러한 반응 메커니즘은 기존 결정학적 구조에 구애를 받지 않는 에너지 저장 반응이며 따라서 기존 양극 소재의 한계를 극복 할 수 있는 방안이 될 수 있다. 나노 복합체 양극 소재 디자인 방법은 리튬 이차전지뿐만 아니라 나트륨 및 칼륨 배터리 시스템에 이르기까지 확장 적용이 가능하다. 이러한 양극 디자인 전략은 리튬 화합물과 전이금속 화합물의 다양한 조합을 통해 양극 소재로 활용 가능한 물질 범위의 경계를 확장 할 수 있는 기회를 제공하며, 높은 에너지 밀도를 갖는 양극 소재 개발에 기여 할 수 있다.

주요어: 나노 복합체, 배터리, 표면 전환 반응, 호스트 생성 반응, 양극, 혼합물, 리튬 이차 전지.

학 번: 2014-30216